DEVELOPMENT OF A PROCESSING-STRUCTURE-FATIGUE PROPERTY MODEL FOR SINGLE CRYSTAL SUPERALLOYS

by

Clinique L. Brundidge

A dissertation submitted in partial fulfillment
of the requirements for the degree of
Doctor of Philosophy
(Materials Science and Engineering)
in The University of Michigan
2011

Doctoral Committee:

Professor J. Wayne Jones, Co-Chair
Professor Tresa M. Pollock, Co-Chair
Professor John E. Allison
Assistant Professor Samantha H. Daly

To my family, for all their support over the years

Acknowledgements

First and foremost, I would like to thank my advisor, Tresa Pollock, for accepting me into her research group and providing me with guidance and support throughout this work. I would also like to especially thank J. Wayne Jones for taking on the role as my co-advisor for the past couple of years and welcoming me into the Jones-Daly-Allison group. I also wish to acknowledge my committee members, Samantha Daly and John Allison, for their helpful comments and suggestions. I am truly blessed to have the opportunity to work with such knowledgeable and renowned individuals.

Additional recognition goes to my collaborators at General Electric, specifically, Norb Maurer (GE-Aviation), Doug Konitzer (GE-Aviation), Laura Carroll (currently at Idaho National Laboratory) and Drew Elliott (GE-Energy). Thank you for all of the feedback, insightful information relevant to the industry and funding for the research.

I am extremely grateful to Chris Torbet, our Senior Research Engineer at the University of Michigan—and now UC Santa Barbara, for providing me with instruction and assistance in conducting experiments safely and efficiently. My fellow group members within the Pollock, Jones, Daly and Allison groups from 2006-2011 deserve an addition thanks. Every member has provided me with useful discussions and support. I would also like to acknowledge my office mates for the intellectual discussions, support and lab assistance: McLean Echlin, Jason Van Sluytman and Kate Gallup. A special thanks goes to Brian Wang, a former graduate student in the group, who helped me integrate into the Pollock group when I was an undergraduate student.

I wish to acknowledge all of the undergraduate students that have worked with me on various aspects of this research including: Peter Seo (Univ of Michigan), Elizabeth Rowles (Oxford University), Akosua Miller (Univ of Michigan), Denar Van Drasek (Univ of Michigan), Guy Hamburger (Univ of Michigan), and Dwayne Sharper (Univ of Michigan).

Mentorship from individuals within the department has definitely been a great asset to me during my matriculation at the University of Michigan. Obi Ezekoye, Jonathan Madison and Jason Van Sluytman all have been a great support network.

I am grateful for the support that my mother, father and two brothers have given me while at the University. You love, guidance and interest in my work has definitely helped me to stay grounded for the past 5 years.

TABLE OF CONTENTS

List of Figures

List of Tables

Abstract

Single crystal nickel-base superalloys have emerged as the materials of choice for high-temperature applications when significant resistance to fatigue loading is required. Although the fatigue life improvements due to a direct material substitution may be possible, additional gains are possible through advanced casting techniques in comparison to typical production processes. However, before integration in the manufacturing sector, optimization of a higher thermal gradient process for producing refined, homogeneous, single crystal components with improved fatigue properties is imperative.

In this dissertation, a higher cooling efficiency process, specifically, liquid-metal cooling (LMC) using Sn as the cooling medium, has been evaluated for potential fatigue property benefits of single crystal superalloy airfoil-sized components. A series of casting experiments were conducted using conventional radiation cooled Bridgman casting and the LMC process to compare the refinement in dendritic spacings and defect size distribution for 1.6 cm diameter rods. Casting conditions were selected to observe the trend in refinement with increasing cooling rate, as well as to identify the limit to structure refinement with the LMC process. Single-crystal René N5 and a modified version of the René N5 alloy were grown using both processes in order to evaluate the influence of segregation of alloying elements and defect occurrence with the addition of the refractory element, Ta. Newly developed statistical modeling techniques were employed to characterize the homogeneity in microstructure. Fatigue experiments were performed at 538^{o}C (R = 0, f = 0.5 Hz), along with unique *in-situ* crack growth studies (R = 0.1, f = 20 kHz) to examine the influence of refinement on the fatigue life and crack propagation behavior.

The LMC process is capable of refining the dendritic spacings and maximum pore size by 60 and 65 pct, respectively. The primary initiation sites for fracture in the single crystals during low cycle fatigue (LCF) were casting pores that were located internally and near to the surface. These pores were strongly influenced the crack initiation life. An empirical-based processing-structure-fatigue property model that relates the critical aspects of processing conditions to fatigue life has been developed.

Chapter 1

INTRODUCTION

1.1 Motivation for Superalloy Development

Directionally solidified nickel-base superalloys used in the hot-section of turbine airfoil systems are one of the critical components of jet-engines that play an important role in addressing the efficiency challenges.[1] This exceptional class of metallic materials is widely used in aircraft and power generation turbines, due to their excellent resistance to high-temperature mechanical degradation in corrosive or oxidizing environments.[2]

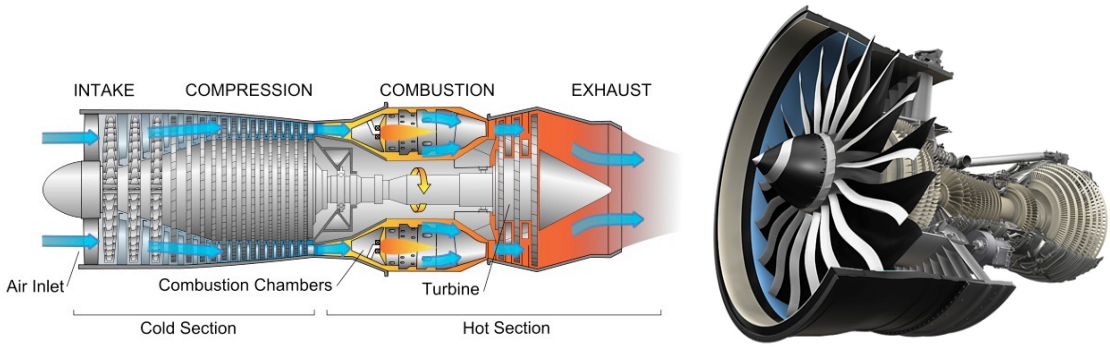

(a) (b)

Figure 1.1 (a) Schematic of a typical jet engine illustrating the hot section turbine blades.[3] (b) Cross-section of a GEnx aircraft engine, courtesy of GEAE.com.

Comprised of a combination of group VIIIA elements, nickel-base alloys are precisely developed for elevated temperature service where severe mechanical stressing is induced. These alloys are typically used at higher fractions of their melting temperature compared to other conventional alloys and contribute to 40-50% of the total weight of an aircraft engine.[2,3] Superalloys are located in the critical sections of the engine where accelerating hot-gas exits the combustor, Figure 1.1a.

Hot-section materials development has produced significant contributions to the performance of aircraft engines and land-based turbines with innovation in directional solidification technology and advancement in alloy chemistry. Consequently, the temperature capabilities of turbine blades have increased by more than 125^{o}C in the past 30 years.[4] The motivation for continued superalloy development stems from the need for further increases in the efficiency of aircraft engines, the desire for ultra-efficient power generation systems to meet the needs of rapidly growing economies, and light-weight, highly durable military jet engines. Within the aviation industry, customer requirements have provided a driving force for materials development and implementation on an accelerated timeline.[5] Stringent demands, including lifetime improvements, have continuously established challenges for future desired capabilities and consequently motivates superalloy development. To better understand the challenges involved in designing for improved single crystal superalloy mechanical properties, this chapter will address the fundamental issues of alloy development, optimization of solidification processing conditions, and the life limiting factors during cyclic loading. Approaches taken for fatigue property prediction will be reviewed next and, finally, the objectives and methodology of this dissertation research are described.

1.2 Nickel-Based Superalloy Evolution

Since the 1960s the need for improved elevated temperature mechanical properties of turbine blades has motivated investigations on the effects of alloying additions on mechanical, physical and environmental properties. Figure 1.2 displays various elements that typically comprise a superalloy composition. It is known that strengthening is typically achieved by increasing the Al concentration in superalloys, decreasing the Cr content and increasing the levels of Group VIB and VIIB refractory transition metals.[6, 7] However, with increases in refractory elements, the stability of precipitated phases and the formation of solidification defects during casting become concerns.

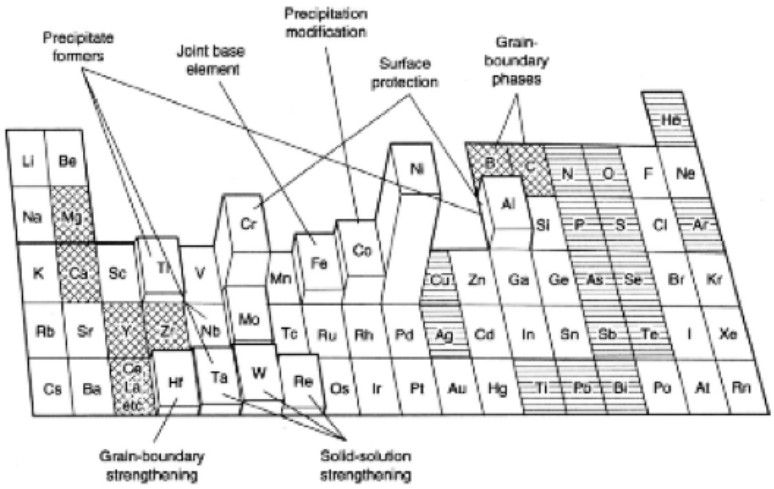

Figure 1.2 Important elements and their respective role(s) in Ni-base superalloys. Beneficial minor elements are marked with hatching, while detrimental elements are marked with horizontal lines.[7]

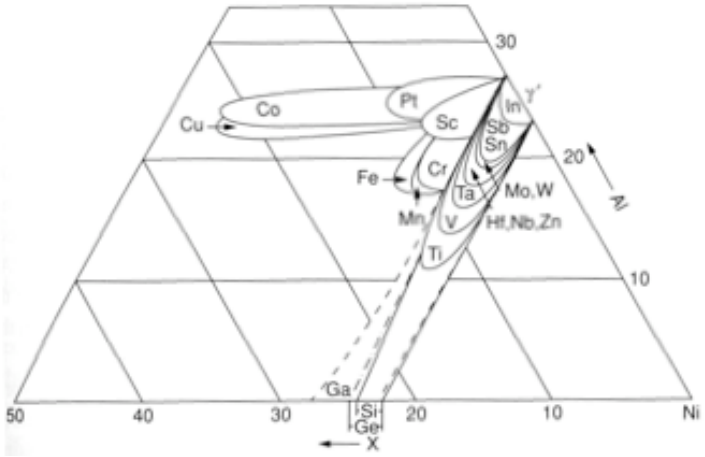

Figure 1.3 Superimposed Ni-Al-X ternary phase diagram for possible nickel-base superalloys.[3]

Superimposed Ni-Al-X ternary phase diagrams are shown in Figure 1.3. Most alloying elements in nickel-based superalloys reside in the *d*-block of the periodic table. The major phases in superalloys include the γ′ phase, which exists as precipitates that are embedded in a γ matrix. Elements that usually constitute the FCC austenitic matrix, γ, include: nickel, iron, cobalt, chromium, molybdenum, ruthenium, rhenium and tungsten due to their similar atomic size as nickel.[3] The γ′ phase, Figure 1.4, often coherent with the γ-matrix, is generally enriched with aluminum, titanium, tantalum, vanadium and niobium to promote the formation of the Ni_3X (X = Al, Ta, Ti, V, or Nb) ordered $L1_2$ phase. The microstructure of a single-crystal superalloy typically consists of at least 55%

by volume of cuboidal γ' precipitates in a γ matrix. The precipitate size has been shown to depend on the rate at which the alloy is cooled through the solvus temperature and the aging cycles employed.[2,8]

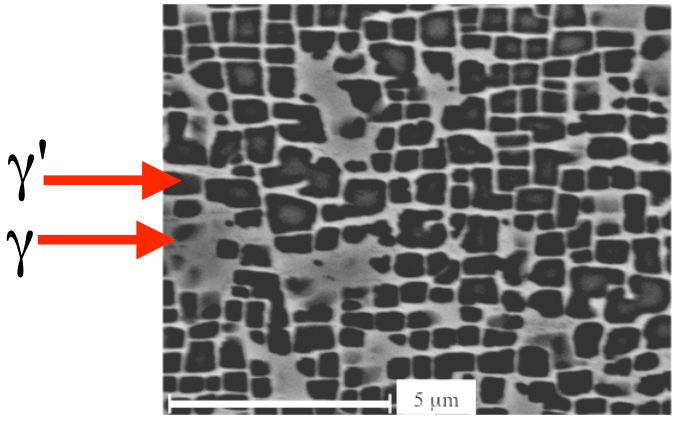

Figure 1.4 Scanning electron microscopy image of γ/γ′ microstructure of a second- generation nickel-base superalloy.

Figure 1.5 shows an example of script carbides within the interdendritic area. Carbon is added to the single crystal superalloy composition for purification of the alloy melt,[9] strengthening of any grain boundaries,[10] and reducing the extent of segregation for refractory elements.[11] Carbide and boride phase formation is promoted by the additions of chromium, molybdenum, tungsten, niobium, tantalum, hafnium and titanium in addition to C and B. Some of these reactive elements may combine with up to 0.2 wt% carbon to form MC-type carbides, which may be beneficial for solidification, but may be detrimental for mechanical performance,[11] Typical MC carbides include: TaC, TiC, and HfC.

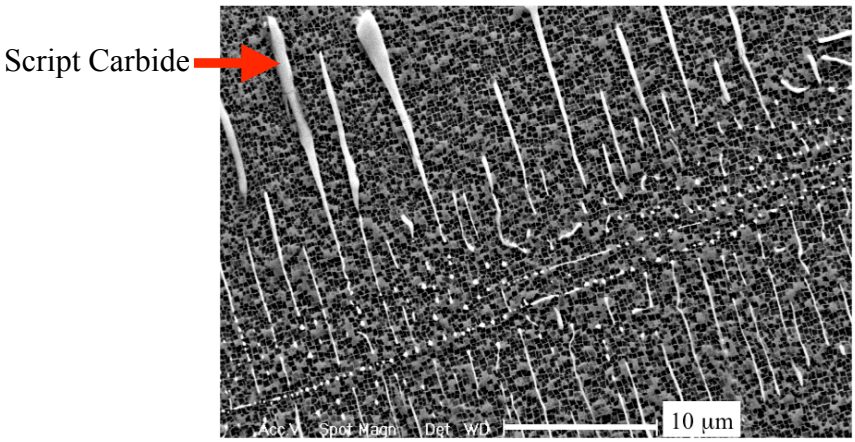

Figure 1.5 Script carbides formed during the solidification of a second-generation single-crystal nickel-base superalloy.

Thermal processing of the alloy can promote the conversion/decomposition of the MC carbides to other phases such as $M_{23}C_6$, M_7C_3 or M_6C. Additionally, complex intermetallic phases that are undesirable, but commonly found within nickel-base superalloys, include topologically closed packed (TCP) μ, σ and Laves phases.

The microstructure of nickel-base superalloys is based on the precipitation transformation:[12]

$$\gamma^S \rightarrow \gamma + \gamma' \qquad [1.1]$$

where γ^S is a supersaturated solid solution. The γ/γ′ microstructure allows for preferred cube-cube orientation relationship due to similar lattice parameters. One factor that strongly influences the mechanical properties of these alloys is the coherency of the γ/γ′ interface, associated with the lattice misfit that is defined as:

$$\delta = \frac{\alpha_{\gamma'} - \alpha_{\gamma}}{\frac{1}{2}(\alpha_{\gamma'} + \alpha_{\gamma})} \qquad [1.2]$$

where $a_{\gamma'}$ and a_{γ} are the lattice parameter of the precipitate and the matrix respectively. The lattice parameter of the γ phase is typically larger than the γ′ phase generally resulting in a very small and negative lattice misfit of approximately -0.2 to-0.3% in commercial single crystal superalloys.[13] Precipitation strengthening occurs due to the

high resistance of precipitates to shearing by dislocations. Strengthening of the γ′ precipitates by elements such as Ti and Ta is effective for increasing the resistance to shearing of precipitates.[3] Tantalum is also beneficial to the solidification process since it significantly reduces the tendency toward convective instabilities and freckling.[14]

The development of the optimal compositions and properties in superalloys alloyed by more than 15 elements is a highly laborious task, which requires an abundant amount of time and cost. Each new generation of single crystal alloys has allowed for increases in temperature capability by 20-25°C.[3] Examples of alloys which have been developed over time are listed in Table 1.1. Therefore, it is critical to obtain an understanding of how each element affects the solidification process, since solubility limits may change with alloy chemical modification.[15]

Table 1.1 Various generations of conventionally cast, directionally solidified and single-crystal nickel-base superalloys.[3,16]

Alloy	Cr	Co	Mo	W	Ta	Re	Nb	Al	Ti	Hf	C	B	Y	Zr	Other	Ni
Conventionally Cast Alloys																
Mar-M246	8.3	10	0.7	10	3			5.5	1	1.5	0.14	0.02		0.05		bal
In-100	10	15	3					5.5	4.7		0.18	0.01		0.06	1.0 V	bal
Rene 80	14	9.5	4	4				3	5		0.17	0.02		0.03		bal
Directionally Solidified Alloys																
IN792	12.6	9	1.9	4.3	4.3			3.4	4	1	0.09	0.02		0.06		bal
GTD111	14	9.5	1.5	3.8	2.8			3	4.9		0.1	0.01				bal
GTD444	9.8	7.5	1.5	6	4.8		0.5	4.2	3.5	0.15	0.08	0.01				bal
1st Generation Single Crystal Alloys																
PWA 1480	10	5		4	12			5	1.5							bal
Rene N4	9.8	7.5	1.5	6	4.8		0.5	4.2	3.5	0.15	0.05	0				bal
CMSX-3	8	5	0.6	8	6			5.6	1	0.1						bal
2nd Generation Single Crystal Alloys																
PWA 1484	5	10	2	6	9	3		5.6		0.1						
Rene N5	7	7.5	1.5	5	6.5	3		6.2		0.15	0.05	0	0.01			bal
CMSX-4	6.5	9	0.6	6	6.5	3		5.6	1	0.1						bal
3rd Generation Single Crystal Alloys																
Rene N6	4.2	12.5	1.4	6	7.2	5.4		5.8		0.15	0.05	0	0.01			bal
CMSX-10	2	3	0.4	5	8	6	0.1	5.7	0.2	0.03						bal

1.3 Optimization of Solidification Processing Conditions

To increase the efficiency of the engine, directionally solidified single-crystal superalloys have been employed in gas turbine blades since the mid 1970s and early 1980s due to their superior resistance to creep and thermo-mechanical fatigue compared to any other metallurgical material.[1] High strength conventionally cast alloys such as IN100 and René ’80 were used as airfoil materials until the introduction of directionally solidified MAR-M200 + Hf airfoils.[9] During the past few decades, casting methods

have progressed from conventional casting, producing an equiaxed (EQ) microstructure, to columnar grain (CG) and finally single crystals (SX) (Figure 1.6),[17] which has been driven by the need for mechanical improvements at higher temperatures. Directional solidification of an airfoil component allows for the growth of single crystals with controlled crystallographic orientation. Strain-controlled fatigue is maximized with [001] orientation due to the low modulus of elasticity in the longitudinal direction. Single crystal superalloys are advantageous over conventionally cast and directionally solidified alloys due to the removal of grain boundaries, eliminating creep damage initiation sites in the microstructure. Further performance improvements are possible with changes in the solidification processing to produce finer microstructures that consequently improve the mechanical properties.

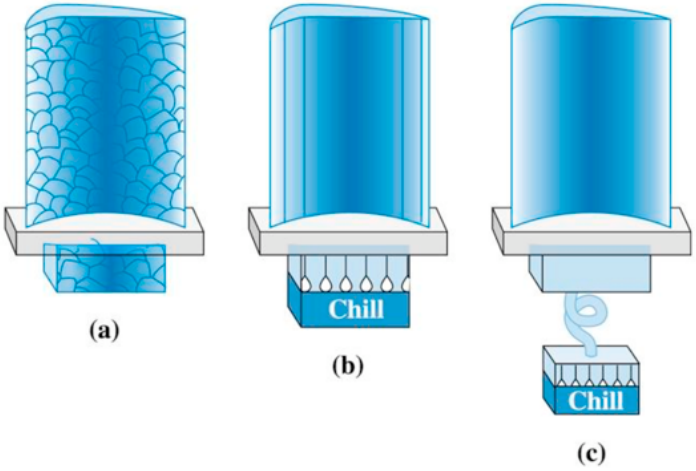

Figure 1.6 Schematic of various grain structures in cast turbine blades: (a) conventional equiaxed grains, (b) directionally solidified columnar grains, and (c) single crystal.[17] The "chill" represents the chill plate below the mold.

Within the past few decades, radiation-cooled Bridgman-type solidification processes have been used to cast single-crystal components. However, a new liquid-metal cooling (LMC) casting process is currently being evaluated as an alternative manufacturing process to refine the cast microstructure and achieve a cost-effective yield for single-crystal airfoils.[3] This section will highlight the major differences between the processes and give insight to the progress being made toward optimizing higher gradient casting processes.

1.3.1 Conventional Radiation Cooling

Fabrication of equiaxed turbine blades using the 'power-down' method has evolved into directional solidification of single-crystals via the Bridgman casting process (Figure 1.7).[18] This radiation-cooled method, detailed in the work of Gell *et al.*,[9] involves pouring a molten alloy into a pre-heated ceramic mold that sits upon a water-cooled chill plate. A schematic of this process is shown in Figure 1.7.[19]

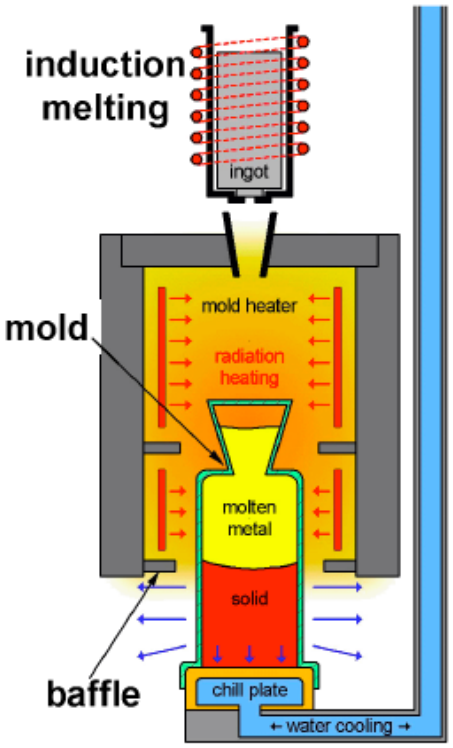

Figure 1.7 Schematic of Bridgman casting process. Diagram courtesy of Andrew Elliott.[19]

Withdrawing the investment mold from the mold-heater to the cold vacuum chamber leads to heat extraction primarily by radiation. Dendritic growth is favored in the direction of the thermal gradient, which is steadily maintained by lowering the mold from the mold heater through a stationary radiation baffle and into a cool-zone, with the solidification front proceeding unidirectionally. A withdrawal speed of a few millimeters per hour is maintained to control the location of the solid/liquid interface and to have controlled motion along the length of casting. A slow withdrawal rate must be maintained to preserve a stable solid/liquid interface and to avoid undercooling and the

formation of equiaxed grains. Assuming uniaxial heat flow, the withdrawal speed chosen is heavily dependent on the heat balance for moving a nearly planar solid/liquid interface and is given by:[20]

$$K_S G_S - K_L G_L = \rho_S L_f V_I \qquad [1.3]$$

where K is the thermal conductivity, G is the thermal gradient, ρ is the density, L_f is the latent heat of fusion, V_I is the solid/liquid interface velocity, and the subscripts S and L refer to solid and liquid phases, respectively. With stable solid/liquid interface conditions, the withdrawal rate can be taken as the solid/liquid interface velocity, V_I, thefore, these terms may be used interchangeably. A maximum solidification velocity is obtained when G_L nears zero as

$$V_{I,\max} = \frac{K_S G_S}{\rho_S L_f} \qquad [1.4]$$

Typical thermal gradients and withdrawal rates range from 10 to 100°C/cm and 5 to 40 cm/hr, respectively,[9] and the actual values used are highly dependent on the size and geometry of the castings in order to produce a dendritic structure. At optimized conditions, the solidification zone is maintained at the baffle line to avoid extraneous nucleation and to increase the heat-extraction capability of the system. A grain selector or seeded starter is typically used in order to produce a single, well-oriented grain with the <001> crystallographic orientation.

Equiaxed castings were first produced by the 'power-down' method, which involved reducing the power of the furnace gradually with time after the molten metal was poured into an investment mold.[3] The benefits of the Bridgman process compared to the power-down method include increasing the solidification rate and temperature gradient in the solid.[9] Directionally solidifying superalloys using radiation cooling has helped pave the way for casting single-crystal turbine airfoils with complex geometries.[9] However, thermosolutal convective instabilities that initiate at low cooling rates with the Bridgman process can produce fragmentation of dendrite arms, which subsequently develop small chains of equiaxed grains aligned parallel to the withdrawal direction.[21] If these microstructural features develop in a cast single-crystal, they are detrimental to the

mechanical properties. Misoriented grains possessing high angle grain boundaries can also develop at low cooling rates.[2] These defects can serve as crack-initiation sites during fatigue and must be avoided. Both defect types can contribute to low casting yields, but can be improved by increasing the thermal gradient in the casting process.[2] Recent studies have shown that increasing the temperature gradient, *G*, and solidification rate, *V*, can further improve the mechanical properties, refine the dendritic structure and reduce defects within the microstructure.[22] Therefore, the capability of the LMC process to increase *G* and *V* for a specified geometry is highly desirable and was investigated in this research.

1.3.2 Optimization of the Liquid Metal Cooling Process

Investigation of the solidification parameters used in Bridgman casting has demonstrated the need for additional heat transfer modes other than radiation.[23] Even though the Bridgman solidification technique has been the conventional means for growing single-crystals for the production of aero-engine scale parts, interest in the casting of large industrial gas turbine (IGT) components has exposed several critical issues. Maintaining a sharp and well-oriented thermal gradient at the solid/liquid interface during solidification is difficult with physically large crystals using the Bridgman method and has resulted in slow withdrawal rates and low casting yields. Other challenges in casting of complex IGT components include shell mold warping and cracking, mold-metal reaction, and low casting yields.[2,23] The impeding factor for the production of the IGTs with the Bridgman method originates from the low rate of heat extraction. The LMC process provides a means to improve the heat transfer conditions by solidifying the alloy into a metal-coolant possessing a low melting temperature, Figure 1.8. The liquid metal bath serves as a heat sink for the casting and extracts heat via conduction and convection. Liquid tin is an outstanding candidate as a coolant due to its low melting temperature, low vapor pressure, high boiling point, moderate cost, and minor impact on alloy properties.[24] Improvement of the thermal isolation between the hot and cool zones in the furnace by using a unique combination of a tin coolant and a dynamic floating baffle and has been shown to sharpen and maintain a steady thermal gradient at the solid/liquid interface at faster withdrawal rates throughout the entire casting process. [22,25]

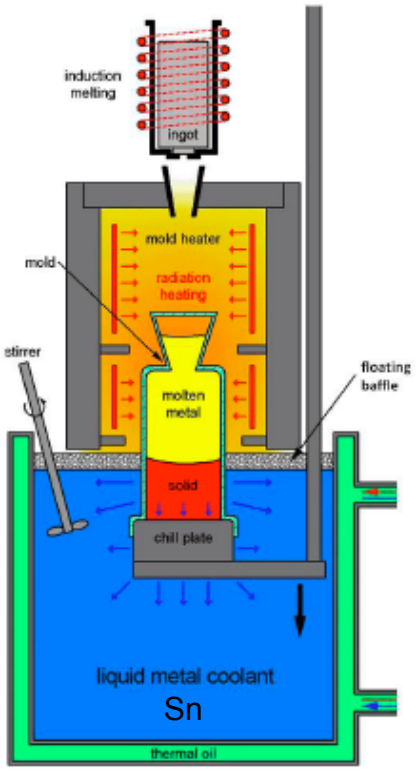

Figure 1.8 A schematic of the liquid-metal cooling process. Diagram courtesy of Andrew Elliott.[19]

A schematic of the major components within the LMC process is shown in Figure 1.8. Early laboratory (small-scale) setups are discussed in the work of Giamei and Tschinkel.[26] The mold, situated on top of a chill plate, promotes nearly axial heat flow through the mold walls. Progressive mold immersion into the liquid-tin diminishes the heat extraction from the starter region. Heat flow is promoted both parallel and perpendicular to the withdrawal direction at different and unknown magnitudes due to the conductive and convective cooling from the chill plate and tin coolant, respectively.[24,27] For that reason, it is of particular interest to investigate changes in casting conditions and the limits of structure refinement with the LMC process. Ideally, the solid/liquid interface will be flat and maintained at the baffle zone to generate the highest thermal gradient. Since the LMC process is relatively new, there is not a sufficient understanding of the influence of processing parameters on resulting microstructure and properties. Important microstructural features that are refined by the LMC process are the primary and secondary dendrite arm spacings. Oriented <001> dendrites are aligned along the heat removal direction. Dendritic refinement can be obtained with changes in solidification

parameters and has been shown to increase fatigue resistance.[28] The cooling rate can be estimated by measurement of the average distance between dendrite cores and can be compared to experimental data measured from thermocouples during solidification. The influence of solidification parameters on the primary dendritic arm spacing (λ_1) has been treated in a model presented by Hunt[29] and is given by:

$$\lambda_1 \propto G^{-½} \bullet V^{-¼} \qquad [1.5]$$

where V is the solidification velocity, and G is the thermal gradient. It is also worthwhile to consider the influence of solidification parameters on the secondary dendrite arm spacings (λ_2). The λ_2 also has been related to the solidification parameters through a similar equation given by:[29]

$$\lambda_2 \propto (G \bullet V)^{-⅓} \qquad [1.6]$$

In order to obtain a measure of the average primary dendrite arm spacing, λ_1, over a given area, Equation 1.7 can be used,

$$\lambda_1 = n_p^{-½} \qquad [1.7]$$

where n_p is the number of primary dendrite cores per area. The average λ_2 can be measured using the line-intercept method:

$$\lambda_2 = \frac{L}{n-1} \qquad [1.8]$$

where L is the length of a line drawn next to the primary dendrite trunk which intersects n secondary arms. Both relationships have shown reasonable agreement with the observed dendritic arm spacings in microstructures of dendritically solidified castings produced using the LMC process.[25] Previous investigations have shown that primary and secondary dendrite arm spacings will decrease at higher solidification rates.[25,30]

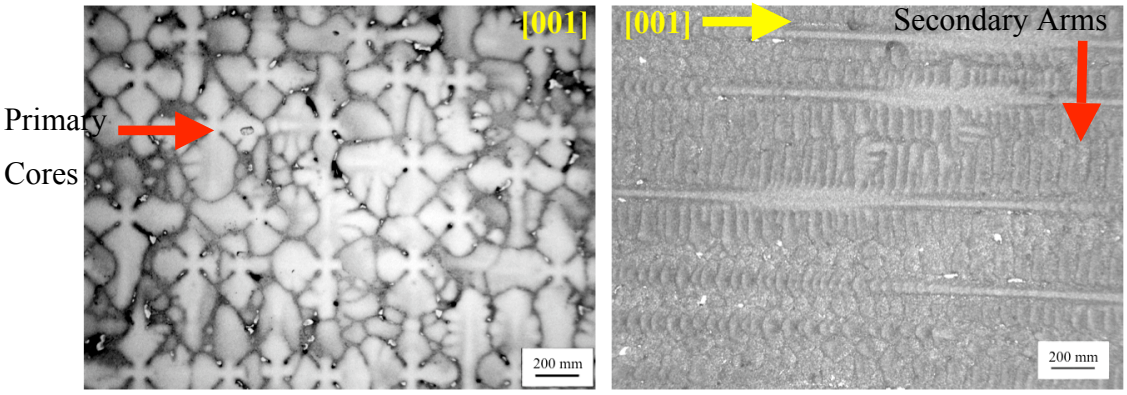

Figure 1.9 Optical images of sections of solidified bars. (a) Primary dendrite cores are shown in the transverse section with respect to the withdrawal direction (b) Secondary dendrite arms are shown in the image sliced parallel to the withdrawal direction.

Experimental studies by Elliott *et al.*[25] quantified the benefits of the LMC process by a direct comparison to the Bridgman process using large cross-section castings. Large cross-sections are defined as possessing a diameter greater than 20 mm. Elimination of freckle-type defects, a refinement in dendritic structure and a reduction in eutectic pool size and detrimental carbides were observed with laboratory experiments using LMC to cast large cross-sections. This was attributed to the capability of higher withdrawal rates while maintaining a steady, flat solid/liquid interface.[11] Increased thermal gradients using the LMC process have resulted in cooling rates 1.5 to 7.5 times greater than achieved in the Bridgman process for a casting with equal dimensions.[25] This direct comparison has highlighted the possibility of improved quality and cost reductions for large-scale turbine blades applicable in next generation IGTs.[22] However, the mechanical property improvements have not yet been fully characterized for either small- or large-scale castings, particularly the fatigue behavior. Undissolved eutectic pools, porosity and carbides that are distributed within the interdendritic regions can serve as potential initiation sites during fatigue, and should be reduced in size or eliminated in order to improve fatigue life. Additionally, the cooling rate required to suppress formation of freckle-type defects has not been addressed with LMC for small-scale castings. For that reason, the identification of the solidification parameters responsible for producing the most finely spaced dendritic structures without

solidification-induced defects for improvement of fatigue properties will be addressed in this thesis.

1.3.3 Casting Porosity

It has been reported that large casting pores can negatively effect the high cycle fatigue properties of single-crystals since they reside as stress concentration sites.[28] Microporosity (Figure 1.10) is present in nickel-base superalloys due to the dendritic solidication with freezing over a temperature range during solidification. Specifically, this involves either the rejection of gas from the liquid metal or the inability of liquid metal to feed through the interdendritic channels to compensate for shrinkage results in pores of various shapes and volumes.[31-35] For the case of superalloys, which are solidified in a vacuum, gas porosity is usually absent. Since the fluid flow in the interdendritic channels is strongly dependent on the primary and secondary arm spacing, the variation of these parameters during solidification can strongly influence the pore size and distribution.

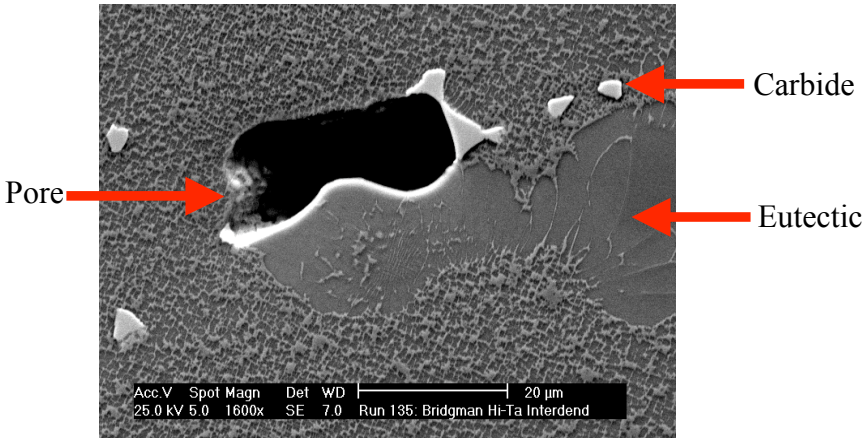

Figure 1.10 Electron image of solidification features residing in an interdendritic region of a cast superalloy detailing a pore, carbide and eutectic region.

The difference in density between the solid and liquid in the mushy zone requires the liquid to flow toward the solidifying region to prevent porosity formation. When the interdendritic liquid flows to feed solidification shrinkage, the liquid metal pressure can drop below a critical pressure, permitting the nucleation and growth of pores. It is particularly difficult to feed the shrinkage far from the dendrite tips. Pores are likely to

nucleate heterogeneously when the atmospheric pressure ($P_o \sim 1$ atm), metallostatic head pressure ($P_\rho = \rho_L g h$) and liquid-vapor surface tension pressure ($P_\sigma = 2\sigma_{LV}/r$) necessary to close the pores (with radius, r) does not exceed the local pressure to open them. Favorable conditions for pore nucleation can be expressed as[36]:

$$P_T = P_o + (2\sigma_{LV})/r + \rho_L g h - P_g - P_{MZ} \quad [1.9]$$

where g is the gravitational constant, ρ_L is the liquid metal density, h is the height of the liquid metal, and σ_{LV} is the liquid-vapor surface tension. Gas pressure (P_g) from partitioned gaseous species and the pressure drop in the mushy zone (ΔP_{MZ}) are both terms that contribute to open pores.

$$P \leq P_G - \frac{4\gamma_{LG}}{f_L \lambda_1} \quad [1.10]$$

where P_g is the pressure of the gas in the pore, γ_{LG} is the surface tension of the liquid-gas interface, and f_L is the fraction of liquid. Modeling of microporosity formation has proven to be difficult because of the issues of predicting the critical initial radius, $r_{p.}$, and finding a correlation to the interdendritic space between primary dendrite cores.[31] With that, the estimation of the maximum size within the structure should be possible using[31]

$$r_p = \frac{\lambda_1}{2} \quad [1.11]$$

However, this equation is not realistic because the solidified dendrite volume, dendritic arrangement and spacings are not taken in account.[31,32] These issues have motivated the dendrite-pore characterization technique for single crystals presented in Chapter 4. In addition, limited research has provided a connection between the solidification processing parameters to resulting defect size for single crystals.[28] Therefore, this research aims to provide a relationship between solidification processing and microstructure inhomogeneities using statistical analyses and modeling.

1.3.4 Modeling of Dendritic Array Morphology

It has been shown for various metallic materials that minimizing the variability in structure reduces the scatter in fatigue life.[37-39] Therefore, it is of interest to model the size and distribution of defects in single crystals and their correlation to the dendritic spacing distribution. Dendritic arrays have been extensively investigated to achieve a homogeneous distribution of primary spacings for a uniform distribution of mechanical properties in various directionally solidified alloys.[40-43] Tewari *et al.*[43] performed statistical analysis of the primary spacing distribution on transverse sections using Voronoi polygons in order to characterize the frequency distribution of nearest neighbors and nearest-neighbor interactions during solidification. A correlation between the overall steady-state distribution in terms of the mean primary spacing was obtained from this statistical technique.[43]

Voronoi tessellation is a tiling of space where each tile represents the space closest to a particular point. Voronoi diagrams and the associated statistics are powerful tools for analyzing spatial attributes with respect to primary dendrites grown in the <001> orientation. Optical microscopy of transversely sliced samples with respect to the withdrawal axis can provide a finite number of dendrites in a 2-D space, Figure 1.11. If every dendrite core is allocated in space, S, to its closest core, a partition of the space into a number of regions results. Such a partition is a tessellation of the space and collectively serves as a Voronoi diagram for the given set of dendrite cores where each region is designated as a Voronoi cell, V_i. A distance function is used to measure the distance of a point x from a dendrite core in the 2-D space. Let $S = \{S_1, S_2,\ldots,S_n\}$ represent a set of sites designated from dendrite cores and let $\delta(x,S_i)$ denote the distance of a point x from the site, S_i. Given two sites, S_i and S_j, the set V_{ij} of points that are closer to S_i than to S_j with respect to the distance function $\delta(x,\bullet)$ can be shown as:

$$V_{ij}=\{x \in \mathbb{R}^2 : \delta(x,S_i) < \delta(x,S_j)\} \qquad [1.12]$$

The set V_i of points on the plane, which is closer to S_i than to any other object in S, can be shown as:

$$V_i = \cap_{i \neq j} V_{ij} \qquad [1.13]$$

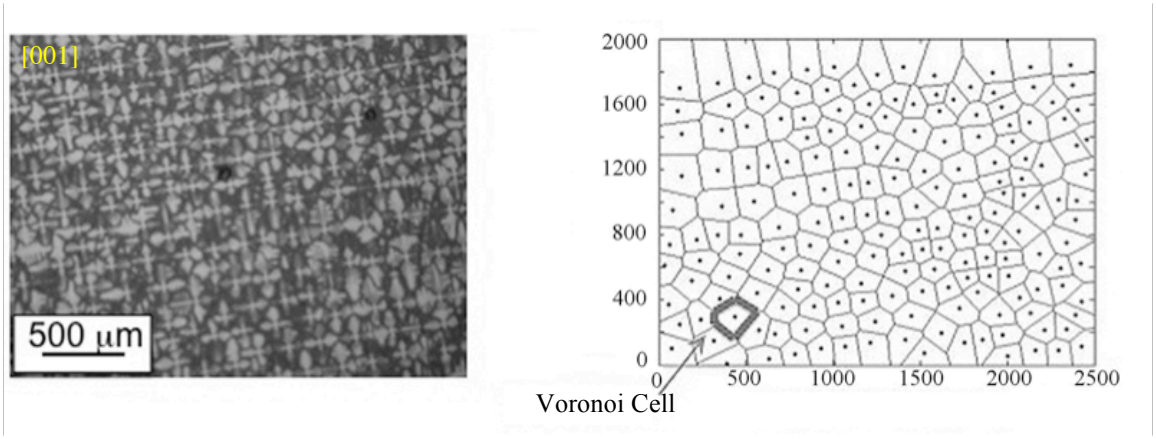

Figure 1.11 Voronoi diagram (b) constructed from optical micrograph of a René N5 alloy taken at 5X (a). Dots represent dendrite cores partitioned in 2-D space.

The locus of points on the plane that are equidistant from exactly two sites, S_i and S_j, is designated as a Voronoi bisector. A point that is equidistant to three or more objects in S is called a Voronoi vertex. A connected subset of a Voronoi bisector is a Voronoi edge. Hence, any location in a polygon is closer to its respective dendrite core than any other point in the space. Computational programs such as MATLAB® and Simulink® or CGAL can quickly produce Voronoi diagrams with points, circles and cells in a matter of seconds.

Statistical analysis of the nearest neighbor dendrite core spacing will be employed in this thesis to aid in predicting the fatigue strength of single crystals. This is only possible if there is a relationship between dendrite structure and maximum defect size. Pores, which are the focus as the major flaw, can nucleate at the root of dendrites and can be controlled by the amount of interdendritic space during solidification.[44] Since fatigue crack initiations occur at weak links in a component, modeling the heterogeneity in microstructure using Voronoi statistics is a suitable choice for constructing structure-property connections. Additionally, the conncection between fatigue life variability and microstructure heterogeneity is important, but has not been investigated to date in single crystal superalloys.

1.4 Fatigue Behavior of Single Crystals

Aircraft turbine blades experience substantial fluctuations in stress and temperature during take-off, cruise, and landing cycles, leading to a number of potential failure modes. This section will address two main fatigue failures common in single crystal turbine blades: low and high cycle fatigue. A detailed literature review of models typically used to characterize crack initiation and growth will be given in the upcoming subsections.

High cycle fatigue (HCF) has been identified as the single largest cause of component failure in modern military gas turbine engines.[45] In general, HCF involves high frequencies, low amplitudes, nominally elastic behavior and a long life ($>10^6$ cycles). The driving forces for HCF damage in turbine engines include: aerodynamic excitation, mechanical vibration, airfoil flutter and acoustic fatigue. Blades subjected to high frequency vibrations are typically designed to avoid operating near strong excitations and high vibratory stresses.[45]

In the case of low cycle fatigue (LCF), macroscopic plastic deformation occurs during every cycle and typically results in failure at less than $< 10^5$ cycles.[46] The Coffin-Manson relation displayed in Equation 1.14 can be used to represent the LCF conditions as a function of strain amplitude, ε_a. Figure 1.12 shows the relation for precipitation strengthened nickel-base superalloy 720Li.[48]

$$\varepsilon_a = CN^{-\beta} \qquad [1.14]$$

where C and β are material constants, and N represents the fatigue life. The exponent β is often on the order of -0.5.[46] The Coffin-Manson formula has been widely applied to fatigue crack life prediction.[47, 48]

The three of the most important aspects that determine fatigue life includes the cyclic plastic stress-strain response, resistance to crack initiation, and resistance to crack growth during cycling. The following sections will detail the relevant characteristics that govern the total lifetime of a blade, specifically crack initiation and propagation.

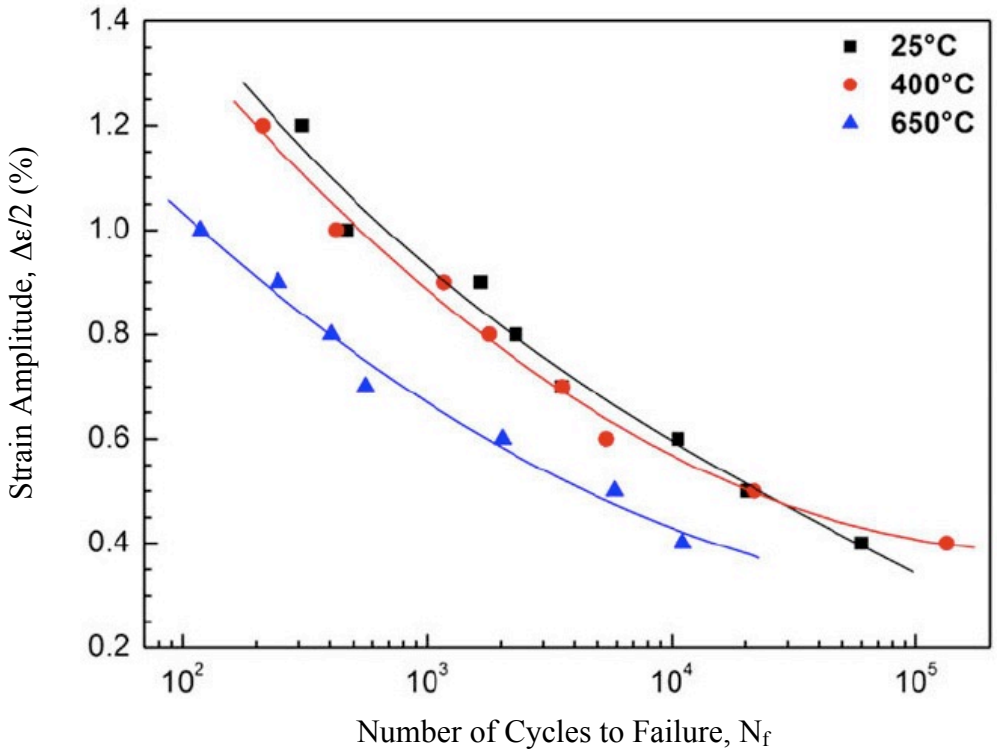

Figure 1.12 Dependence of fatigue life (N_f) on the strain amplitude ($\Delta\varepsilon/2$) for precipitation strengthened nickel-base superalloy 720Li. Figure taken from Gopinath *et al.*[48]

1.4.1 Lifetime Estimation

The total life consists of fatigue crack initiation plus growth of surface or near-surface cracks. The total fatigue life, N_T, of an initially defect-free structure can be expressed as:

$$N_T = N_I + N_P \qquad [1.15]$$

where N_I is the crack initiation period and N_P is the crack growth period, which includes stable and accelerated portions of crack propagation.[49] In high cycle fatigue, the crack initiation period is typically the dominant factor in the total service life of a component. In this thesis, crack initiation is defined as the cycles to initiate a crack from a flaw within the material. Linear elastic fracture mechanics is typically used to model long cracks using a stress intensity factor, ΔK. The issues related to both initiation and growth are presented in the following sections.

1.4.2 Crack Initiation Life

The crack initiation life of metallic materials is controlled by the cyclic plastic deformation process, where fatigue cracks initiate at locations where the stress level is higher than nominal. The development of a quantitative understanding of the crack initiation process is one of the most important aspects for characterizing and predicting the low cycle fatigue properties.

During the cyclic slip localization process, deformation takes place predominately by the generation of $\frac{a}{2}\langle 110 \rangle$ type dislocations that glide on {111} planes.[50] At low temperatures (< 427°C) and low stress levels, dislocation motion occurs mostly in the γ channels. However, at higher stress amplitudes, the dislocations generated in the γ channels can cut through the γ′ precipitates.[51-53] Therefore, it is of considerable interest to develop alloys that provide increased resistance to this localized deformation process at higher operating temperatures.

Micrometer-scale flaws such as shrinkage pores,[54-56] crevices created by oxidation effects,[57-60] carbides,[61] or indentations produced from machining are often the source of fatigue failures of turbine blades.[62] For instance, pores often serve as stress concentrators, where the pore wall represents a free surface at which the initiation process develops. This is due to the fact that the stress concentration locally enhances the dislocation processes.[63] However, the combined effect of internal casting defects and varying levels of γ/γ′ strengthening requires further investigation to understand the fatigue initiation life of these materials. A detailed analysis of the stress intensifying effect of the casting pores leading to crack initiation and the growth of short cracks is lacking.

Single crystal alloys can undergo a hot isostatic pressing (HIP) process in order to reduce or eliminate porosity and improve the fatigue resistance of a component.[64] However, a standard HIPing process at a pressure of 103.5 MPa at ~1130°C has been shown to result in internal recrystallization.[65] Furthermore, single crystal superalloys are prone to incipient melting at temperatures above the solution heat treatment range.

For optimum properties, the superalloy must be cooled from the solution heat treatment temperature at rates greater than those allowable within the HIP vessel. Subsequently, post-HIP treatment may be necessary in order to achieve the desired cooling rate, which provides a means for pore reopening due to the diffusion of alloying elements.[65]

Variability in the sizes of defects have been shown to be responsible for the fatigue scatter within cast material.[66] Crack initiation analyses have determined that the lower fatigue lives were attributed to crack initiation at large dendritic shrinkage pores located close to the specimen surface, contributing to a higher probability of initiating a crack. In some cases, a relatively small pore near the surface can initiate a crack even though larger defects may be present within the alloy.[66]

Zhang *et al*.[67] investigated the effect of cooling rate on pore size reduction during solidification on the fatigue behavior in polycrystalline Al-Si-Mg alloys. Fatigue crack initiation lives were shown to increase from 15 to 75% of the total life with a pore size decrease from ~50 μm to ~15-30 μm.[67] This delay in the initiation of fatigue cracks was attributed to the higher cooling rate and refinement in SDAS. Consequently, correlations of SDAS to fatigue life were useful in predicting the fatigue properties of the alloy. However, it is unclear how the fatigue initiation lives vary with cooling rate in single crystal superalloys. Additionally, the effect of precipitate strengthening on the cyclic slip localization process near defects has not been extensively evaluated. Thus, the motivation of this study includes understanding the crucial factors for improving fatigue: (1) reducing the defect size, or (2) manipulating the γ' structure for increasing the precipitate shearing resistance, or (3) a combination of both.

Typically, lifetime predictions ignore the initiation life and utilize crack propagation laws.[68] Therefore, the influence of crack initiation process on the total fatigue life will be evaluated in this thesis.

1.4.3 Crack Growth

The fatigue crack propagation behavior of single-crystal nickel-base superalloys is governed by interactions between deformation mechanisms, stress intensity and environmental conditions.[69] The Paris equation has been useful for characterizing the

relationship between the crack growth rate and the stress intensity range (ΔK) in the form of a power law:[70]

$$\frac{da}{dN} = C(\Delta K)^m \qquad [1.16]$$

where C and m are material constants and $\Delta K = K_{max} - K_{min}$ is the difference between the maximum and minimum stress intensity factors. This relation incorporates the number of cycles required for cracks or flaws already present in a component to grow from a subcritical size to a critical size. A schematic of the da/dN vs log ΔK is shown in Figure 1.13. Region A is the slow crack growth regime. The Paris law describes region B, where intermediate crack growth rates (in comparison to A and C) are exhibited.

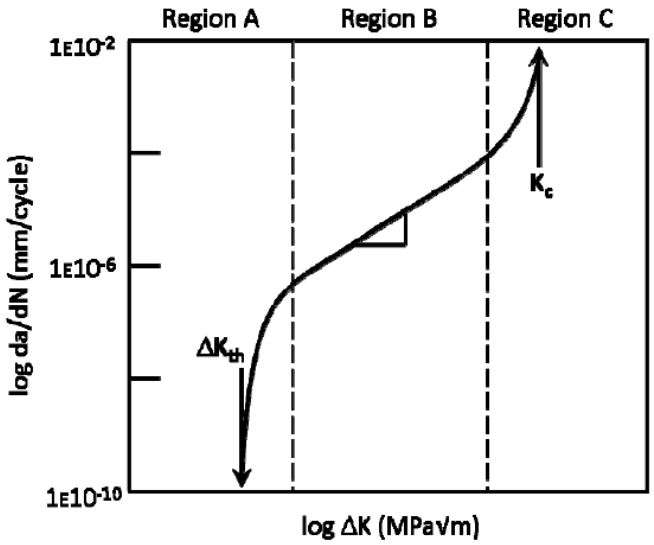

Figure 1.13 Schematic of fatigue crack growth rate vs stress intensity factor range. Adapted from Suresh.[63]

Figure 1.14 displays the crack growth behavior over a range of temperature and loading conditions for René N5.[71] Table 1.2 lists the threshold stress intensity values, ΔK_{th}, for data presented in the figure. This information will be especially useful when comparing stress intensities from defects to the threshold stress intensity (Chapter 7) for fatigue modeling purposes.

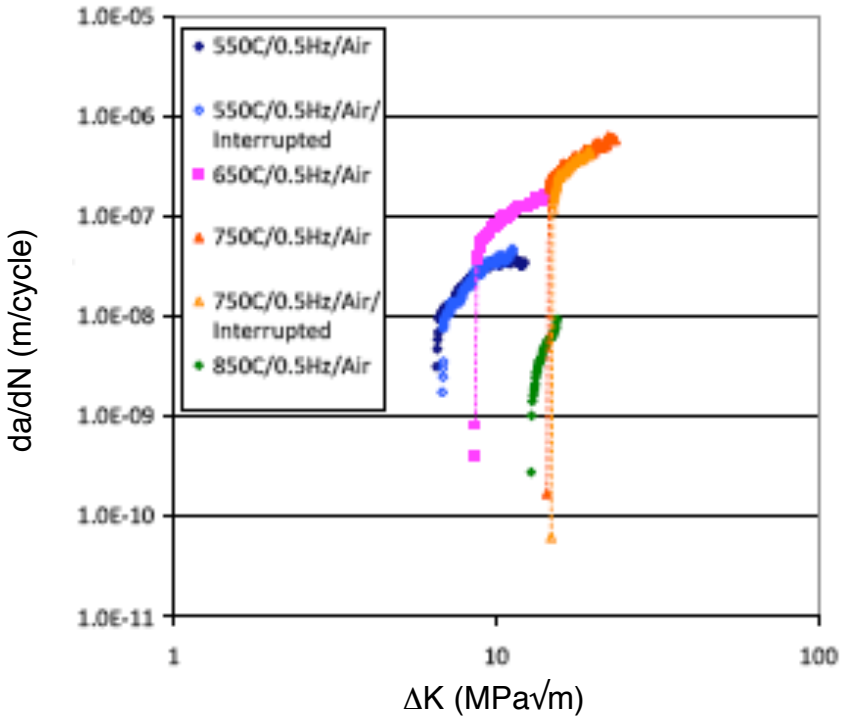

Figure 1.14 Fatigue crack growth data for specimens tested in air at 0.5 Hz with a crystal orientation of (001)[100].[71]

Table 1.2 ΔK_{th} values for René N5 specimens tested in air at 0.5 Hz with an orientation of (001)[100].

Temperature (°C)	ΔK_{th} (MPa√m)
550	6.5
650	8.5
750	14.4
850	12.9

Deviations from the Paris equation may arise due to the nature of single crystal crack growth. The modes of cracking must be identified since cracks are not necessarily propagating in a Mode I manner early in the crack growth regime. Therefore, it is worthwhile to briefly review the failure modes that may be associated with material anisotropy and variations in crystal orientation. The three basic modes are schematically shown in Figure 1.15. In addition to Mode I (tensile opening), Mode II is characterized as in-plane sliding, and Mode III as tearing or anti-plane shear.

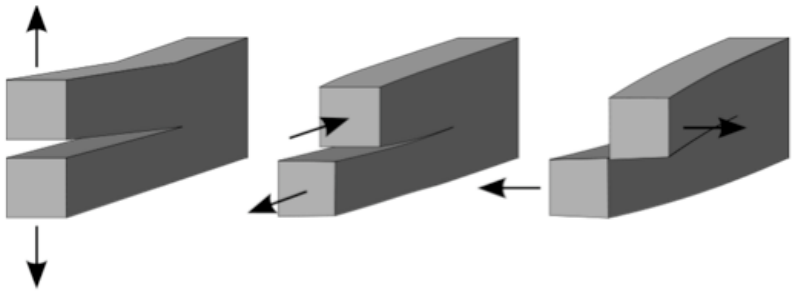

Mode I: Opening | Mode II: In Plane Shear | Mode III: Out of Plane Shear

Figure 1.15 Various modes of fracture for metals.[63]

The combination of all modes of loading must be considered in determining the stress intensity factor at the crack tip for characterization of the fatigue crack propagation in Ni-base single-crystals. Due to the two-phase microstructure in nickel-base superalloys, fracture modes include (1) non-crystallographic fracture perpendicular to the stress axis[72] and (2) crystallographic crack propagation along specific slip planes, as shown in Figure 1.16.

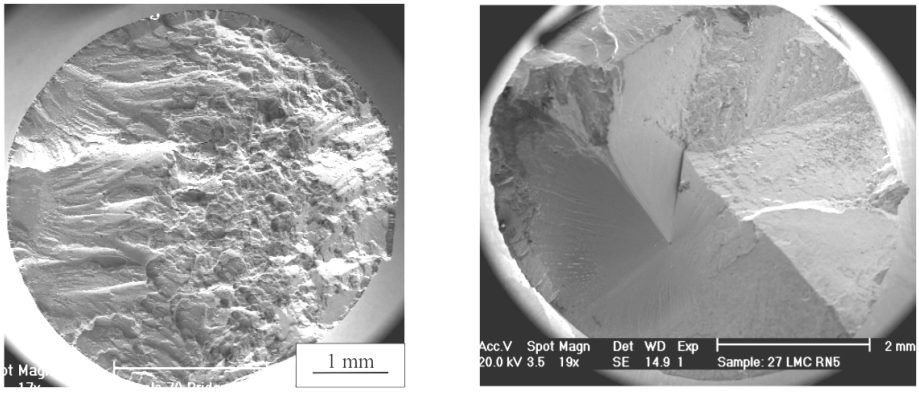

(a) (b)

Figure 1.16 Fracture surface of a nickel-base superalloy exemplifying (a) a full fracture perpendicular to the applied stress axis and (b) a fatigue crack which emanated from a casting pore and propagated crystallographically.

In single-crystal alloys, cracks may proceed crystallographically along {111} planes in the early stages of growth, and then may advance in a less crystallographic manner.[73] With linear elastic fracture mechanics (LEFM) theory, finite element analysis (FEA) techniques can be used to characterize cracks that have propagated in Mode I, II, III or mixed mode configurations to obtain stress intensities for fatigued single-crystals of K_I, K_{II} and K_{III}, respectively. Stress intensity factors can be derived by measurement of

the displacement field near the crack tip as functions of the distance, r, and angle, θ, (Figure 1.17). The stress field near the crack tip can be shown as[74,75]

$$\sigma_i(r,\theta) = \frac{1}{\sqrt{2\pi r}}[K_I f_i(\mu,\theta) + K_{II} g_i(\mu,\theta) + K_{III} h_i(\mu,\theta)] \quad (i=1,\ldots,6) \qquad [1.17]$$

where f_i, g_i and h_i are geometrical functions defining the angular dependency of the stress field. For an infinite plate with a crack with length $2a$ and subjected to a normal stress σ_y and shear stresses τ_{xy} and τ_{yz}, the stress intensity factors can be defined as[76]

$$K_I = \sigma_y \sqrt{\pi a} \qquad [1.18]$$

$$K_{II} = \tau_{xy} \sqrt{\pi a} \qquad [1.19]$$

$$K_{III} = \tau_{yz} \sqrt{\pi a} \qquad [1.20]$$

The stress field also depends on the complex roots, μ_i, of the characteristic equation[74]

$$a_{11}\mu^4 - 2a_{16}\mu^3 + (2a_{12} + a_{66})\mu^2 - 2a_{26}\mu + 2a_{26}\mu + a_{22} = 0 \qquad [1.21]$$

where the coefficients a_{ij} are the compliance elements of the elastic constitutive matrix, relating stresses and strains according to

$$\varepsilon_i = a_{ij}\sigma_{ij} \quad (i, j = 1,\ldots,6) \qquad [1.22]$$

Previous work[76] has shown that Mode I stress intensity factor solutions often cannot be used for the anisotropic nickel-superalloys, since cracks often propagate along {111} octahedral planes at specific angles with respect to the tensile axis. To model the crack propagation behavior in single crystal materials, stress intensity factors should be determined for cracks propagating perpendicular to the stress axis as well as for cracks that grow at high angles of inclination.

Cracks can transition from crystallographic to non-crystallographic propagation modes and vice-versa during fatigue.[73] Temperature and stress intensity have been

shown to exert considerable influence on the initiation and transition of crystallographic to non-crystallographic cracking.[69] Non-crystallographic cracking is defined here as propagation of a crack normal to the stress axis. Telesman and Ghosn[77] have observed the fatigue crack growth (FCG) rate proportional to the applied ΔK at stress intensities above 8 MPa-$m^{1/2}$ and a crack growth rate independent of the applied ΔK below that value for PWA 1480. Understanding the driving force for each mode during fatigue is critical for predicting the total life of an alloy.

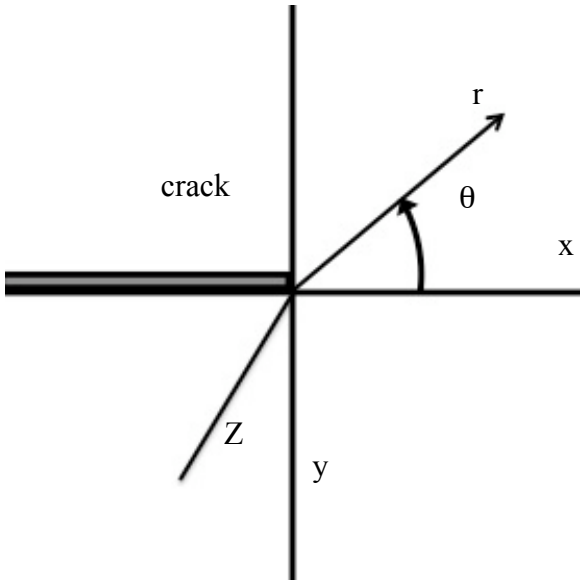

Figure 1.17 Definition of the variables *r* and *θ* and the crack tip local coordinate frame.[76]

1.4.4 Fatigue Life Prediction

In practice, fatigue life predictions for aircraft components utilize a fracture mechanics approach, specifically, the number of cycles to failure for a given defect size.[78] Numerous studies on single crystals have focused on characterizing the fatigue crack growth rate and fatigue threshold data in order to develop life prediction models.[79-82] It has been suggested that the threshold region is very important if a significant portion of the life of a component is spent in this region.[83] Since the near-threshold crack growth rate and the fatigue threshold are known to be microstructurally sensitive,[84] microstructural modifications appear to be the critical factor in improving the crack growth resistance within this domain.

Recently, the fatigue life of superalloys has been estimated using the Paris-Erdogen crack growth law to model the initial subsurface crack growth from pores.[85] This approach requires a mechanistic based understanding of the complex stress states, subsurface failures and various temperature/environment regimes. A schematic of a deterministic fracture mechanics based lifing model has been shown to explain the variability in fatigue life in terms of the sizes and locations of micropores, Figure 1.18.[86] However, factors that require further investigation include multiple initiations originating from porosity and carbides, the role of γ/γ' strengthening arising from varying alloy composition, and the applicability of a model across a range of alloys. These issues will be addressed in later sections of this dissertation.

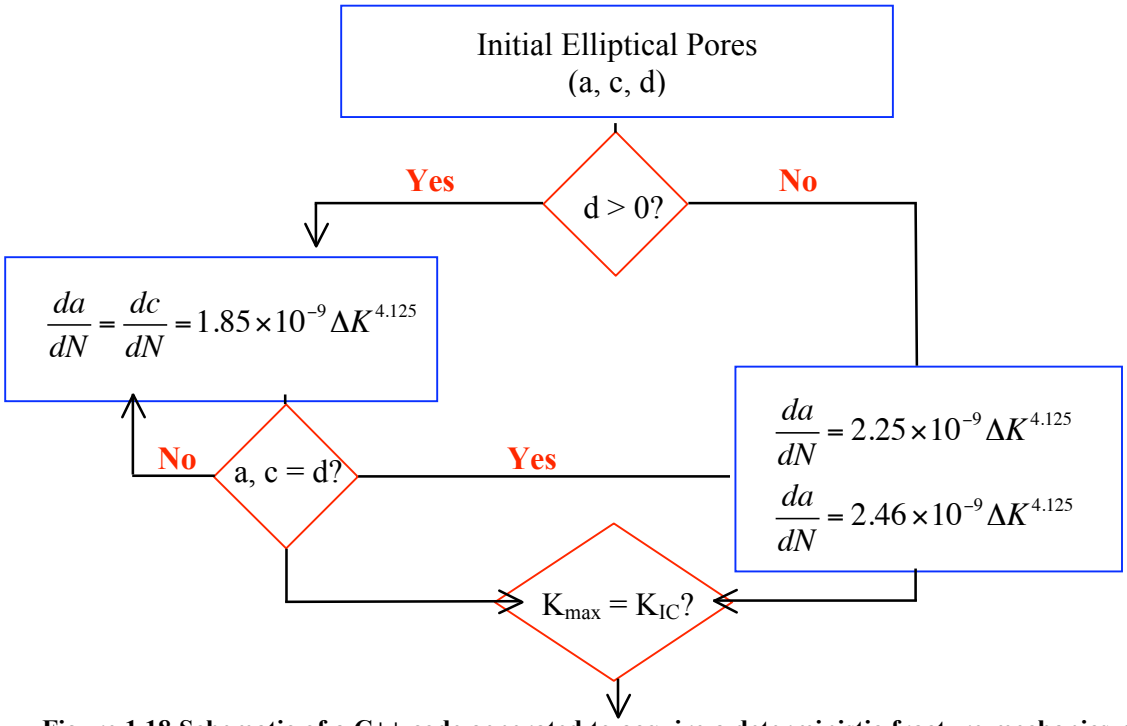

Figure 1.18 Schematic of a C++ code generated to acquire a deterministic fracture mechanics model. The variables a and c represent the major and minor axes of the elliptical casting pores, and d is the distance below the notch root.[86]

1.5 Research Motivations and Objectives

In order to introduce an advanced alloy and/or newer solidification process at the industrial scale, the mechanical properties must first be quantified. However, with the multitude of multicomponent compositions and the complex blade geometries, the task of selecting optimal conditions can be extremely laborious and costly. An engineering approach that enables the optimization of the materials, manufacturing processes and

component design in advance of component fabrication is highly desirable. Once manufacturing processing-structure-mechanical property relations are developed and are applicable to a variety of alloys, reductions in component design and process development costs and cycle times can be attained.

The current investigation focuses on gaining an increased understanding of critical features associated with higher gradient solidification processing approaches and resulting microstructure heterogeneities that influence the observed fatigue properties. The study of these particular properties is useful in that improvement in solidification techniques and alloy chemistries may lead to increased service lives of newer classes of superalloy single crystals. In order to improve fatigue properties of single crystal alloys, a microstructure-based fatigue model is needed to guide alloy and process design. Of considerable relevance to any microstructure-based fatigue model for cast alloys is the dependence of crack initiation on the dendritic structure, the size and distribution of pores and carbides, temperature and loading parameters. Additionally, an assessment of the relative dominance of fatigue crack initiation compared to fatigue crack propagation is needed. René N5, which is a second-generation single crystal superalloy, and a modified René N5 alloy with an increased amount of Ta content have been studied. These alloys were selected due to their widespread use in aircraft engines.

The overall objective of this research has been to develop a processing-structure-property model that can be applicable to a range of single crystal superalloy compositions and solidification conditions. Since higher thermal gradient casting processes are currently under investigation as a means to grow refined single crystal airfoils, a model that captures the major process parameters will be useful for developing new materials that benefit from the high gradient processing and structure. Additionally, a phenomenology for quantifying the life-limiting solidification features at various withdrawal rates was an aim of this research. Finally, identifying a connection between the solidification parameters and the fatigue life was a final objective. Experimental procedures will be presented in Chapter 2, while Chapter 3 examines the solidification experiments, which utilized the Bridgman and LMC processes. Microstructural characterization and modeling of the solidification structure and pores formed using

statistical analyses are presented in Chapter 4. The LCF behavior and the influence of temperature on the crack propagation mode will be addressed in Chapter 5 and 6, respectively. Chapter 7 describes a simple model that connects processing parameters to fatigue lives for the investigated alloys with consideration of key microstructural features of the system. Chapter 8 summarizes the major conclusions and provides recommendations for future studies.

---

[1] N.S. Cheruvu: *J. of Eng. Gas Turb. Power*, 1999, 3, pp. 484-453.

[2] T.M. Pollock and S. Tin: *J. of Prop. Power*, 2006, pp. 361-74.

[3] R.C. Reed: *The Superalloys: Fundamentals and Applications,* Cambridge, Cambridge University Press, 2006.

[4] E.N. Kablov and N.V. Petrushin: *Pure Appl. Chem*., 2004, 76, pp. 1679-1689.

[5] R. Schafrik, S. Walston: in *Superalloys 2008*, R.C. Reed, K.A. Green, P. Caron, T.P. Gabb, M.G. Fahrmann, E.S. Huron, eds., Seven Springs, PA, TMS, 2008, pp. 3-9.

[6] J.D. Nystrom, T.M. Pollock, W.H. Murphy, and A. Garg: *Metall. Trans. A,* 1997, 28A, pp. 2443-2452.

[7] M.J. Donachie and S.J. Donachie: *Superalloys: A Technical Guide*, Materials Park, OH, ASM International, 2002).

[8] D.N. Duhl: *Superalloys II,* John Wiley & Sons Inc., 1987, pp. 198-200.

[9] M. Gell, D.N. Duhl, and A.F. Giamei: in *Superalloys 1980*, J.K. Tien, S.T. Wlodek, H.I. Morrow, M. Gell, and G.E. Mauer, eds., Seven Springs, PA, TMS 1980, pp. 205- 214.

[10] E.W. Ross and K.S. O'Hara: in *Superalloys 1996*, R.D. Kissinger, D.J. Bye, D.L. Anton, A.D. Cetel, M.V. Nathal, T.M. Pollock, and D.A.Woodford, eds., Warrandale, PA, TMS 1996, pp. 19-25.

[11] S. Tin, T.M. Pollock, and W.Murphy: *Metall. Trans. A*, 2001, 32, pp. 1743-1753.

[12] D.A. Porter and K.E. Easterling: *Phase Transformations in Metals and Alloys*, Stanley Thornes Ltd, Cheltenham, 1992.

[13] T.M. Pollock and R.D. Field: in *Dislocations in Solids Vol. 11*, F.R.N. Nabarro, M.S. Duesbery, eds., Amsterdam, Elsevier, 2002.

[14] S.M. Copley, A.F. Giamei, S.M. Johnson and M.F. Hornbecker: *Met. Trans*., 1977, 1, pp. 2193.

[15] E.N. Kablov, I.L. Svetlov and N.V. Petrushin: Materialovedenie, 1997, 4, pp. 32-38.

[16] M. Gell, D.N. Duhl, and A.F. Giamei: In Superalloys 1980, J.K. Tien, S.T. Wlodek, H.I. Morrow, M. Gell, and G.E. Mauer, eds., Seven Springs, PA, TMS 1980, pp. 205- 214.

[17] D.R. Askeland and P. Phulé: *The Science and Engineering of Materials 4th Edition*, Thomson-Brooks/Cole, 2006.

[18] G.K. Bouse and J. R. Mihalisin: in *Superalloys, Supercomposites and Superceramics*, J. K. Tien, and T. Caulfield, eds., San Diego, CA, Academic Press, 1989, pp. 99–148.

[19] A.J. Elliott: *PhD. Thesis*, University of Michigan, Ann Arbor, 2005.

[20] H.S. Carslaw and J.C. Jaeger: *Conduction of Heat in Solids,* Oxford, Clarendon Press, 1959.

[21] S. Tin, T.M. Pollock, and W. Murphy: *Metall. Mater. Trans. A*, 2001, 32A, pp. 1743-1753.

[22] A.J. Elliott, S. Tin, W.T. King, S.-C. Huang, M.F.X. Gigliotti, and T.M. Pollock: *Metall. Trans. A*, 2004, 35, pp. 3221-3231.

[23] T.J. Fitzgerald and R.F. Singer: *Metall. Trans. A*, 1997, 28, pp. 1377- 1383.

[24] M. Gell, C.P. Sullivan, and F.L. Versnyder: in *Solidification Technology*, J.J. Burke, M.C. Flemings, and A.E. Gorum eds., Chestnut Hill, MA, Brook Hill, 1974, pp. 141-164.

[25] A.J. Elliot, GB. Karney, M.F.X Gigliotti, and T.M. Pollock: in *Superalloys 2004*, K.A. Green, H. Harada, T.E. Howson, T.M. Pollock, R.C. Reed, J.J. Schirra, S Walston, eds., Seven Springs, PA, TMS, 2004, pp. 421-430.

[26] J.G. Tschinkel, A.F. Giamei, and B.H. Kearn: 1973, U.S. Patent # 3,763,926.

[27] J.D. Miller and T.M. Pollock: in *Proceedings of the 2009 International Symposium on Liquid Metal Processing and Casting,* P.D. Lee, A. Mitchell and R. Williamson, eds., AVS, 2009, pp. 119-126.

[28] M. Lamm and R.F. Singer: *Metall. Trans. A*, 2007, 38, pp. 1177-1183.

[29] J.D. Hunt: in *Proc. Conf. on Solidification and Casting of Metals*, J.D. Hunt, eds., Metals Society, London, 1979, pp. 3.

[30] A. Kermanpur , N. Varahraam, E. Engilehei, M. Mohammadzadeh and P. Davami: *Mater. Sci. Tech.*, 2000, 16, pp. 579.

[31] D.R. Poirier, K. Yeum, and A.L. Maples: *Metall. Trans A,* 1987, 18, pp. 1979.

[32] K. Kubo and R.D. Pehlke: *Metall. Trans. B,* 1985, pp. 359.

[33] D. Argo and J.E. Gruzleski: *Trans. AFS,* 1989, 96, pp. 67.

[34] G.K. Sigworth and C. Wang: *Trans. AFS,* 1992, 100, pp. 979.

[35] G.K. Sigworth and C. Wang: *Metall. Trans B,* 1993, 24, pp. 349-364.

[36] H.S. Whitesell and R.A. Overfelt: *Mater. Sci. Eng. A*., 2001, A318, pp. 264-276.

[37] D.L. McDowell, K. Gall, M.F. Horstemeyer and J. Fan: *Eng. Fract. Mech.*, 2003, 70, pp. 49-80.

[38] J.Z. Yi, P.D. Lee, T.C. Lindley, and T. Fukui: *Mater. Sci. Eng. A*, 2006, A432, pp. 59-68.

[39] S.K. Jha, M.J. Caton, and J.M. Larsen: *Mater. Sci. Eng. A*, 2007, A468-470, pp. 23-32.

[40] P. Zhao, M. Vénere, J. Heinrich, and D.J. Poirier: *J. of Comp. Phys*. 2003, 188, pp. 434-461.

[41] B. Billia, H. Jamgotchian, and H. Nguyen Thi: *Metall. Trans A*, 1991, 22A, pp. 3041-50.

[42] N. Noel, H. Jamgotchian, and B. Billia: *J. of Crys. Growth*, 1997, 181, pp. 117-32.

[43] S.N. Tewari and Y-Hsuan Weng: *Metall. Trans A*, 2002, 33 pp. 1229-43.

[44] R. Cahn and P. Haasen: *Physical Metallurgy 4th Edition*, Elsevier Science, Amsterdam, The Netherlands, 1996.

[45] T. Nicholas: *High Cycle Fatigue*: *A Mechanics of Materials Perspective*, Elsevier Ltd., London, 2006

[46] J. Schijve: *Fatigue of Structures and Materials*, Springer-Verlag New York, Inc., New York, 2008.

[47] S.S. Manson: *Thermal Stress and Low Cycle Fatigue*, McGraw-Hill, New York, 1966.

[48] K. Gopinath, A.K. Gorgia, S.V. Kamat, R. Balamuralikrishnan, and U. Ramamurty: *Acta Mater.*, 2007, 57, pp. 3450-3459.

[49] B. Bhattacharya and B. Ellingwood: *Int. J. Fatigue*, 1998, 20, pp. 631-639.

[50] G.E. Dieter: *Mechanical Metallurgy*, McGraw-Hill, London, 1988.

[51] J.H. Zhang, Z.Q. Hu, Y.B. Xu, and Z.G. Wang: *Metall. Mater. Trans. A.,* 1992, 23, pp. 1253-1258.

[52] V. Brien and B. Decamps: *Mater. Sci. Eng. A,* 2001, 316, pp. 18-31.

[53] D.W. MacLachlan and D.M. Knowles: *Fatigue Fract. Engng. Mater Struct*., 2001, 24, pp. 503–21.

[54] Y. Murakami and S. Nemat-Nasser: *Eng. Fract. Mech.,* 1983, 17, pp. 193-210.

[55] K.L. Miller: *Mater. Sci. Tech*., 1993, 9, pp. 453-462.

[56] G. Jianting, D. Ranucci, E. Picco, and P.M. Strocchi: *Int. J. Fatigue,* 1984, 6, pp. 95- 99.

[57] M. Reger and L. Remy: *Metall. Trans. A.,* 1988, 19, pp. 2259-2268.

[58] E. Fleury and L. Remy: *Mater.* Sci. *Engng.,* 1993, 167, pp. 23.

[59] S. D. Antolovich, S. Liu, and R. Baur: *Metall. Trans. A,* 1981, 12, pp. 473-481.

[60] J. Reuchet and L. Remy: *Mater. Sci*. *Engng.,* 1983, 59, pp. 33-42

[61] J. Reuchet and L. Remy: *Mater. Sci. Engng*, 1983, 58, pp. 19-32

[62] Q. Huang and X. Ren: *Int. J. Fatigue,* 1991, 13, pp. 322-326.

[63] S. Suresh: *Fatigue of Materials 2nd Edition,* Cambridge, University Press, 1998.

[64] Wasson and Fuchs: in *Superalloys 2008*, R.C. Reed, K.A. Green, P. Caron, T.P. Gabb, M.G. Fahrmann, E.S. Huron, eds., Seven Springs, PA, TMS, 2008, pp. 489-497.

[65] L.G. Fritzemeier: 1987, U.S. Patent # 5,573,609.

[66] D. Eylon and B. Strope: *J. of Mater. Sci.*, 1979, 14, pp. 345-353.

[67] B. Zhang, W. Chen, and D.R. Poirier: *Fatigue and Frac. Engng. Mater. Struct.,* 2000, 23, pp. 417-423.

[68] M.D. Miller, P.A.S. Reed, M.R. Joyce, M.B. Henderson, J. Brooks, I.M. Wilcock: *Mater. Sci. Tech*., 2007, 23, pp. 1439-1445.

[69] N.K. Arakere and J. Moroso: *High Temp. Mater. Processes,* 2001, 20, pp. 117.

[70] P. Paris and F. Erdogan: *Trans. ASME J. of Basic Eng.*, 1963, 85, pp. 528-534.

[71] C. Yablinsky, *Ph.D. Thesis*, The Ohio State University, Columbus, OH, 2010.

[72] S. Cunningham, D. DeLuca, and F. Haake: Report WL-TR-94-4089, Wright Laboratory, 1996.

[73] J.S. Crompton and J.W. Martin: *Metall.. Trans A*, 1984, 15, pp. 1711-1719.

[74] G.C. Sih, P.C. Paris, G.R. Irwin: *Int. J. Fract. Mech.,* 1965, 1, pp. 189–203.

[75] A.C. Pickard: *in The application of 3-dimensional finite element methods to fracture mechanics and fatigue life prediction*, London, Chameleon Press Ltd, 1986.

[76] T. Tinga: *Engng. Fract. Mech*., 2006, 73, pp. 1679-1692.

[77] J. Telesman and L.J. Ghosn: *J. of Eng. Gas Turb. Power,* 1996, 118, pp. 399–405.

[78] B.A. Cowles: *Int. J. Fatigue*, 1996, 80, pp. 147-163.

[79] A. Sengupta, S.K. Putatunda, and M. Balogh: *J. Mat. Eng. Performance*, 1994, 3, pp. 540-549.

[80] R. Naik, D.P. DeLuca, and D.M. Shah*: J. Eng. Gas. Turb. Power*, 2004, 126, pp. 391-400.

[81] J.Z. Yi, C.J Torbet, Q. Feng , T.M. Pollock, and J.W. Jones: *Mater. Sci. Eng A* 2007, 443, pp. 142–9.

[82] D.W. MacLachlan, D.M. Knowles: *Fatigue Fract. Engng. Mater Struct*., 2001, 24, pp. 503–21.

[83] P. Lukáš , L. Kunz: *Int. J. Fatigue*, 2003, 25, pp. 855-862.

[84] D.L. McDowell: *Mater. Sci. Eng.,* 2007, 468-470, pp. 4-14.

[85] M.D. Miller, P.A.S. Reed, M.R. Joyce, M.B. Henderson, J.W. Brooks, I. Wilcock, and X. Wu: *Mater. Sci. Tech*., 2007, 23, pp. 1439-1445

[86] P.A.S. Reed and M.D. Miller: in *Superalloys 2008*, R.C. Reed, K.A. Green, P. Caron, T.P. Gabb, M.G. Fahrmann, E.S. Huron, eds., Seven Springs, PA, TMS, 2008, pp. 527-533.

Chapter 2

EXPERIMENTAL PROCEDURES

In this chapter the procedures used to conduct solidification, fatigue experiments and the associated material structure analysis are described. Solidification experiments were conducted with the Bridgman and LMC casting processes with René N5 and a modified René N5 alloy at various solidification rates. Microscopy preparation approaches and image processing techniques are detailed. Finally, procedures for strain-controlled low cycle fatigue testing and the conditions for the displacement controlled cycling at ultrasonic frequencies are described.

2.1 Solidification Experiments

Laboratory-scale cylindrical bars of a René N5 and modified René N5 modified single-crystal, nickel-base superalloy (Table 2.1) were solidified by both conventional Bridgman and liquid-metal cooled (LMC) processes in an interchangeable ALD Vacuum Technologies furnace located at the University of Michigan.

Table 2.1 Elemental composition (wt%) of 2nd generation single-crystal nickel-base superalloy.

	Cr	Co	Mo	W	Ta	Re	Al	Hf	C	Y	Ni
René N5	7.00	7.50	1.50	5.00	6.50	3.00	6.20	0.15	0.05	0.01	bal
René N5+Ta	7.07	7.60	1.50	5.14	9.26	3.09	5.63	0.14	0.06	0.01	bal

The Bridgman setup utilized a 150 mm diameter water-cooled copper chill plate to support the mold (Figure 1.7), whereas a stainless steel chill plate of the same dimension was used in the LMC setup (Figure 1.8). The cooling container held a 500 kg

Sn bath maintained at ~250°C. A stirrer and re-circulating thermal oil system, which was monitored by thermocouples, maintained control of the tin-bath temperature. A ceramic baffle floated atop the tin-bath surface to provide thermal insulation of the cooling medium (tin-bath) from the mold heater. A mixture of hollow and solid zirconium silicate beads, ranging from ~0.5 to 1.5 mm in diameter was utilized as the floating baffle (Figure 2.1). The average baffle thickness was maintained at ~1.5 cm for all castings as measured from three locations near the rim of the container holding tin-bath.

Figure 2.1 Ceramic beads comprised in the baffle used in the LMC casting process.

A vacuum of at least 10^{-4} mbars was obtained before the start of the casting process. The ingot, contained in an alumina crucible, was suspended above the mold heater within an induction coil. The ingot was induction melted by the coil at a temperature of approximately 1550^{o}C. The ingot pour was controlled by a higher melting of 99.9% pure nickel "penny" at the base of the crucible. The removal of the mold from the furnace at a specified withdrawal rate was initiated after complete pouring of the molten metal into the preheated (1550^{o}C) investment mold. A computer controlled mechanical arm attached to the chill plate withdrew the mold into the tin bath. The starting position of the mechanical arm was approximately 1 cm above the baffle/tin-bath surface. The mold heater was shut down only upon the completion of the withdrawal at a pre-set end position in the tin bath.

Cylindrical bars of 1.6 cm diameter were cast using a six-bar mold configuration from investment molds supplied by PCC Airfoils (Beachwood, OH) (Figure 2.2) using varying withdrawal rates, see Table 2.2. The cylindrical bars were spaced evenly from the

center in a radial configuration to maintain similar thermal conditions. Nickel plugs below a pigtail bend or seeded starters were used to control grain nucleation to produce a [001] oriented single-crystal. Each of the six cylindrical bars was extracted from the mold following solidification.

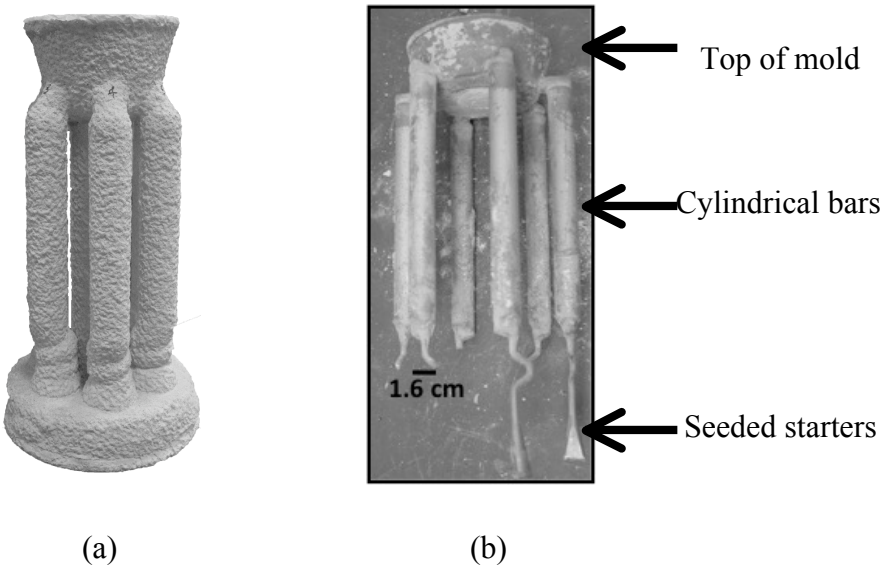

Figure 2.2 (a) Investment mold utilized in the Bridgman and LMC casting processes. (b) Ceramic mold and tin remnants removed post-casting to reveal the 6-bar mold-configuration for grown single-crystals.

Table 2.2 Bridgman and LMC withdrawal velocities used for growing single crystals during each casting run.

Process	Withdrawal Rate	Alloy	Total Number of Casting Runs
Bridgman	3.4 mm/min	René N5	4
Bridgman	3.4 mm/min	René N5 + Ta	4
LMC	8.5 mm/min	René N5	1
LMC	12.7 mm/min	René N5	6
LMC	12.7 mm/min	René N5 + Ta	4
LMC	14.8 mm/min	René N5	1
LMC	21.2 mm/min	René N5	1

Residual tin-bath and the remnant mold material were removed from the cast surface by the use of sandpaper. Macroetching of the bars was performed for surface

defect identification by submerging cast bars in a solution of 80 ml HCl: 2mL HNO_3: 11 mL H_2O: 16 g $FeCl_3$ for about an hour. The crystallographic orientation of each cylindrical bar was determined by Laue back-reflection X-ray diffraction techniques, and was performed at PCC Airfoils. A standard René N5 solution (1290^oC, 4 hours), first ageing treatment (1120^oC, 4 hours) and second ageing treatment (1080^oC, >10 hours) were subjected to the cast bars at Metcut Research Laboratory (Cincinnati, OH).

2.2 Microstructural Characterization

Dendrite arm spacings were characterized by manual point count, line-intercept, and digital methods. This section will detail the metallographic preparation for optical microscopy and the integration of image processing techniques for measurement of solidification-induced microstructural features.

2.2.1 Manual Dendrite Arm Spacing Procedure

Optical microscopy was performed on polished and etched (33 mL glacial acetic acid: 33 mL H_2O: 33 mL HNO_3: 1 mL HF) sections from transverse and longitudinally sliced locations with respect to the withdrawal axis. Microstructures were obtained for each withdrawal rate and analyzed for primary and secondary dendrite arm spacings. Transverse slices with respect to the solidification direction allowed for PDAS measurement (λ_1) based on Equation 1.7.[1] Areas of at least 4 mm^2 were used for calculation in order to image a statistically significant number of dendrites for comparison. Secondary dendrite arm spacings (λ_2) were measured according to Equation 1.8 based on the line-intercept method[2] using longitudinal slices of the bars with respect to the withdrawal axis.

2.2.2 Microstructure Modeling Using Voronoi Tessellations

Statistical and spatial analyses were carried out to characterize the heterogeneity in microstructure. For select specimens, individual sampling of nearest neighbors was performed using a Voronoi methodology detailed in Chapter 1. Voronoi maps were constructed from a series of polygons formed around dendrite cores using a MATLAB program.[3] Neighbors of dendrite cores were defined as any core whose polygon shares

a border with the selected core. For example, in Figure 1.11 the dendrite cores are represented by dots with the bold, highlighted polygon as a single Voronoi-dendrite cell. Additionally, Voronoi-dendrite maps were generated to display the quantity of nearest-neighbor dendrite cores represented by color and the enlarged number shown in Figure 2.3.

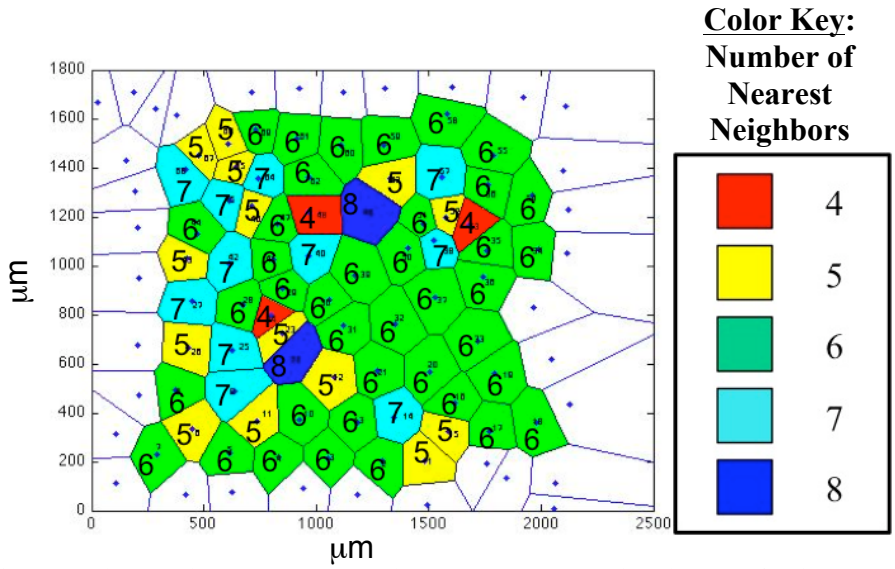

Figure 2.3 Voronoi-dendrite cell plot modeling a transverse optical image of primary dendrite cores. The enlarged numbers and colors indicate the number of nearest-neighbor dendrite cores

The region enclosed in each cell contains the area closest to that dendrite core. Each specimen was treated as a population of primary dendrite arms within each optical micrograph. Since most cells were six-sided, a regular hexagon was used to approximate the cell diameter, D,

$$D = \left(\frac{2A}{\sqrt{3}}\right)^{\frac{1}{2}} \qquad [2.1]$$

where A is the area of a Voronoi cell.

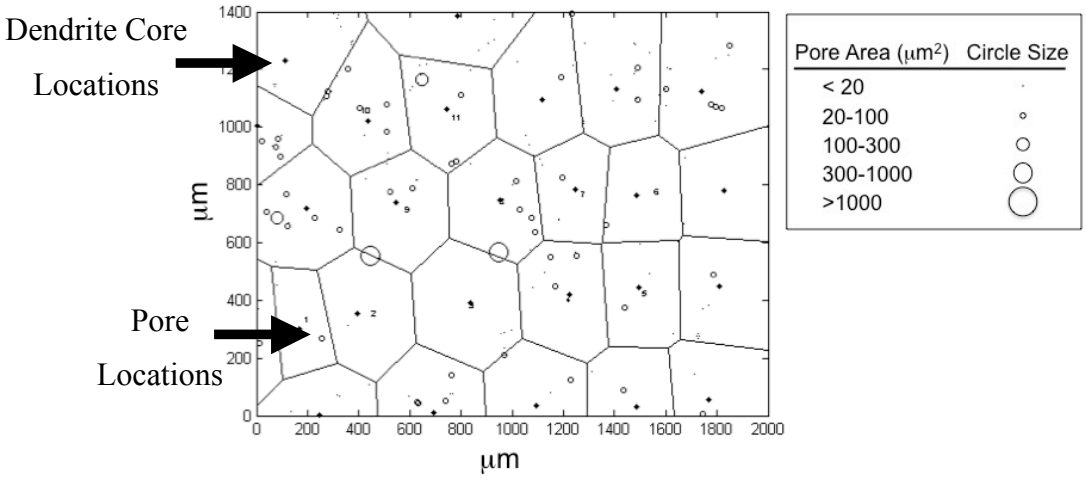

Figure 2.4 Corresponding Voronoi diagram with associated pore locations for a transverse optical image of a Bridgman cast nickel-base superalloy

Pore area measurements with their respective X-Y coordinates were acquired with ImageJ[4] software and transposed onto Voronoi maps by using circles in order to identify a pore-dendrite spatial correlation, as well as to quantify large pores and clustering. In the Voronoi maps, ranges of pore areas were designated with circles of specific sizes, indicated in Figure 2.4. It should be noted that the Voronoi polygons are constructed only with respect to the dendrite cores.

2.3 Mechanical Testing

Various mechanical tests were employed to measure the fatigue life, strength and creep life of the solidified alloys. Electron microscopy was performed on post-failed samples to obtain an understanding of the failure mechanisms.

2.3.1 Strain-Controlled Low Cycle Fatigue Testing

Heat-treated bars were machined into threaded uncoated specimens at (Figure 2.5) and subjected to strain-controlled low cycle fatigue at 538^{o}C until failure using a computer controlled servohydraulic testing system. Both machining and testing was performed at Metcut Research Laboratory in Cincinnati, OH. The nominal loading axis was in the [001] crystal growth direction. The LCF tests, based on testing specification E50TF148, were performed in air at total strain-ranges, $\Delta\varepsilon_t$, between 0.6 and 1.1%. A specific strain range used for cycling was based on the selection of an alternating

pseudostress, which ranged between 380 and 620 MPa, using a R-ratio of 0. The pseudostress amplitude is defined as

$$\sigma_p = \frac{\Delta\varepsilon_t E}{2} \qquad [2.2]$$

where E is the Young's modulus. Using the alternating pseudostress for the fatigue damage parameter is the normal method for presenting S-N results for strain cycle fatigue at GE Aviation. This strategy has been used for many decades for direct comparisons with many engineering analyses conducted at General Electric. Therefore, the fatigue results will be presented with a y-oridinate as alternating (pseudo) stress.

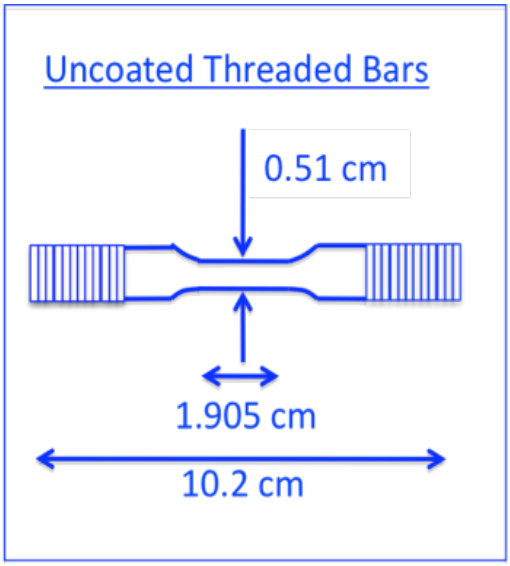

(a)

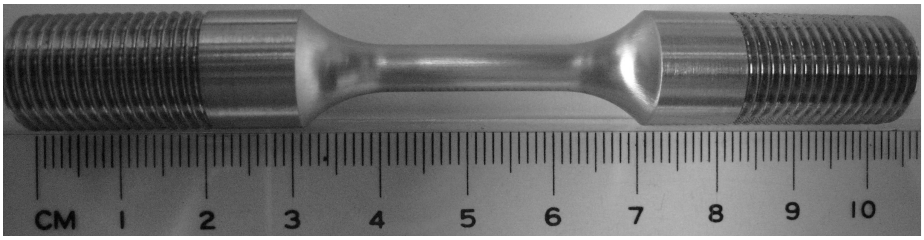

(b)

Figure 2.5 (a) Uncoated threaded specimen design for low cycle fatigue testing at 538°C. (b) Threaded single crystal specimen.

A triangular sinusoidal waveform was used at 0.5 Hz for the first 24 hours, followed by 9 Hz until failure. Hysteresis loops were recorded and digitally stored at predetermined loading cycle numbers. This allowed for the determination of elastic moduli and cyclic stress-strain behavior. Fractography and crack initiation analysis was performed on fractured samples using Phillips XL30 scanning electron microscopy (SEM) with an accelerating voltage of 25.0 kV.

2.3.2 High Cycle Fatigue Testing at Ultrasonic Frequencies

High cycle fatigue experiments were carried out using an ultrasonic fatigue test system with a cyclic frequency of approximately 20 kHz and at temperatures between 23-720^{o}C. The ultrasonic fatigue test instrumentation was developed by the Institute of Physics and Materials Science, BOKU, Vienna and the details of the system are reported elsewhere.[5] A portable ultrasonic fatigue unit, specifically designed for advanced imaging/diagnostic techniques, was built at the University of Michigan for *in-situ* X-ray studies of fatigue cracks in the beam line of the Advanced Photon Source (APS) at Argon National Laboratory (ANL).[6] Figure 2.6a schematically displays the apparatus, consisting of a transducer, a horn, connection bars and a specimen. Figure 2.6b shows the details of the fatigue loading train. The transducer converted an electrical signal from the power generator to a mechanical vibration; the horn was incorporated as an amplitude amplifier. For high temperature testing, the center of the gage section of the specimen was monitored with an infrared pyrometer. The lengths of all vibrating mechanical parts of the load train were adjusted to vibrate in resonance at approximately 20 kHz to obtain specific load amplitudes. The required mean stress was obtained by applying a mean load at the node position, as shown in Figure 2.6, where the vibration amplitude was zero.

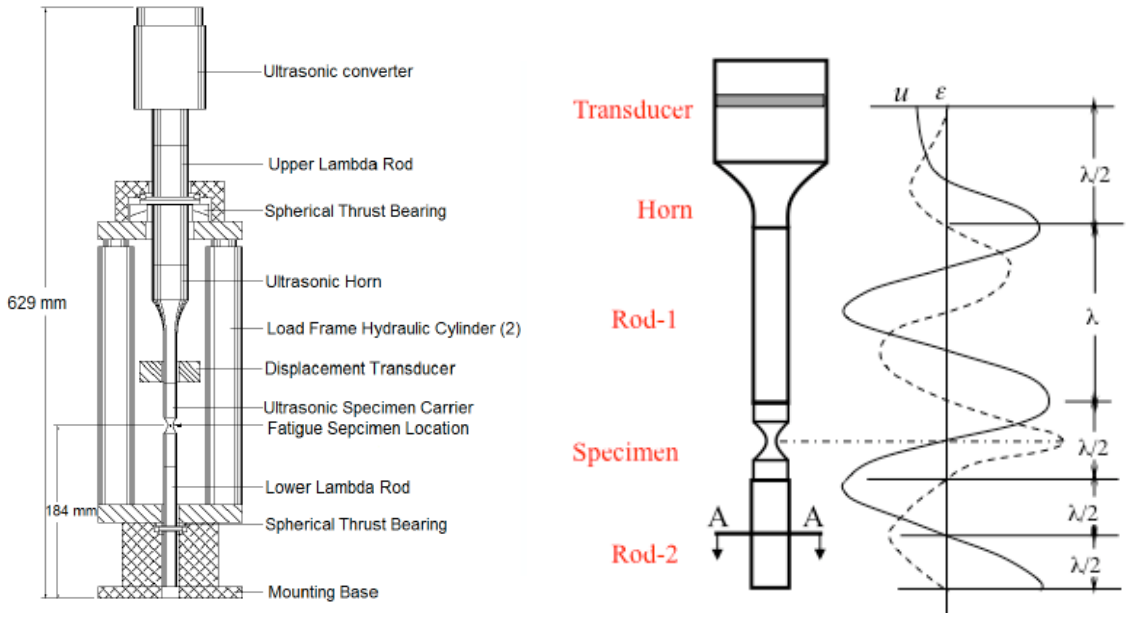

(a) (b)

Figure 2.6 (a) Overview of the details of a portable ultrasonic fatigue instrument[7] and (b) schematic of a fatigue loading train designed to achieve a maximum strain in the center of the specimen at 20 kHz. A-A is one of the node positions where mean load was applied, *u* is displacement, and *ε* is strain.

Fatigue tests were performed in a pulse-pause manner to minimize the temperature oscillation due to internal friction at high strain rate. A pulse length of 0.5s and pause 2.0s were found to give a good control of the temperature variation within ±3°C as suggested by Yi *et al*.[7]

In-situ x-ray radiation fatigue experiments of single crystal samples were performed at the Advanced Photon Source at Argonne National Laboratory. The portable fatigue apparatus (Figure 2.6a) was installed at Sector 32-ID to allow for samples to be dynamically imaged in transmission using coherent, high brilliance X-rays. It has been shown that the X-rays at this particular synchrotron source are capable of penetrating millimeters of superalloy material.[8] Therefore, in order to allow the passage of X-rays through the superalloy material, thin-sheets were fabricated from single-crystal bars and attached to a Ti-6Al-4V carrier bulk specimen with a 2 mm hole in the gage section (Figure 2.8).

Dog-bone shaped thin-sheet fatigue specimens were acquired by electrical discharge machining. Flat coupons, of dimensions shown in Figure 2.7, were ground and

polished to a thickness between 170-200 μm. The samples were loaded along the <001> crystal growth direction. An edge notch perpendicular to the tensile axis was produced in the gage section center by femtosecond laser machining (Figure 2.7b). The technique was utilized due to the limited amount of damage produced around the notch area within the superalloy material.[9]

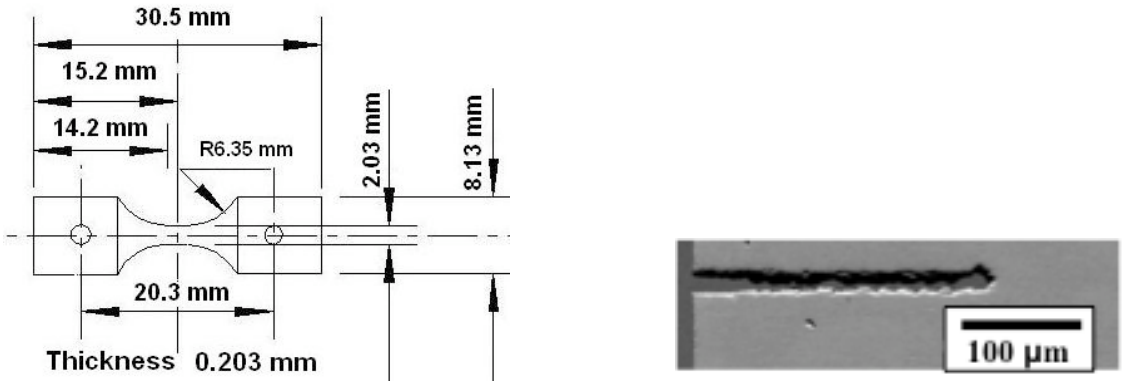

(a) (b)

Figure 2.7 Diagram of thin-sheet Ni-base superalloy microspecimen used in ultrasonic frequency fatigue experiments; (b) SEM image of a femto-second laser machined notch in the gage section.

A three-dimensional, linear static stress/displacement finite element analysis[6] determined the thin-sheet specimen geometry and carrier specimen design for resonance at 20 kHz. An illustration of the elastic stress distribution in the thin-sheet and carrier specimen is shown in Figure 2.8d, which determined the optimal testing conditions to (1) prevent fatigue failure of the carrier, which occurs with $N_f > 10^9$ cycles and (2) generate sufficient stresses at the notch tip in the microspecimen to initiate a fatigue crack.

Cyclic loads were applied to the microspecimen via the displacement of the carrier at the shoulder connections. Two hydraulic cylinders provided the loading force and guided the upper and lower platens for a hydraulic pressure necessary for static loads of 22 kN. Stress amplitudes were adjusted by varying the displacement amplitude of the carrier.

For high temperature testing, a micro-torch powered by an oxyhydrogen generator was attached to the portable unit. This generator operated by converting distilled water into oxygen/hydrogen fuel gas. The micro-flame produced extremely localized heating

for temperatures up to 900°C (Figure 2.9). It should be noted that the flame was not in direct contact with the specimen, but provided localized heating to the gage section.

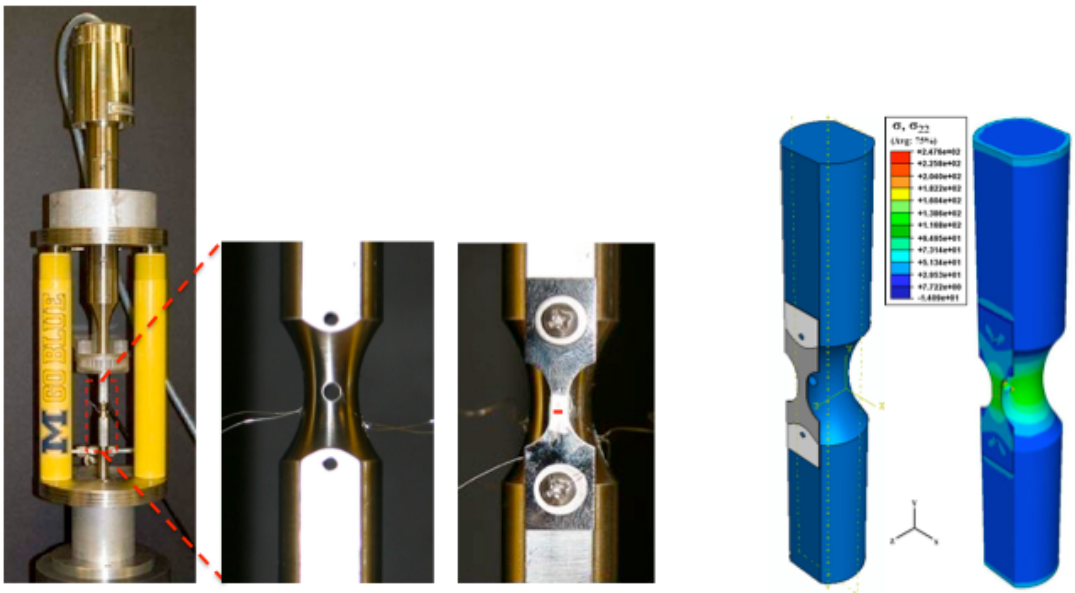

(a) (b) (c) (d)

Figure 2.8 Portable ultrasonic fatigue instrument; (b) details of the Ti-6Al-4V carrier specimen with a 2 mm diameter hole in the center of the gage section to allow the passage of the X-ray beam; (c) rigid attachment of the superalloy thin-sheet microspecimen to the carrier with a marked location of the laser notch; (d) FEA model and contour plot of the tensile stress σ_{22} due to the applied displacement.[6]

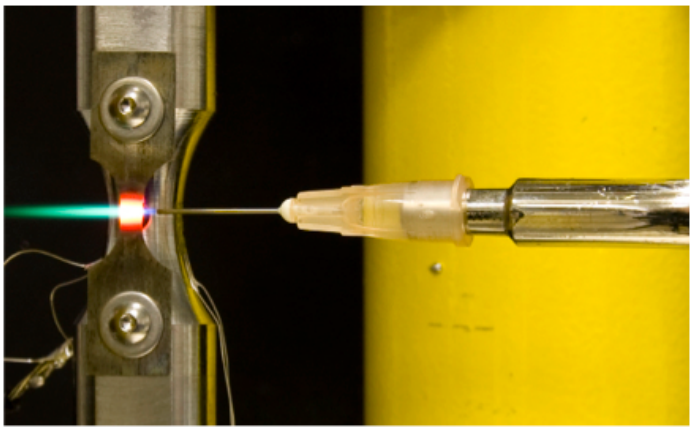

Figure 2.9 A micro-torch used for extremely localized heating at the gage section for temperatures up to 900°C.

Specimens were mounted in transmission geometry in line with a liquid nitrogen-cooled Si (111) double-crystal monochromator on a translation and rotation stage (Figure 2.10). This arrangement allowed for movement within the plane perpendicular to the X-

ray beam and rotation about the load axis. An undulator insertion device was utilized for X-ray radiation tuning at 23 keV and was collimated to approximately 1.8 mm x 1.5 mm. Attenuated X-rays induced fluorescence in a YAG: Ce scintillator crystal located 0.5 m behind the sample, which was imaged using a 16-bit, cooled charged-coupled device (CCD) with a 10x objective.[10] The effective spatial resolution was approximately 2 μm/pixel. The total image acquisition time consisted of a 50 ms integration time and 200 ms readout time. The output showed a high-quality, two-dimensional projection of the 3D structure image instantaneously, with only minor image processing [3,4] required to correct the slight Gaussian beam profile.

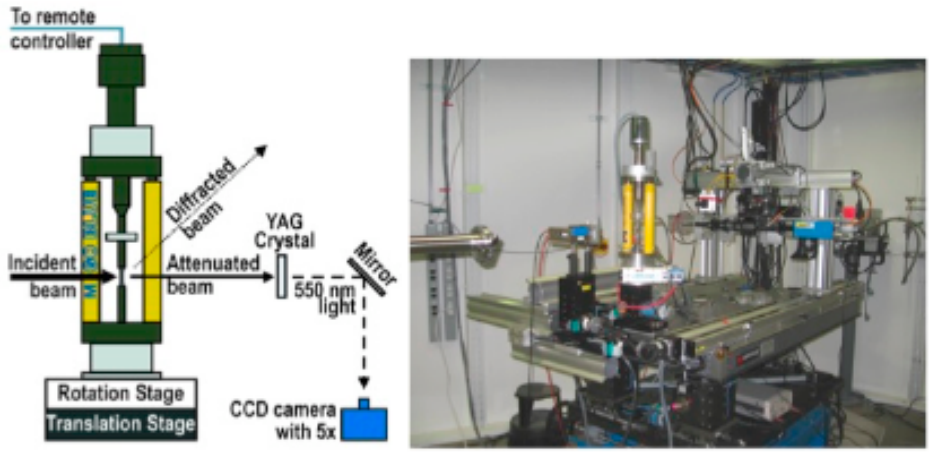

(a) (b)

Figure 2.10 Schematic of the portable fatigue apparatus, (b) which was installed at Sector 32-ID at the Advanced Photon Source at Argonne National Laboratory.[6]

---

[1] D.G. McCartney and J.D. Hunt: *Acta Metall.*, 1981, 29, pp. 1851-1863.

[2] R.E. Spear and G.R. Gardner: *Trans. AFS*, 1963, 71, pp. 209–15.

[3] The MathWorks Inc, Natick (MA).

[4] W.S. Rasband: ImageJ, US National Institutes of Health, Bethesda, MA, 1997–2007. Available from: http://rsb.info.nih.gov/ij/.

[5] H. Mayer: *Int. Mater*., 1999, 44, pp. 1.

[6] L. Liu, N.S Husseini, C.J. Torbet, D.P. Kumah, R. Clarke, T.M. Pollock, and J.W. Jones: *J. of Eng. Mat. Tech*., 2008, 130, pp. 021008-1-6.

[7] J.Z. Yi, C.J. Torbet, Q. Feng, T.M. J.W. Jones: *Mater. Sci. Eng,* 2007, 443, pp. 142-149.

[8] N. Husseini, D.P. Kumah, J.Z. Yi, C.J. Torbet, D.A. Arms, E.M. Dufresne, T.M. Pollock, J.W. Jones, and R. Clarke: *Acta Mater.*, 2008, 56, pp. 4715-4723.

[9] Q. Feng, Y.N. Picard, H. Liu, S.M. Yalisove, G. Mourou, and T.M. Pollock: *Scripta Mater.*, 2005, 54, pp. 511-516.

[10] E.M. Dufresne, D.A. Arms, N.R. Pereira, P. Ilinski, and R. Clarke: *SRI 2003*, 2004, 705, pp. 679-682.

Chapter 3

OPTIMIZATION OF THE LMC PROCESS

This chapter describes the LMC casting experiments employed to evaluate the capability of this process for refinement of structure in single crystal cylindrical bars containing cross sections relevant to aircraft engine airfoils. In order to assess the degree of structure refinement as a function of solidification rate, the dendrite arm spacings and γ/γ' precipitate sizes were quantified. The identification of an optimal withdrawal rate will be discussed in this chapter and the subsequent chapters of this dissertation will address the variability in structure and corresponding mechanical properties for the optimal rate. Material was also cast using a radiation (Bridgman) cooled process to establish a baseline for comparison of microstructure, defects and properties.

3.1 LMC Solidification Structure

René N5 was studied due to its frequent use in airfoils, as well as its similarity in composition to other commercially used single crystal alloys. For the purpose of identifying the optimal solidification velocity for the six-bar mold configuration employed (Figure 2.2), several critical features of microstructure were evaluated for each rate (8.5 mm/min, 12.7 mm/min, 21.2 mm/min), including (1) primary dendrite arm spacings (λ_1), (2) secondary dendrite arms spacings (λ_2), (3) microstructural uniformity along the length of the casting and (4) γ/γ' size and distribution. Table 3.1 lists the withdrawal rates utilized in the casting experiments. Either a seeded starter or pigtail grain selector was used to control single crystal grain growth and had no effect on the dendritic spacings.

Table 3.1 Bridgman and LMC withdrawal velocities used for growing single crystals.

Casting Run	Withdrawal Rate (mm/min)	Starter Type
1	3.4	Pigtail Grain Selector
2	8.5	Non-seeded starter
3	12.7	Non-seeded starter
4	21.2	Seeded starter

Images were collected from samples with longitudinal and transverse sections with respect to the withdrawal axis. Slices were taken at locations 1 cm from the top and bottom of each cast bar to measure the extent of variation in spacings along the length of the casting.

Dendrite morphologies are displayed as a function of withdrawal rate in Figure 3.1. The left two columns show the sections at the top and bottom locations transverse to the growth direction from the LMC and Bridgman processed bars.[1] It should be noted that tertiary arms were observed at all withdrawal rates. Differences in the dendritic scale along the length of the bar are apparent in the 8.5 mm/min micrographs, where significant refinement occurred in the top sections. Lateral growth and stray grain formation were observed at the top section of the 21.2 mm/min casting. Lateral growth is defined here as overgrowth of secondary dendrite arms, relative to primaries. The causes of lateral dendritic growth will be discussed in detail in the next section. Images in columns 3 and 4 are imaged in the plane parallel to the withdrawal direction, showing the secondary dendrite growth.

Castings produced by the LMC process at all withdrawal rates possessed a much smaller average λ_1 than Bridgman castings (Figure 3.2), indicating an overall enhancement in cooling rate. These spacings would be expected to decrease using rates higher than 3.4 mm/min due to the relatively high thermal gradients that are obtained with the LMC process.[2] The average λ_1 was refined with increasing withdrawal rate up

to 12.7 mm/min. Overall, the average primary dendrite arm spacings were reduced by approximately 50% in comparison to the Bridgman process.

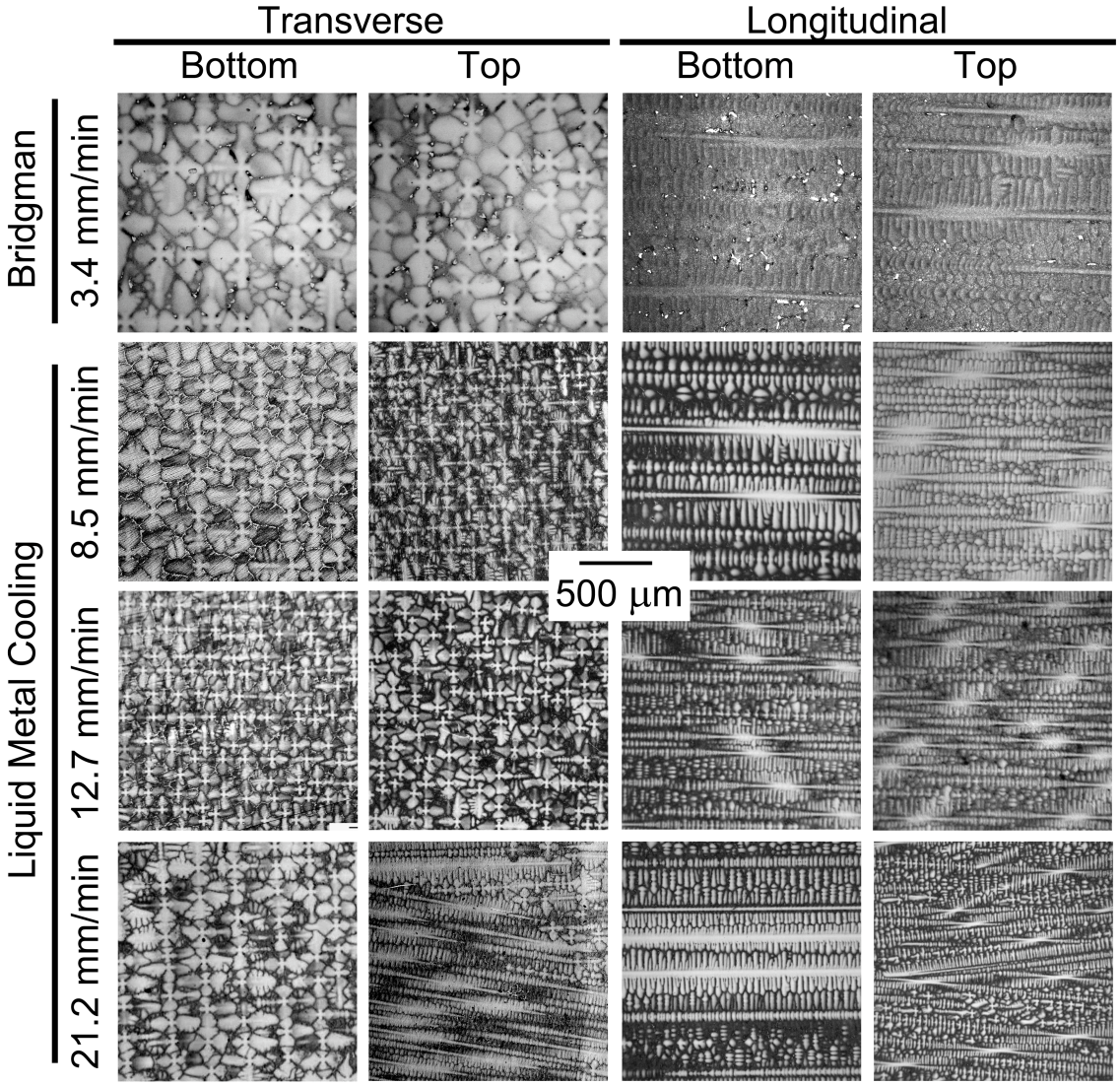

Figure 3.1 Optical images of dendrite morphology as a function of withdrawal rate for transverse and longitudinally sliced sections. Left two columns show [001] solidification direction perpendicular to the plane of the page. Right two columns show a plane parallel to the solidification direction as indicated.[1]

When comparing the variability in primary dendrite-arm spacings across the length of the bar, similar average spacings were measured in the top and bottom sections of the 3.4 and 12.7 mm/min castings, in contrast to all other withdrawal rates, (Figure 3.2). This indicates that a consistent solidification interface position with respect to the baffle location was maintained along the entire length of the bar. For the slowest LMC

withdrawal rate of 8.5 mm/min, a large variation in dendritic spacing across a transverse section was produced in comparison to all other rates. Even though the 21.2 mm/min rate produced lateral growth and stray grains on the top section, the smallest variation in spacing was produced along the length of the bar.

A substantial decrease in secondary dendrite arm spacing, λ_2, was observed in the LMC castings in comparison to the Bridgman bars. In general, top sections had slightly smaller average λ_2, indicating a slightly higher cooling rate in the later stages of solidification. The smallest overall λ_2 was observed at the fastest withdrawal rate of 21.2 mm/min. Approximately a 47% decrease in λ_2 was obtained by using LMC at 8.5 mm/min in comparison to Bridgman at 3.4 mm/min. However, only an overall decrease of 15% in λ_2 is produced by increasing the withdrawal rate from 8.5 mm/min to 21.2 mm/min using LMC, which is within the measurement error for these locations.

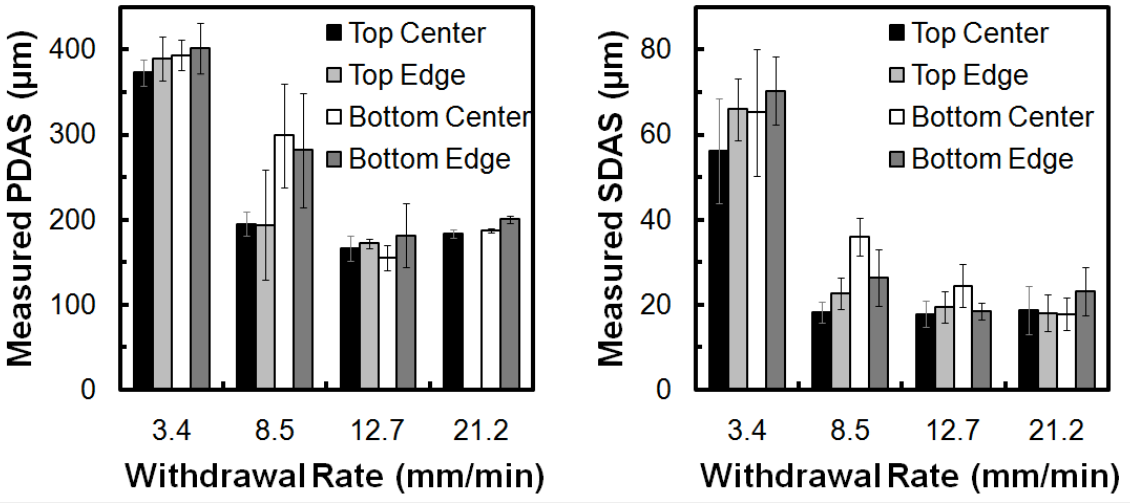

Figure 3.2 Average (a) primary and (b) secondary dendrite-arm spacings for edge and center locations measured from top and bottom sections of cylindrical cast bars processed via Bridgman (3.4 mm/min) and LMC (8.5, 12.7 and 21.2 mm/min) techniques at a range of withdrawal rates.[6] Note: 21.2 mm/min top section values could not be measured due to excessive growth of secondary arms.

3.2 Lateral Overgrowth of Secondaries

Figure 3.3 displays a transverse section with respect to the withdrawal direction at the top section of a 21.2 mm/min casting, revealing locations of severe overgrowth of

secondary dendrite arms. Nearly 50% of the surface area consists of lateral growth, whereas remaining areas show the dendrite morphology similar to the bottom section. Interestingly, secondary arm growth is inward in only one radial <100> direction.

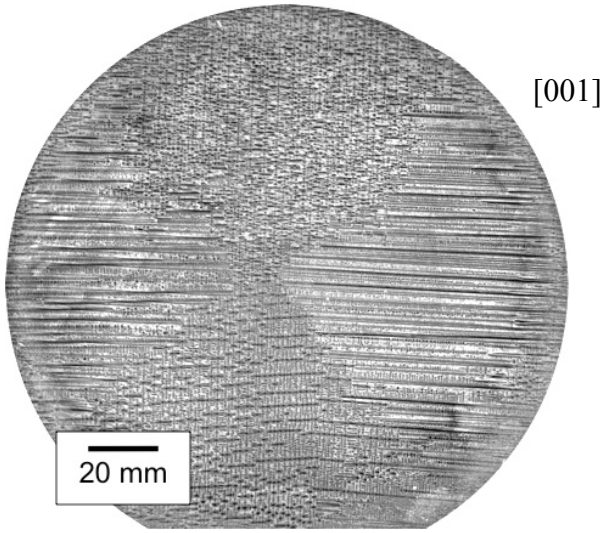

Figure 3.3 Stereomicrograph of the extensive secondary dendrite growth present in a top 1 cm section of a 21.2 mm/min withdrawn bar. Section is shown normal to the solidification direction.[6]

Lateral growth of secondary dendrite arms is of significant interest since it is an indication of unbalanced axial vs. lateral heat extraction.[3] With increased withdrawal rate, heat extraction becomes predominantly lateral through the mold, increasing the average cooling rate and causing the solid-liquid interface to become curved. For the experiments investigated, the lateral growth of dendrites initiated at the outer diameter of the casting and grew inward in one of the two possible directions ((100) or (010)). Due to the bar clustering, variation in thermal fields were produced causing the inner and outer diameters of the bars to experience asymmetrical solidification fronts.

3.2.1 Prediction of the Onset of Lateral Growth

The conditions under which lateral growth occurred during the solidification of alloys CMSX-486 and René N4 were studied experimentally and via solidification modeling using a ProCast™ model developed by Miller.[4] The presence of lateral growth was attributed to the inclination of the solidification front during casting due to non-axial thermal conditions during solidification. The solidification-front inclination

angle, θ, was calculated from the relative magnitudes of the thermal gradient parallel ($G_{\parallel}$) and perpendicular ($G_{\perp}$) to the withdrawal direction locally using Equation 3.1 as[4]

$$\theta = \tan^{-1}\left(\frac{G_{\perp}}{G_{\parallel}}\right) \qquad [3.1]$$

The analysis determined that the ratio of the thermal gradient magnitude is of critical importance to the formation of the final casting structure. Due to the observation of lateral growth during solidification at 21.2 mm/min, the predicted thermal gradients in the transverse and axial directions were analyzed for the range of withdrawal rates for René N5, Figure 3.4, using the identical ProCast™ model developed by Miller. It should be noted that the predicted lateral thermal gradient at the centerline of the bar is not present due to its symmetry.

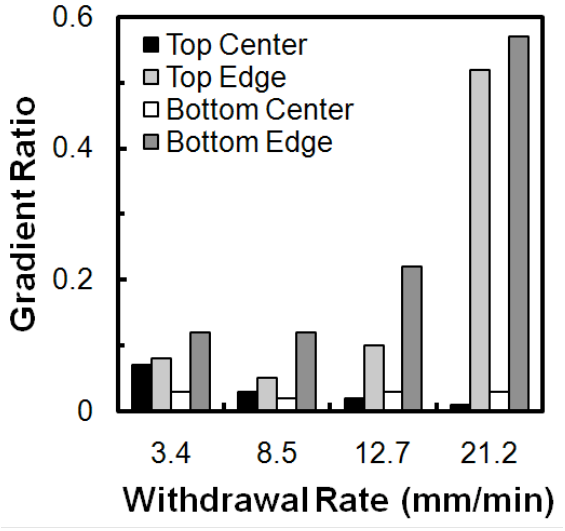

Figure 3.4 Predicted thermal-gradient ratio ($G_{\perp}/G_{\parallel}$) contours of cross-sections from simulations of René N5 bars cast via the Bridgman (3.4 mm/min) and LMC (8.5, 12.7 and 21.2 mm/min) processes for a range of withdrawal rates. Figure shown in Brundidge *et al.*[6]

Increasing the withdrawal rate resulted in an increase in the thermal-gradient ratio at the surface of the casting. As the withdrawal rate increased, the relative increase in the thermal gradient ratio increased, resulting in the increased interface curvature, Figure 3.3. According to the modeling data, it is expected that lateral growth will not occur at ratios less than 1. Since lateral growth did occur at a rate of 21.2 mm/min with a ratio ~0.6, it is suggested that the casting experiments did not maintain sufficient superheat during

solidification at this rate. Additionally, it is probable that the solidification model is slightly in error for this reason, and the actual ratio for this high velocity is greater than 1.

3.3 γ′ Size and Morphology

Figure 3.5 displays the γ/γ′ morphology within the interdendritic area for various solidification rates. Cuboidal γ′ precipitates were observed in all castings in the as-solidified condition. As with λ_1 and λ_2, the faster withdrawal rates employed with the LMC process resulted in a finer γ′ size compared to Bridgman.

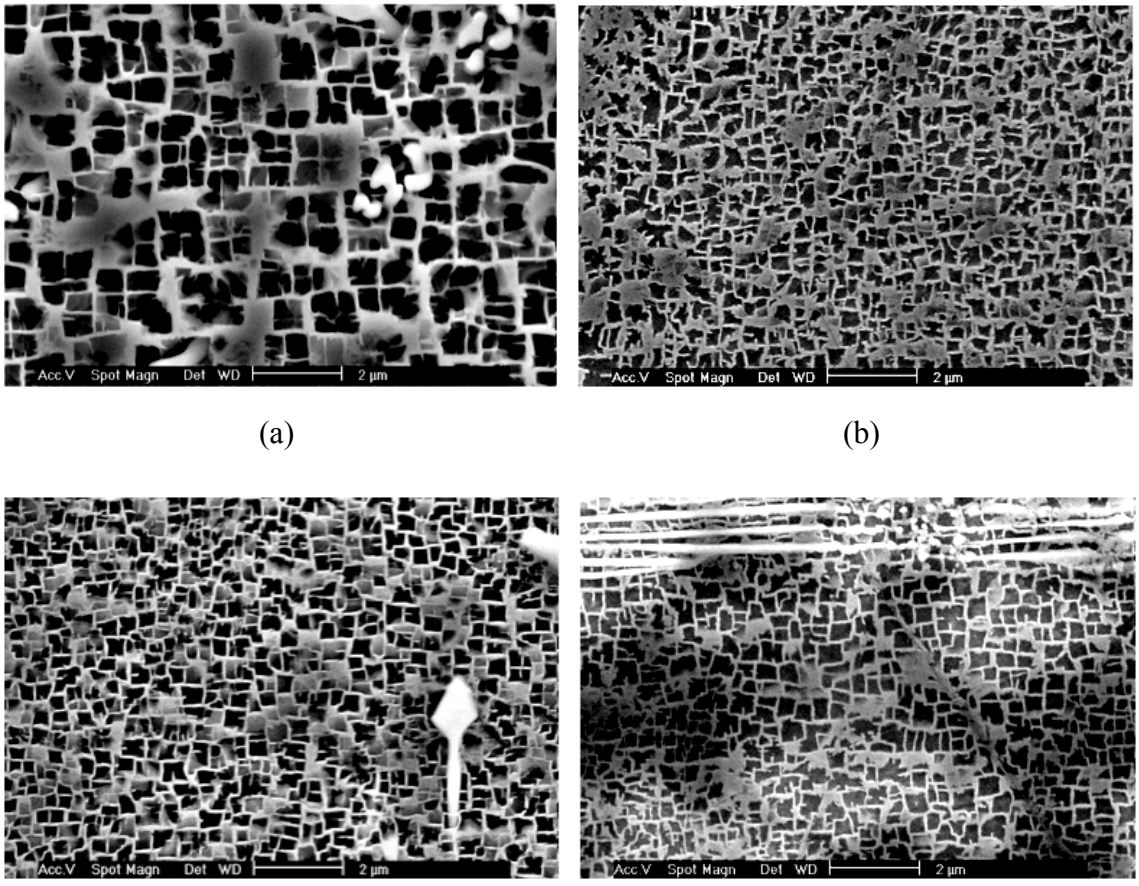

Figure 3.5 SEM images displaying the γ′ precipitates (dark) in a γ matrix (light) within the interdendritic area of as-cast samples from a (a) Bridgman solidification rate (3.4 mm/min), and LMC rates of (b) 8.5 mm/min, (c) 12.7 mm/min and (d) 21.2 mm/min.

Measurements of the γ′ edge length within the dendritic cores and interdendritic regions for each withdrawal rate are shown in Figure 3.6. Over 1,000 precipitates were measured from each region. The smallest average γ′ size within the dendritic core region

was produced within the slowest LMC withdrawal rate, however, this rate (8.5 mm/min) also provided the largest mismatch in dendritic/interdendritic precipitate size. Increases in the solidification rate decreased the difference in average γ′ size between the dendritic cores and interdendritic region.

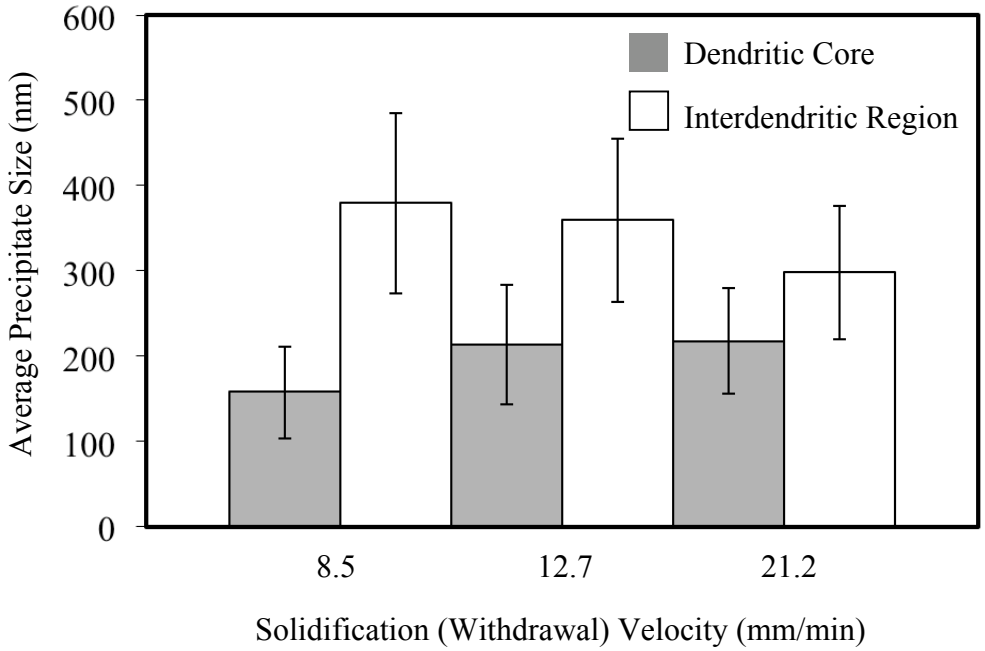

Figure 3.6 Average sizes of measured γ′ precipitates in LMC cast single crystal microstructures using various solidification rates. Sampling was performed directly within dendrite cores and interdendritic regions.

Figure 3.6 indicates a clear influence of microstructural location on the γ′ size for the 8.5 mm/min castings. Figure 3.7 shows the change in morphology moving from the dendrite core toward the interdendritic region. The γ′ in the dendrite core is smaller and blockier in shape than the interdendritic region, as exemplified with increasing distance from the dotted line. The change in γ′ size within the two regions occurs mainly because of the segregation behavior of the René N5 elements. The slow diffusing elements, including Re, partition preferentially to the dendrite core and inhibit the coarsening process in this region of the microstructure.

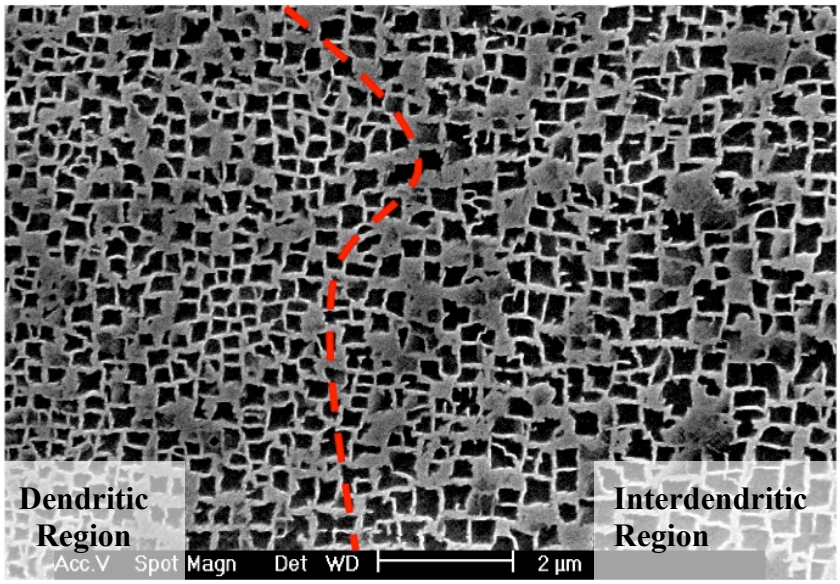

Figure 3.7 SEM image of a 8.5 mm/min solidified bar using the LMC process. The dotted line indicates the interface between the dendritic cores and interdendritic region.

Due to the segregation behavior and the formation of coarse γ′ precipitates within the as-cast material, it is necessary to perform solution heat treatments before a component is used in operation. Thus, the 12.7 and 21.2 mm/min rates would provide a more advantageous structure to reduce heat treatment time and expense.

Carbides, pores and γ–γ′ eutectic regions were observed in the interdendritic region at each solidification rate. Figure 3.8 displays SEM images of the interdendritic features observed in the 8.5 mm/min solidified casting. Ta rich carbides were distributed heterogeneously throughout the microstructure, as observed in previous studies of René N5.[5] Both blocky and script carbides were observed (Figure 3.8b).

Similar solidification features were observed at all other rates, see Figure 3.9-3.11. A large pore is shown in the micrograph of a Bridgman casting (Figure 3.11a), which was significantly larger than any pore observed within the LMC processed bars. However, very few pores were observed on individual 2 cm^2 cross sections of the bars, which indicated a need for measurements on multiple sections to more accurately access porosity distributions for each variant. These measurements will be detailed in Chapter 4.

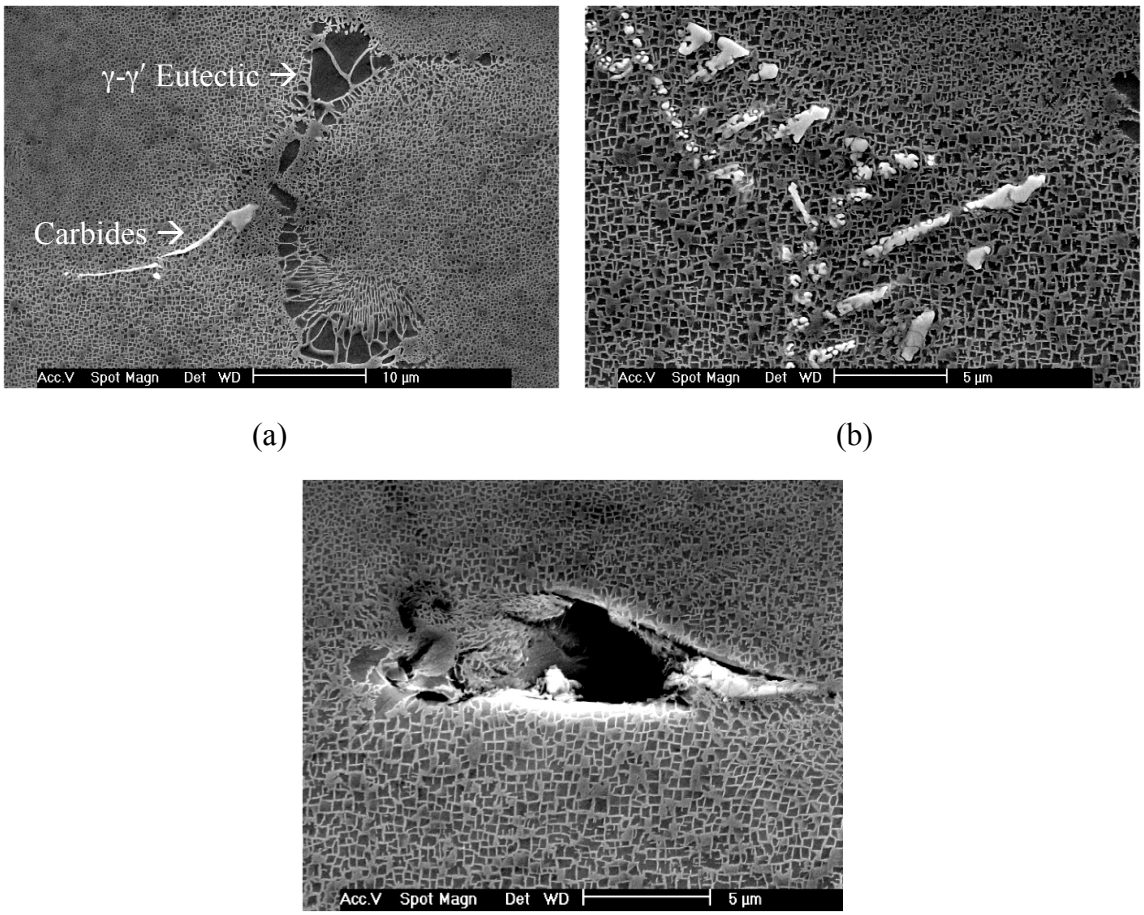

Figure 3.8 SEM images displaying (a) a blocky carbide adjacent to a γ–γ′ eutectic region, (b) script carbide, and (c) casting pore within a 8.5 mm/min solidified bar.

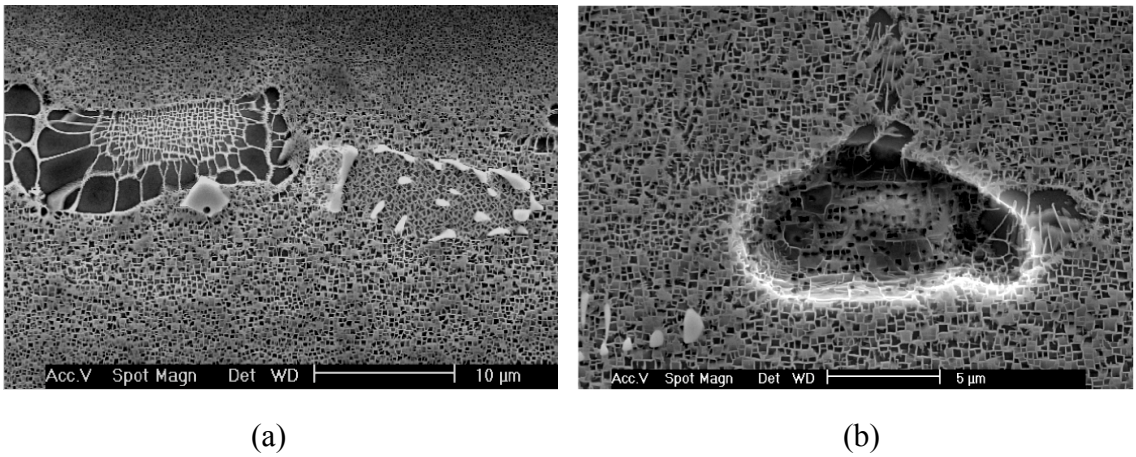

Figure 3.9 SEM-secondary electron images of the interdendritic features within a 12.7 mm/min solidified bar. (a) A eutectic region adjacent to blocky carbides is shown. (b) A pore within the interdendritic region is displayed.

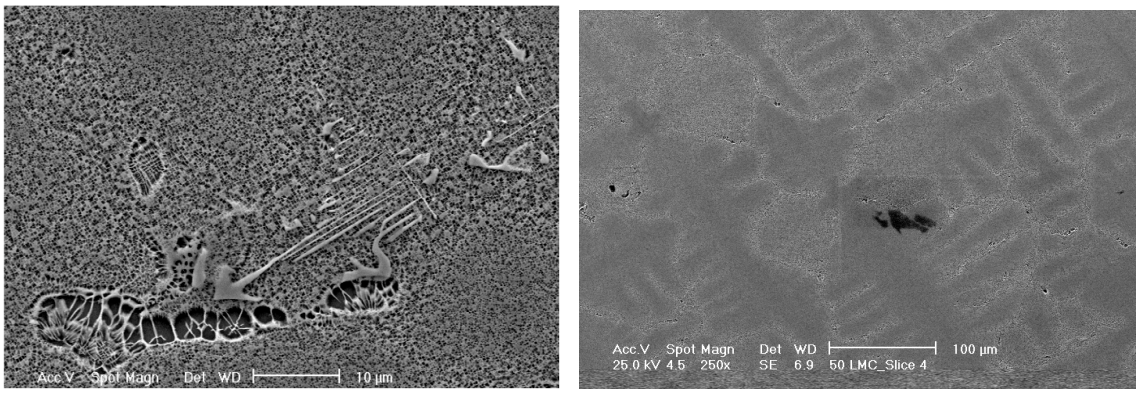

(a) (b)

Figure 3.10 SEM-secondary electron of the interdendritic solidification features within a 21.2 mm/min solidified bar.

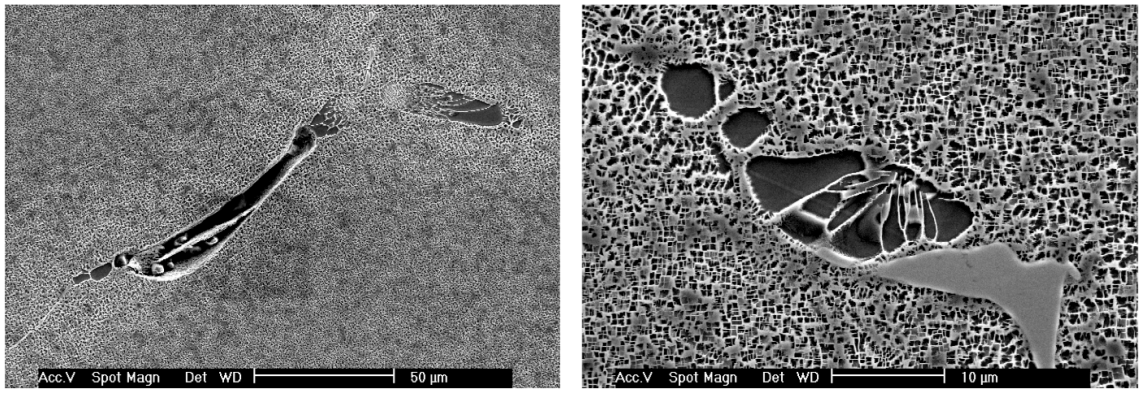

Figure 3.11 (a) Large pore within the interdendritic area of a Bridgman cast (3.4 mm/min) section. (b) $\gamma-\gamma'$ eutectic near a large blocky carbide.

3.4 Determination of Optimal Solidification Conditions

For the cylindrical bar geometry of this study, an optimal solidification rate was selected based on the refinement degree of structure, homogeneity in dendritic structure along the length of the casting, γ' size and morphology, and defect occurrence. The following sections address the influence of solidification conditions on resulting microstructure and the limit to extent of refinement that can be obtained with the LMC process.

3.4.1 The Solid/Liquid Interface During Solidification

The experiments conducted in this study have demonstrated that the LMC process is highly beneficial for producing refined microstructures and reducing the segregation of

alloy constituents. For the 1.6 cm diameter bars, an intermediate solidification velocity produced the most advantageous refinement in dendritic structure throughout the length of the entire bar. Variation in dendrite spacing along the withdrawal axis indicates an imbalance of heat extraction and an undesirable position and shape of the solid/liquid interface during solidification. Changes in λ_1 along the length of the bar occurred due to movement of the location of the solid/liquid interface relative to the baffle zone in the LMC setup. The ProCast solidification simulation in Brundidge and Miller[6] predicts the steady-state position of the solid/liquid interface relative to the transition region of the furnace, shown in Figure 3.12. A reduction of the predicted melting-range height and the height between the liquidus and solidus temperatures was observed with utilization of the LMC process, due to the increased thermal gradient. For the LMC process, an increase in withdrawal rate lowered the position of the solid-liquid interface relative to the floating baffle. In turn, the curvature of the solidification front increased as well, due to the lateral heat extraction from the coolant.

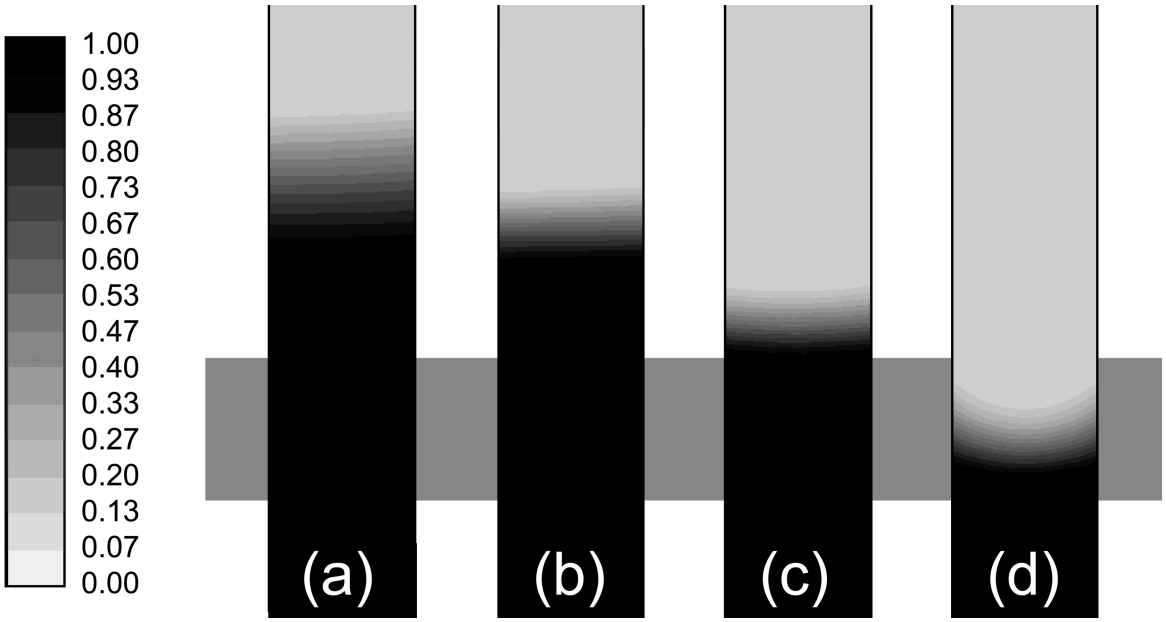

Figure 3.12 Fraction-solid contour plots from simulations of bars cast via (a) Bridgman processing at 3.4 mm/min and LMC at (b) 8.5 mm/min, (c) 12.7 mm/min and (d) 21.2 mm/min). Figure shown in Brundidge *et al.*[6]

Elliott *et al.*[5] investigated the influence of the relative solid/liquid interface curvature on the resulting microstructure of directionally solidified GTD-444 and observed similar solid/liquid interface curvature at high withdrawal rates. The upward

movement of the solid/liquid interface using LMC casting at the slowest withdrawal rate suggested that the cooling efficiency exceeded the heating capability. Also, at the fastest rate, the cooling capacity lagged the heating capability, and the conditions were consequently unable to maintain a stable interface location near the baffle. The effect of solid/liquid interface movement provides a reasonable explanation for the breakdown of the solidification front exhibited in the 21.2 mm/min-solidified castings.

The changes in λ_1 produced within the 8.5 mm/min experiment along the length of the casting suggest an initially suboptimal position of the solid/liquid interface above the baffle toward the mold heater. In the case of the 21.2 mm/min rate, the large shift in the solid/liquid interface from the baffle/coolant line combined with a curvature at the crystallization front caused severe lateral growth of secondary arms within the outer-edge regions of castings, Figure 3.3. At this solidification velocity, the liquid tin does not have sufficient cooling capacity to sustain this high withdrawal rate. Excessive concavity combined with upward solidification has been known to create defects that can degrade the mechanical properties of cast blades.[7] Even though the fastest rate investigated (21.2 mm/min) provided smaller λ_2 values, the formation of high angle grain boundaries and excessive transverse dendrite growth was taken into account when selecting the optimal withdrawal rate.

3.4.2 Breakdown of Single Crystal Microstructure

One of the major issues encountered during solidification of single crystal components is the formation of stray grains.[8] These grains develop due to the nucleation and growth of an undesired crystal in the body of a blade, or at a specific location where significant undercooling develops, such as the platform ends. The stray grains would subsequently act as a favorable location for crack initiation and in-service failure. However, despite the presence of grain boundaries in the 21.2 mm/min cast material, the effect of transverse growth on the mechanical properties has not been fully addressed in the literature.

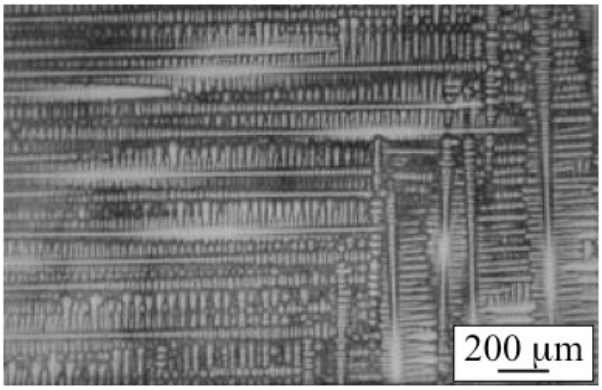

Figure 3.13 Optical micrograph of the surface parallel to the withdrawal direction for a 21.2 mm/min solidified bar.

3.4.3 Limit to LMC Structure Refinement

To produce single crystals with spatially uniform properties, the most desirable withdrawal rate is one that generates a consistency in dendritic structure along the length of the bar. Thus for the conditions investigated, the best possible cooling rate with the liquid-metal cooling process resulted from a 12.7 mm/min-withdrawal rate. Modeling suggests that a fairly flat solid/liquid interface at the floating baffle is maintained, with balanced heat input and extraction, and no high angle grain defects. This rate produced a uniform, fine-scale dendrite arm spacing with λ_1 and λ_2, of 160 μm and 22 μm, respectively, along the length of the bar by maintaining a planar solid/liquid interface at the baffle line during the entire casting process.

At the optimum withdrawal rate, the variability in structure within a bar was also a minimum. The smallest λ_2 was produced using a velocity 21.2 mm/min, which produced up to a 60% refinement in comparison to Bridgman at 3.4 mm/min. However, only a 2 μm decrease in λ_2 is obtained by increasing the velocity from 12.7 mm/min to 21.2 mm/min, which may not significantly influence the mechanical properties.

The limit for the LMC process, for this particular alloy and mold configuration, occurs near a withdrawal rate of 21.2 mm/min, as demonstrated by the lateral overgrowth of secondary dendrite arms at the top sections of the bar, as shown in Figure 3.1. In addition to dendrite arm spacings, as-cast $\gamma-\gamma'$ homogeneity was also a determining factor for selecting an optimal withdrawal rate, since precipitate size and distribution through out the macrostructure determines the final heat treatment times and temperatures. The

size, distribution and shape of as-cast γ′ precipitates vary dramatically within Bridgman and LMC castings, Figure 3.5. As expected, the γ′ is smaller in the dendritic core region than in the interdendritic region for all cases. Increases in solidification rate decrease the overall average γ′ size, even though a limit in λ_1 refinement was ascertained at 12.7 mm/min, which indicates that the precipitates are controlled primarily by the cooling rate. At faster LMC solidification rates, the decrease in γ′ size difference between dendrite cores and interdendritic regions may indicate a reduction in the degree of elemental segregation during casting.[9] Since the formation of γ–γ′ eutectics is closely related to the solute segregation during solidification, higher solidification rates can effectively obtain more homogenous structures. Nonetheless, the 12.7 mm/min rate produced similar sized γ′ precipitates within both regions. Thus, this rate was selected for further studies.

3.5 Summary

The benefits of a LMC casting process have been assessed by direct comparison to the Bridgman casting method for solidification of 1.6 cm diameter René N5 bars. The use of liquid-tin as the cooling medium combined with a floating, ceramic baffle, higher thermal gradients and faster cooling rates permits solidification of single-crystal nickel-base superalloys with substantially refined microstructures.

For the LMC withdrawal rates between 8.5-21.2 mm/min, the maximum structure refinement was produced at an intermediate rate of 12.7 mm/min, producing λ_1 and λ_2 values of 160 μm and 22 μm, respectively for the 1.6 cm diameter bars. An intermediate rate maintains a favorable interface location and shape, yielding a 50% and 60% refinement in λ_1 and λ_2, respectively, in comparison to Bridgman (radiation) processing. Additionally, this rate produced similar sizes of γ′ precipitates in the dendritic cores and interdendritic regions, thus making it a suitable candidate for shorter heat treatment times.

Lateral growth and breakdown of single crystal microstructure was completely avoided except at the fastest solidification rate, 21.2 mm/min. Thermal gradient ratios of the axial and lateral thermal gradients provided a sufficient means to predict the conditions of lateral growth.

The 12.7 mm/min solidified material was selected for statistical analysis of the heterogeneity in microstructure, and the results are presented in Chapter 4. Additionally, a René N5 modified alloy with an increased weight pct of Ta was solidified at the 12.7 mm/min withdrawal rate to analyze the effect of precipitate strengthening and the influence of refinement with increased refractory composition using the LMC process. The mechanical properties for the 12.7 mm/min solidified alloys will be detailed in Chapter 5 and 6 for comparison to Bridgman cast microstructure as a baseline.

---

[1] C.L. Brundidge, D. Van Drasek, B. Wang, and T.M. Pollock: in *Int. Symp. On Liquid Metal Processing and Casting*, P.D. Lee, A. Mitchell and R. Williamson, eds., (The Minerals, Metals & Materials Society, 2009) pp. 107-117.

[2] A.F. Giamei and J.G. Tschinkel: *Metall. Trans. A*, 1976, 7, pp. 1428-1434.

[3] J.D. Miller: *PhD Thesis*, 2011, University of Michigan, Ann Arbor, MI.

[4] J.D. Miller and T.M. Pollock: in *Int. Symp. On Liquid Metal Processing and Casting*, P.D. Lee, A. Mitchell and R. Williamson, eds., (The Minerals, Metals & Materials Society, 2009), pp. 119-126.

[5] A.J. Elliott, *Ph.D. Thesis*, 2005, University of Michigan, Ann Arbor.

[6] C.L. Brundidge, J.D. Miller, and T.M. Pollock: *Metall. Mater. Trans. A*, 2011, in press.

[7] W. Wang, P.D. Lee, and M. McLean: *Acta Mater*., 2003, 51, pp. 2971-2987.

[8] A. De Bussac, Ch.-A. Gandin: *Mater. Sci. Eng.*, 1997, 237, pp. 35

[9] B.C. Wilson, J.A. Hickman, and G.E. Fuchs: *JOM*, 2003, 55, pp. 35-40.

Chapter 4

MODELING THE HETEROGENEITY IN DENDRITIC STRUCTURE

Since the convective cooling within the LMC process had a profound effect on refinement of the dendritic structure, it is of particular interest to examine the influence of solidification processing conditions on the heterogeneity in microstructure, radially and axially within the solidified bars. Chapter 4 describes the statistical analyses used to characterize the variability in dendritic spacings and porosity within René N5 alloys solidified with the LMC and Bridgman processes. Three aspects of the cast structure and associated defects will be examined in detail in the following order: (1) the influence of higher gradient casting on the dendritic structure and packing, (2) new statistical approaches to quantify porosity content, and (3) the correlation between pore structure and dendritic structure.

A statistical method using Voronoi polygons (outlined in Chapter 2) has been employed to quantify the heterogeneity in primary dendritic structure in terms of spacings and nearest-neighbors. Distributions of primary dendrite arm spacings analyzed in terms of Voronoi-dendrite cell size will be presented for 8.5 mm/min, 12.7 mm/min and 21.2 mm/min withdrawal rates from using the LMC process and compared to Bridgman casting at 3.4 mm/min. Furthermore, the influence of Ta on the heterogeneity in dendritic scale was examined for both solidification processes. Pore sizes were measured and correlated to the Voronoi-dendrite cell size in order to obtain a relationship between primary dendrite arm spacings and potential fatigue initiation site sizes.

This chapter will also outline the statistics of extremes value (SEV) method, which is typically used to predict the maximum defect size in a component. Stereological formulae, for both 2-D to 3-D sections, will be described as a means for estimating the maximum pore size in a casting and characterizing the pore size distribution within each variant. Additionally, an estimation of the maximum pore size as a function of fluid flow

parameters for René N5 using the Blake-Kozeny expression will be discussed. The ability to predict maximum defect sizes that limit the fatigue life is a key element in developing a processing-structure-fatigue model, which has motivated this study.

4.1 Spatial Distribution in Dendritic Spacings

Key microstructural features in engineering materials are typically described by their average values when predicting mechanical behavior. For instance, solidification models developed by Hunt and Kurz[1] and Fisher,[2]the Hall-Petch equation, the 'rule of mixtures', and creep models, such as Coble, all describe microstructural aspects by means of average λ_1, average grain size, average inter-particle spacing, and volume fraction, respectively. In the case of directionally solidified material, the dendritic structure is generally characterized by the average primary and secondary dendrite arm spacings, Equations 1.7 and 1.8. Unfortunately, information relating to the spatial distribution of dendrite spacings about a mean quantity is neglected even though weak links may reside in the vicinity of the structure that contains a significant disparity in the extreme values. Therefore, it is of considerable interest to characterize the distribution of dendritic spacings along with the associated interdendritic defects. Prior investigations have demonstrated that the uniformity of spatial distribution of microstructural features plays a key role in controlling the yield strength, ductility, fatigue and fracture of various metallic alloys.[3-5] However, when aiming to link microstructure heterogeneity with mechanical properties, one needs to establish unambiguous definitions of fundamental terms to quantify the spatial distribution of microstructure features, such as 'homogeneous', 'random', or 'clustered'.

Figure 4.1a shows a metallographically prepared, transverse section of an as-cast (12.7 mm/min) sample and the corresponding Voronoi-dendrite map. It should be noted that the edge cells within the Voronoi maps are not used for calculation, since an accurate cell cannot be constructed without the outer lying coordinates of nearby dendrite cores. Each Voronoi-dendrite cell is color coded (see key in Figure 4.1) to represent the number of nearest neighbors. In Figure 4.1b, the range of nearest neighbors is between 4 and 8. Figure 4.1c shows the range of primary dendrite arm spacings for this section, where 20% of the cells were less than or equal to 140 μm in diameter. Figure 4.1d displays the results

for the Voronoi cell diameters shown on a probability plot, as well as a cumulative density function (CDF) for the data (Figure 4.1e). The equation for the three-parameter Weibull CDF is given by

$$F(T) = 1 - e^{-\left(\frac{T-\gamma}{\eta}\right)^{\beta}} \qquad [4.1]$$

where η, β and γ are the scale, shape and location parameters, respectively.

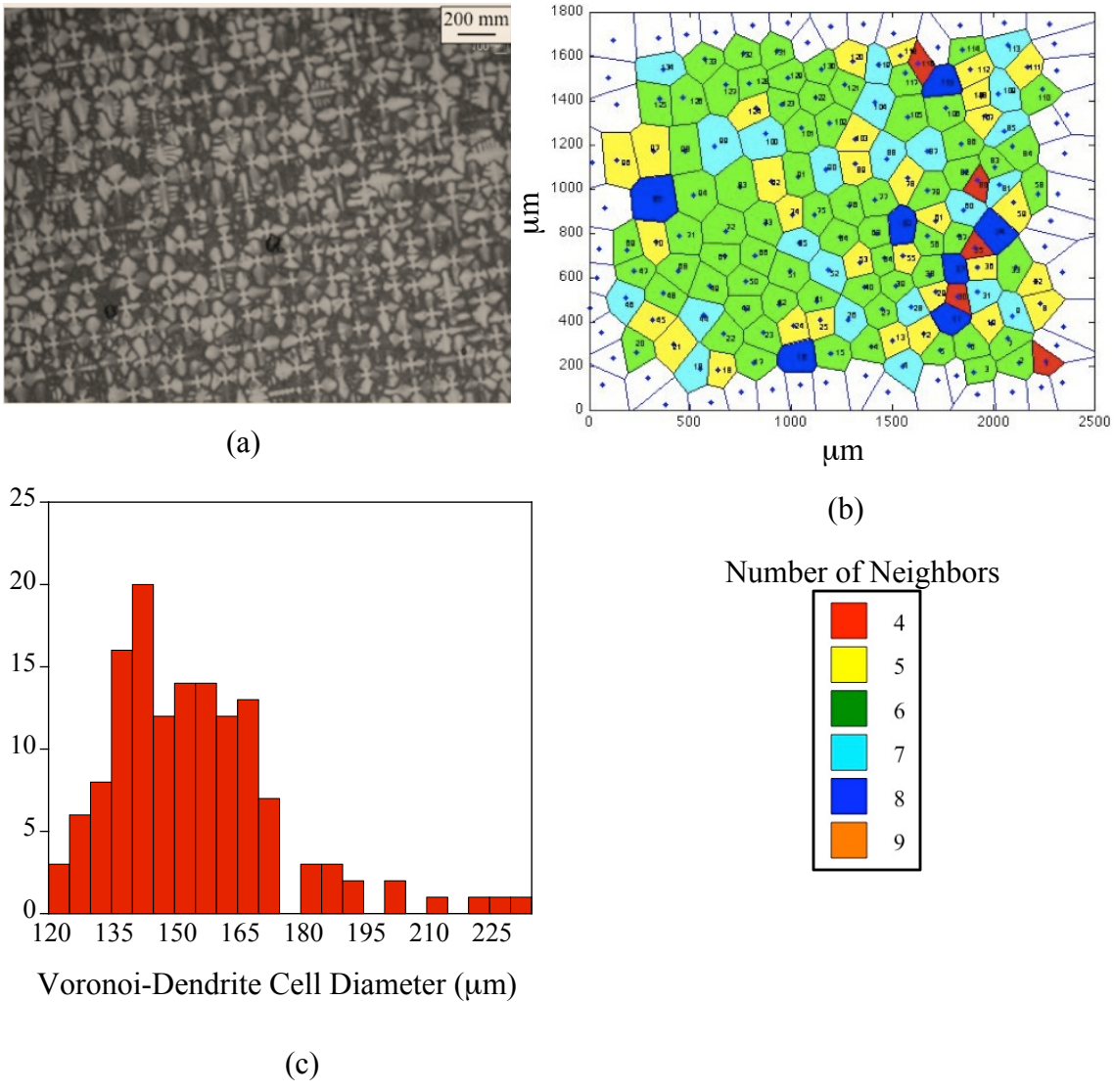

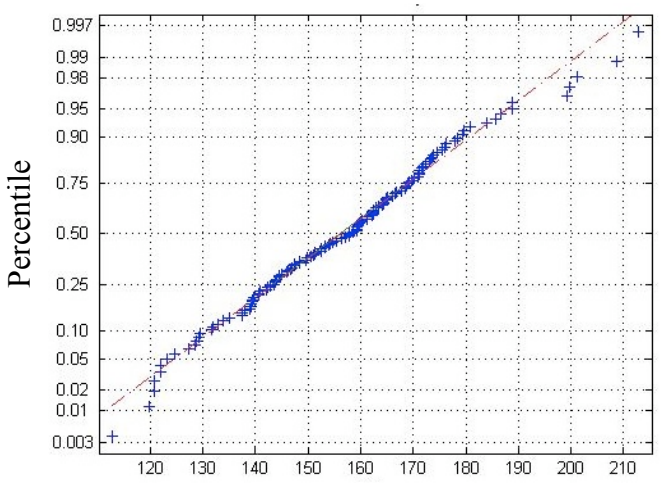

(d)

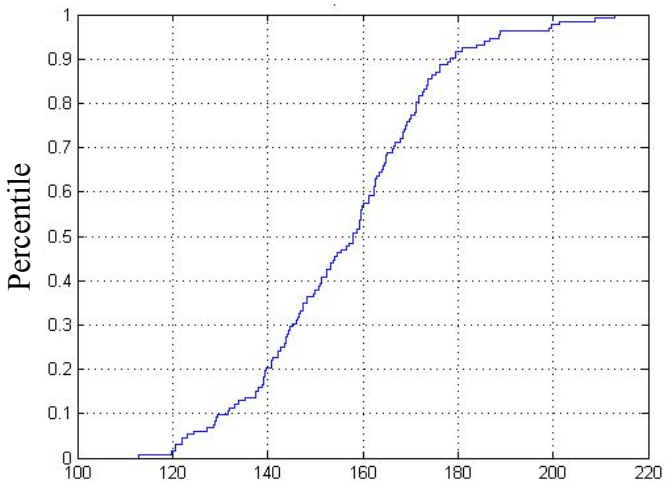

(e)

Figure 4.1 (a) Metallographically prepared transverse as-cast section with respect to the withdrawal direction, (b) corresponding Voronoi-dendrite map for a 12.7 mm/min solidified alloy illustrating the number of nearest dendrite neighbors by color. (c) A distribution of the Voronoi-cell sizes and (d) a probability plot details the spatial distribution in dendritic spacings for the given area in the optical image. (e) A CDF plot details the percentile of cells for the Voronoi-dendrite map.

Typically, Weibull plots are used to identify the probability of failure for a given stress level. Therefore it is of importance to investigate the character of the distribution of dendrite spacings for a given solidification condition in order to identify the factors that influence the fatigue life. The probability plot provided an indication as to whether

the primary dendrite spacings were normally distributed. Data outside of the percentile range of 0.05 and 0.95 were not normally distributed (Figure 4.1d).

Voronoi-dendrite maps in Figure 4.2 display the number of nearest neighbor dendrite cores for each withdrawal rate used in the casting experiments detailed in Chapter 3. Only a portion of the sample cross section is shown here, with the sampling taken from a bottom section of a cast bar at each rate. The enlarged number shown within each polygon indicates the corresponding number of nearest neighbors. Also, the color scheme key shown in Figure 4.1 is applicable here. It is obvious from the figure that there exists a range of neighbors for each rate.

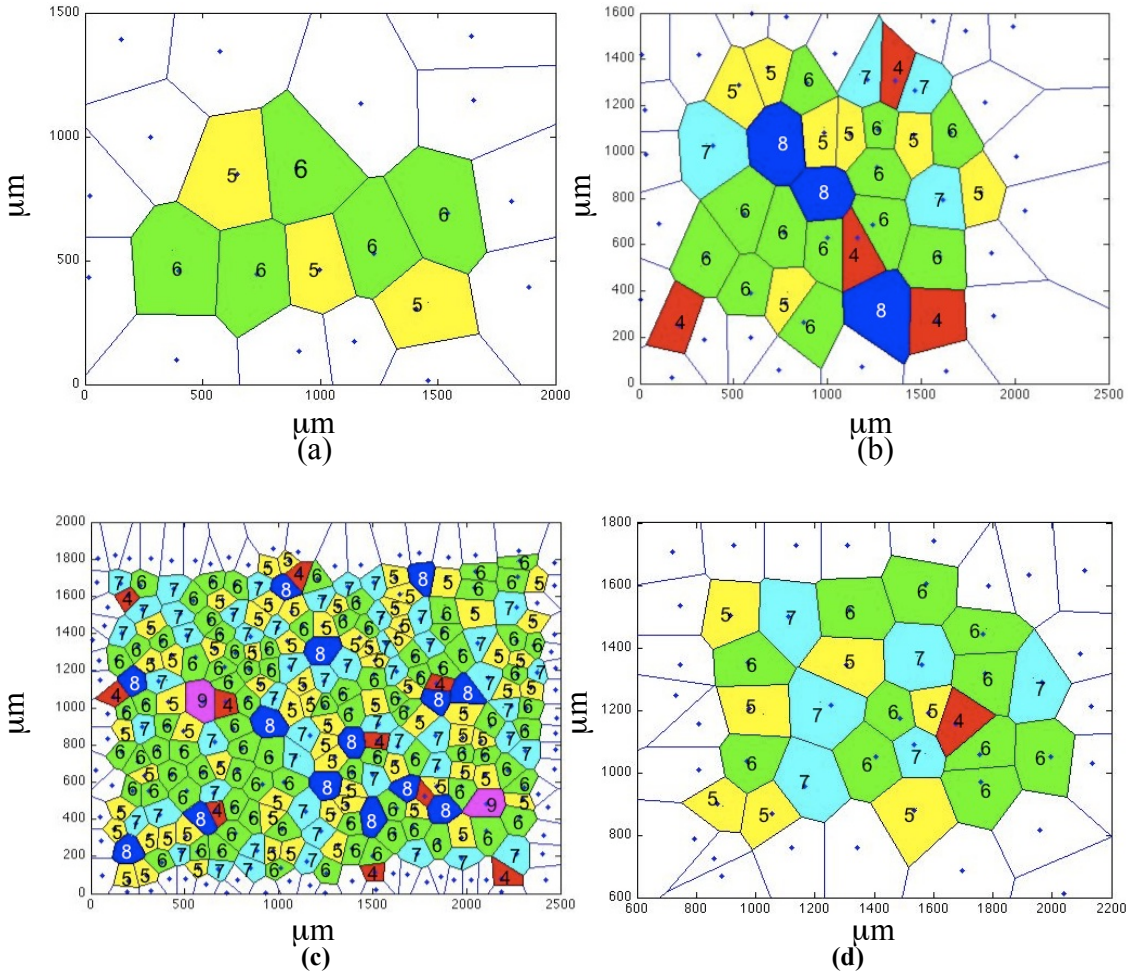

Figure 4.2 Voronoi (dendrite) maps for selected withdrawal rates solidified with (a) Bridgman at 3.4 mm/min and LMC casting at (b) 8.4 mm/min, (c) 12.7 mm/min, (d) 21.2 mm/min for bottom sections. Numbers of nearest neighbors are indicated in each cell.

Figure 4.3 shows the variation in the relative frequency distribution of the number of nearest neighbors as a function of withdrawal rate. In order to obtain comparable sampling at each rate, at least 700 dendrite cores were measured to generate this plot. It is evident that the six-sided polygons are dominant for each rate. Approximately 53 pct of the cells were hexagonal within the Bridgman solidified material, whereas the LMC solidified material constituted only 40-47 pct. Interestingly, these measurements were lower than what has been observed in studies on dendritic structures (~60 pct).[6] A maximum of 7 neighbors was observed in the radiation cooled samples, in contrast to the LMC process, where a maximum of 9 cells was exhibited. Here, the influence of the higher gradient LMC process is reflected in the higher order numbers of nearest neighbors. Here, "ordering" refers to the periodic arrangement of dendrite cores, specifically for square, hexagonal or random packing. Random dendritic packing would reflect the most disordered dendritic arrangement.

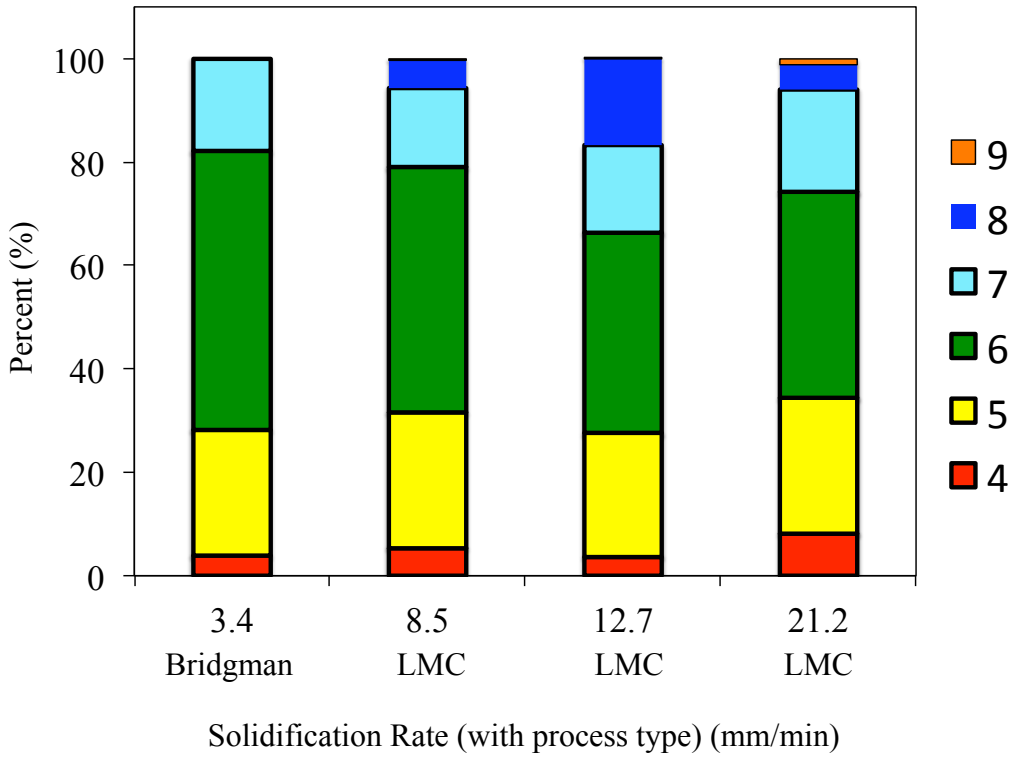

Figure 4.3 Relative frequency distribution of the number of nearest neighbors for various solidification rates including: 3.4 mm/min withdrawal Bridgman, and 8.5, 12.7 and 21.2 mm/min solidified samples using the LMC process.

It is highly desirable to obtain finely spaced and ordered microstructures to produce the most homogeneous microstructures, leading to uniform fatigue properties. Nearest-neighbor interactions from lateral growth of secondaries, creating long tertiary arms, may cause a disruption in the fluid flow during solidification. It is clear that the solid/liquid interface curvature plays a role in the primary dendrite spacing development, and also may play a significant role in the ordering of dendritic arrays as well.[7]

The Voronoi-dendrite cell size distribution for images collected for each withdrawal rate at a bottom section is shown in Figure 4.4. At least 20 micrographs per rate were used to generate this plot. The largest range in spacings was produced at a rate of 8.5 mm/min for the LMC process. All other rates produced a $\Delta\lambda_1$ between 90-95 μm for the given cross-sectional area. The minimum and maximum spacing values were observed in the 12.7 mm/min and 3.4 mm/min withdrawal rates, respectively. Interestingly, the distributions acquired form the 8.5 mm/min and 12.7 mm/min LMC withdrawal rates do not overlap.

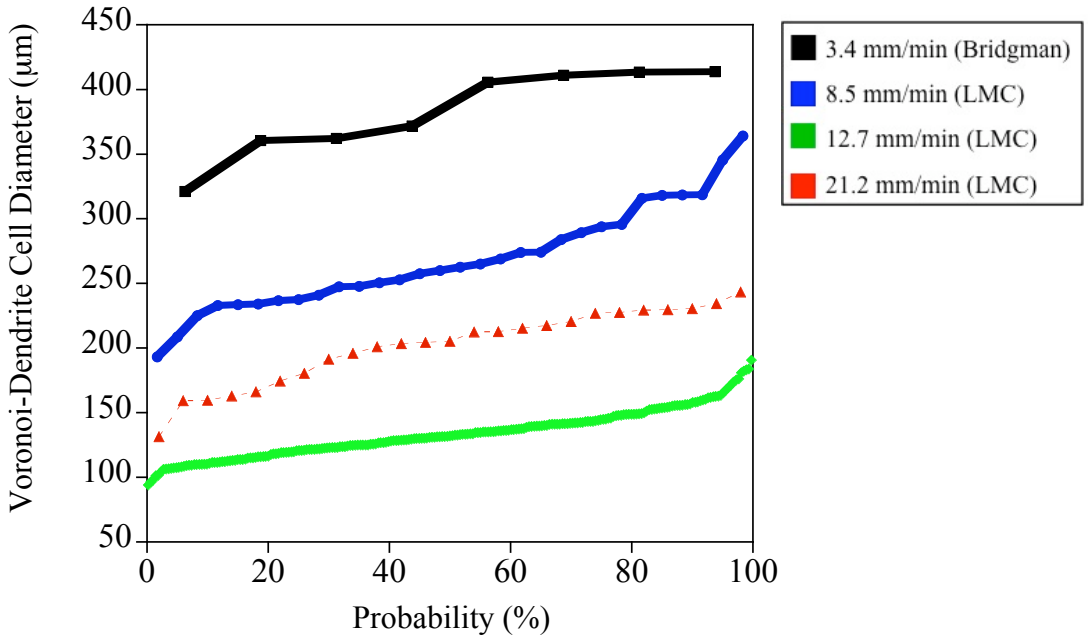

Figure 4.4 Probability distributions of Voronoi (dendrite) cell diameters for bottom center locations of a René N5 cylindrical bar solidified using selected withdrawal rates corresponding to Figure 4.2.

Figure 4.5 displays distribution curves from measuring over 1,000 primary cores from René N5 and modified René N5 alloys solidified with the LMC (12.7 mm/min) and Bridgman (3.4 mm/min) processes from top and bottom sections. A similar range in spacings was produced in the modified alloy in comparison to René N5 for both solidification processes. This finding is particularly important since Ta influences the solidification path due to preferential segregation to the interdendritic region,[8] but does not significantly alter the character of the dendrite spacings.

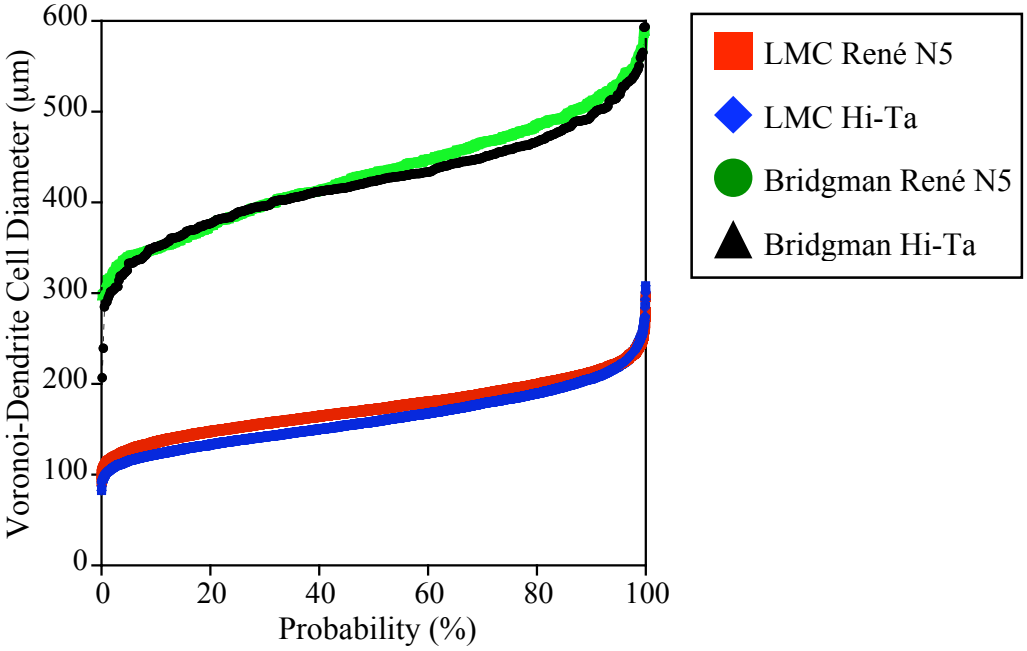

Figure 4.5 Histograms of Voronoi (dendrite) cell diameters for four variants using the LMC and Bridgman processes for casting René N5 and modified René N5 alloys.

It is apparent that there exists a continuous range in primary dendrite arm spacings at all withdrawal rates and alloy compositions. Warren and Langer[9] have pointed out that the selection of primary spacings is history-dependent if there exists a stable range of primary spacings. A theoretical model presented a lower limit of the allowable range of primary spacings through a linear stability analysis of dendritic arrays that encompassed a variety of effects:[10] build-up of a solutal boundary layer in front of the initial flat interface; onset of the morphological instability and formation of the relatively finely spaced array of dendrite tips; and coarsening of the array. These aspects can dictate the final selection of a steady-state primary spacing. At 8.5 mm/min, however, uniform primary dendrite arm spacings were not achieved in either the axial or

radial direction of the bar. The marked change in spacings suggests an existence of a morphological adjustment mechanism in the developing dendritic arrays during directional solidification. Competitive growth between neighboring dendrites may cause elimination of an existing dendrite or the formation of a new dendrite. Additionally, this process can be enhanced with misalignment from the starter or a large solid/liquid interface curvature [7, 11].

It is of interest to determine whether there is a correlation of the extremes of the spacings to the sizes of pores that serve as weak links during fatigue. It is assumed that larger spacings will allow for larger areas for pores to nucleate and grow within the interdendritic region. Alternatively, closer spacings may impede the flow of interdendritic liquid between solidified dendrites during the solidification process, thus creating pores in the structure. With this in mind, the solidified structure produced at 8.5 mm/min produced the most variability in fatigue life in comparison to all other LMC withdrawal rates, thus it is assumed that a large distribution in pores will be present in the microstructure.

4.1.1 Variation in Radial Spacing

Voronoi maps were obtained at edge and center locations of the cylindrical bars. Maps were acquired at locations within 3 mm from the edge and at center locations that were greater than 5 mm from the edge. Figure 4.6 shows examples of maps acquired from an 8.5 mm/min withdrawn casting at top and bottom locations, since this processes resulted in the largest variability in comparison to all other LMC rates. The partitions used to distinguish between each range of cell diameters are shown in the key of Figure 4.6. The difference in spacing between the edge and center locations may give an indication of the local solid/liquid interface curvature during solidification. At the bottom of the bar for this 8.5 mm/min withdrawal rate, there is a notable overall increase in spacing of at least 100 μm from an edge location to 800 μm from the edge inward, shown by the inversion of the map from predominately green (200-300 μm) compared to the predominately red (300-400 μm) maps. At this rate, it is anticipated that notable

variability in mechanical properties will be exhibited in edge and center locations of a component.

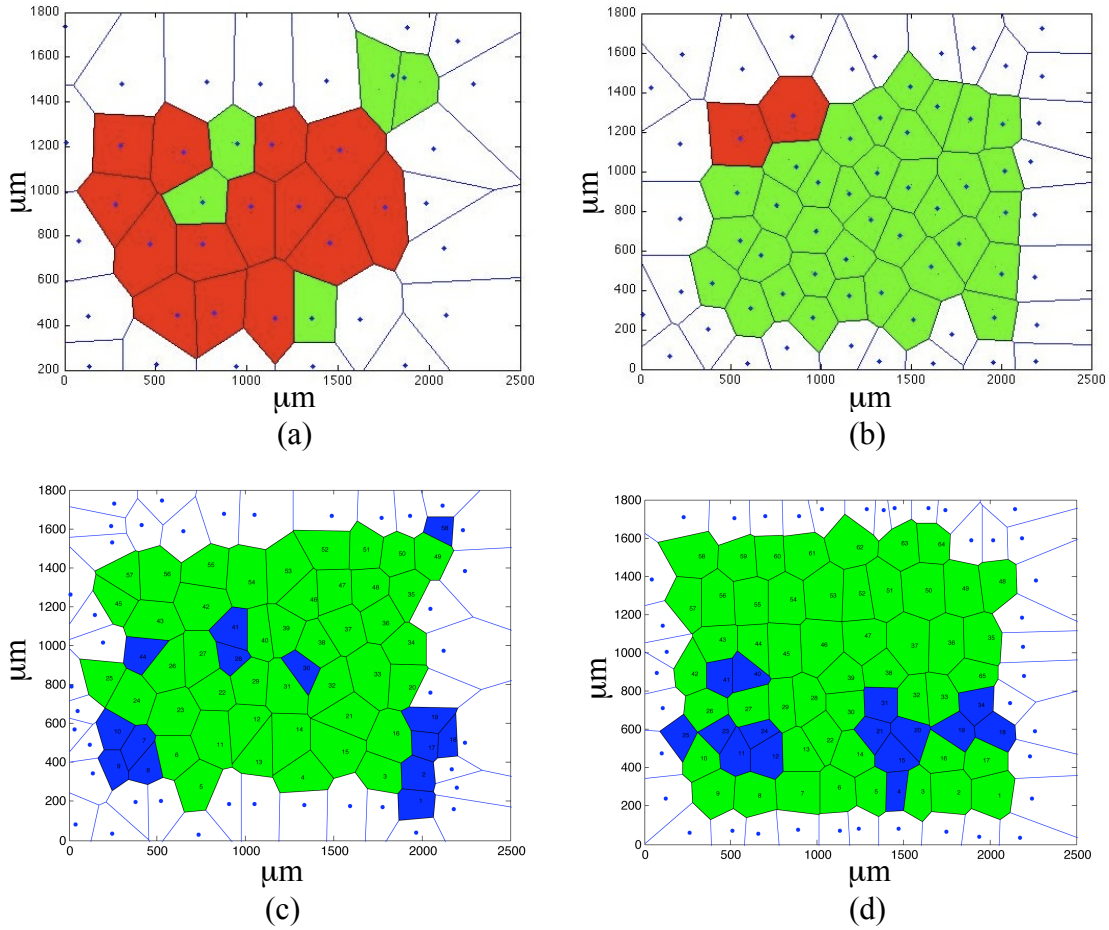

Figure 4.6 Voronoi-dendrite maps modeling the microstructure of an 8.5 mm/min solidified bar. Bottom sections illustrate the variation in spacing at the (a) edge and (b) center of a cylindrical bar. Top sections show smaller spacings at the (c) edge and (d) center.

A 100 µm difference in spacing may be problematic when using an average λ_1 as an indirect indication of the thermal gradient. Widely accepted models, proposed by

Hunt[1] and Kurz and Fisher[2], have demonstrated a functional dependence of λ_1 on the thermal gradient and solidification velocity (see Equation 1.5).

$$\lambda_1 \propto G^{-0.5} \times V^{-0.25} \qquad [4.5]$$

This relationship is typically used to estimate solidification conditions for single crystal castings, yet it assumes a completely axial temperature gradient with completely square packing of dendrites. Based on Equation 4.5, a variation of ±100-200 μm in λ_1 represents approximately a 50% difference in thermal gradient from edge to center of a bar. The local change in radial at 8.5 mm/min was likely due to the strong component of transverse heat extraction, $G_{\perp}$, produced in the LMC process.[11]

4.1.2 Spatial Packing of Dendrites

One factor that may influence the variability in spacings and pore size distribution is the type of dendritic packing structure that has evolved during solidification. Average λ_1 measurements acquired using Equation 1.7 accounts for only a square packing arrangement, despite the fact that alternative packing structures existed in various sections within the bars, Figure 4.1b. McCartney and Hunt have defined nearest neighbor spacings in the following equations for square (λ_1), hexagonal (λ_2) and random (λ_3) packing arrangements:[12]

$$\lambda_1 = \sqrt{A/N} \qquad [4.2]$$

$$\lambda_2 = 1.075\sqrt{A/N} \qquad [4.3]$$

$$\lambda_3 = 0.5\sqrt{A/N} \qquad [4.4]$$

where A is the sampling area, and N is the number of dendrite cores. Thus, up to a 20% difference in spacing can be measured for a single location depending on these geometrical factors. The impact of packing structure on the extent of interdendritic flow is of considerable interest when casting single crystals, due to the propensity for convective instabilities[13] and macrosegregation.[14] The driving force for interdendritic

fluid flow arises from the temperature and composition gradients in the casting and volume shrinkage during solidification. Previous work has detailed the trend in higher permeability with larger dendritic spacings.[15,16] Three-dimensional fluid flow modeling by Madison *et. al*[13] has also emphasized the importance of reducing the connectivity of interdendritic channels in order to reduce the formation of convective instabilities.

It is common practice in the industry to measure the average dendrite arm spacings for a given location and assume these to be representative of the entire blade. This suggests that the local material properties, such as elastic modulus and yield strength, are constant over a representative area, when, in fact, the local properties may vary strongly spatially. The Voronoi-dendrite maps obtained from the LMC solidified microstructures indicate that the dendrites are not purely random or perfectly regular. When the processing conditions provide a stable solid/liquid interface and balanced heat extraction for well oriented single crystal growth, it is expected that the structure will posses highly ordered primary dendrite arrays, with a specific packing type, along the length of the casting and the variability of material properties will be minimal.

The arrangement of dendrites and various interdendritic solidification features such as pores, carbides and γ–γ' eutectic determine the physical characteristics of superalloy materials. Minimum, maximum and average properties obtained from the Voronoi analysis of dendrite arm spacings are key input parameters for models that have the goal of linking microstructural features to the resulting fatigue life. That being said, it is necessary to ascertain the correlation between defect size and the dendritic spacings, since the fatigue properties will likely be influenced by the extremes of the defect size distribution.

4.2 Influence of Processing Conditions on Porosity

Solidification studies of single crystal superalloys commonly report the volume fraction of porosity within a casting and disregard the maximum size and distribution. However, of greater interest to properties is the maximum defect size. The maximum defect size in a component is usually acquired from systematic metallographic sectioning, which can be a tedious and time-consuming process, or radiography, with limited

resolution. The remainder of this chapter outlines a new approach to estimating the maximum pore size within a single crystal superalloy. This requires a basic overview of stereology for obtaining volumetric estimations from 2-D sections. Predicted pore volumes within LMC and Bridgman solidified material will be presented and compared to X-ray tomography studies that have recently been conducted.

4.2.1 General Observations of Porosity with Imaging Techniques

Figure 4.7 displays shrinkage pores in 2-D sections taken transverse to the withdrawal direction for both LMC and Bridgman-solidified alloys. These micrographs present a low magnification view of the size and distribution of pores within LMC and Bridgman solidified material, for each alloy variation. Even though the pores are significantly smaller in the LMC solidified material, image processing software was able to resolve the pores for 2-D area measurements.

Since pores were not only spherical, but irregular in shape, a semi empirical approach by Murakami and Endo[17] was used to characterize the pore size. The irregularity in shape makes it nearly impossible to describe their geometry accurately on the basis of a few parameters. Furthermore, prior studies have agreed that the size of the defects rather than the geometry plays a dominant role in forming cracks during the fatigue process.[17-19] By using the square root of the projected area as the measure of the pore size, the equivalent circular diameter, d, is defined as

$$d = \sqrt{\frac{4}{\pi} A_{pore}} \qquad [4.6]$$

where A_{pore} is the area of the pore measured on metallographic sections. The secondary electron images in Figure 4.8 display various pores observed on a longitudinal section. These images are presented in addition to the optical micrographs in Figure 4.7 to exemplify the size, shape and give a 2-D perspective of the depth of each pore. For the René N5 Hi-Ta alloys, instances of pores near carbides were more frequently observed than in the René N5 alloys, regardless of the solidification process.

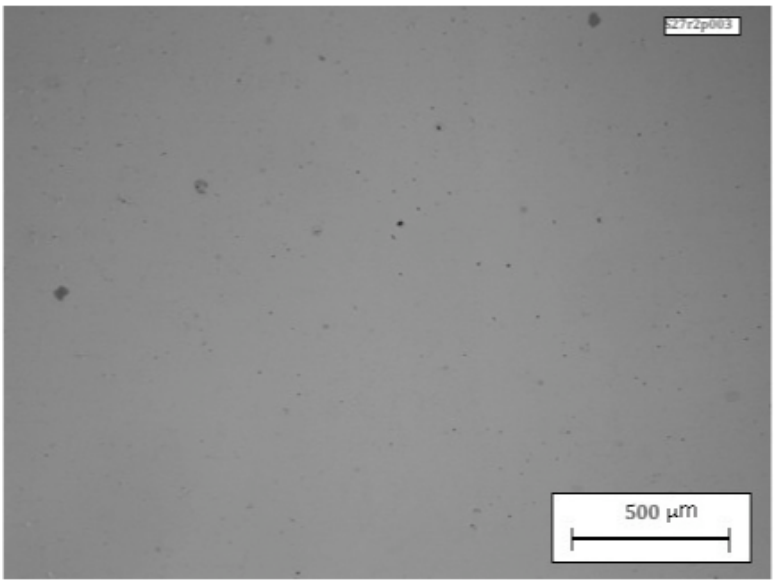

(a)

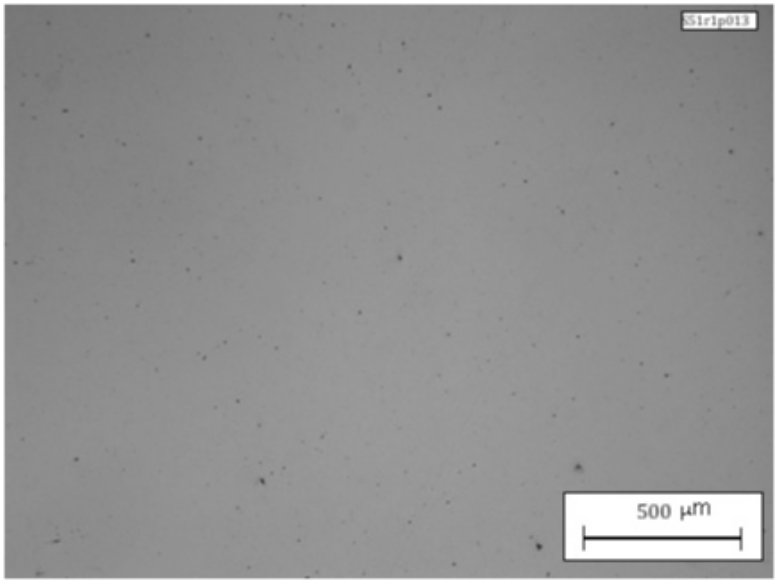

(b)

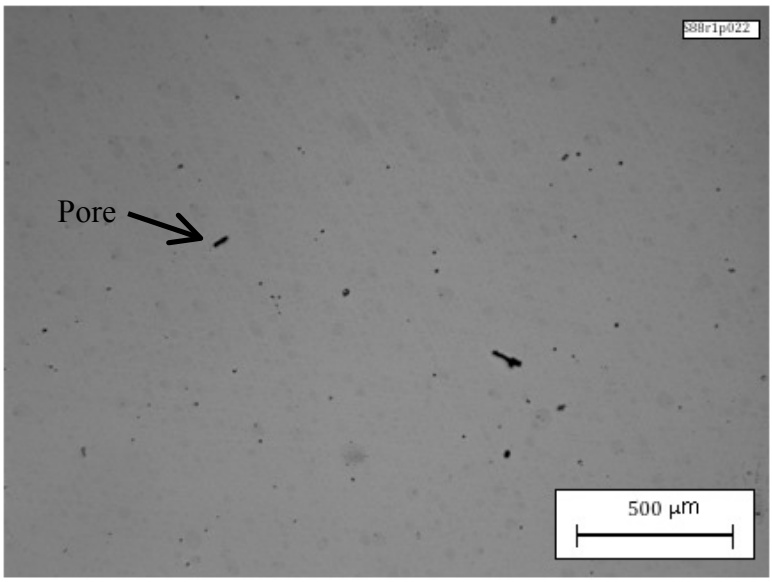

(c)

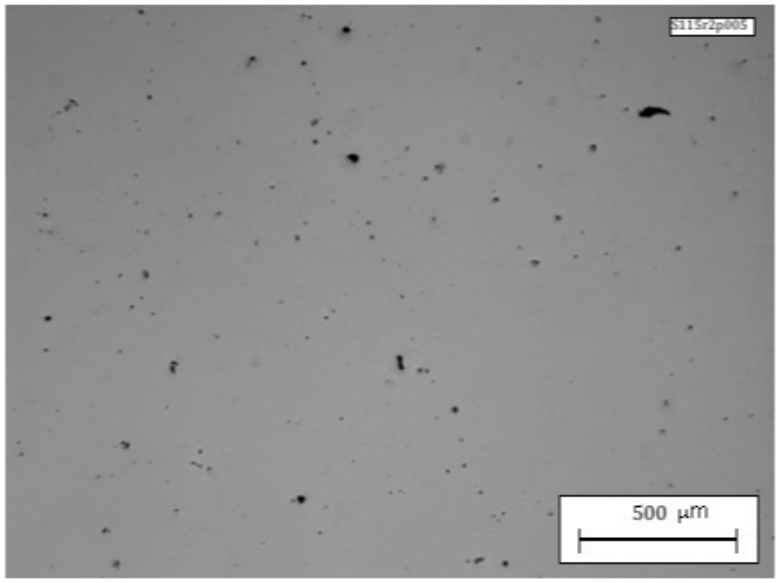

(d)

Figure 4.7 Optical micrograph of specimens sliced perpendicular to the [001] growth direction. Pores are shown as dark areas for (a) René N5 and (b) Hi-Ta LMC solidified alloys. Larger pores nucleated with the Bridgman process are shown for (c) René N5 and (d) Hi-Ta material.

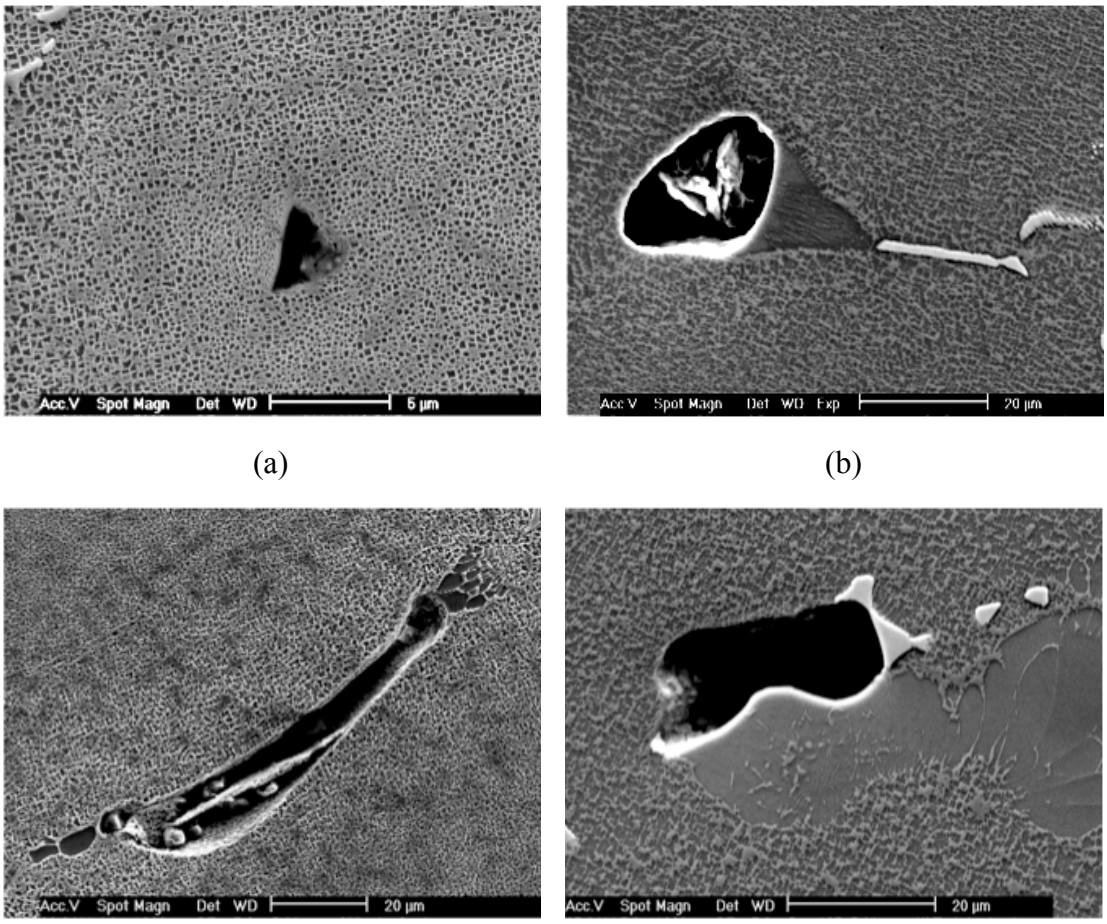

Figure 4.8 SEM images of various pores observed in longitudinal sections for (a) LMC René N5, (b) LMC Hi-Ta (c) Bridgman René N5, and (d) Bridgman Hi-Ta solidified alloys.

4.2.2 Quantification of Pore Volume

In order to quantify the volume fraction of porosity within a casting, stereological based equations can be applied to random metallographic sections. The area fraction of porosity is given as:

$$\rho = \frac{\sum_i A_p}{\sum_i A_t} \qquad [4.7]$$

where ρ is the porosity, A_p is the area of the sectioned pore, and A_t is the sectioned area of the sample. Delesse and co-workers [20,21] have described methods for determining the

volume of pores from random sectioning and measuring the relative area of the profiles, where a profile is defined as the perimeter of the 2-D shape.

It is of considerable interest to observe the variability in pore size along the length of the casting to identify where weak links may reside. Figure 4.9 displays micrographs collected from a section of at least 1 cm from the ends (top or bottom) of a LMC solidified bar. These randomly selected areas were imaged and analyzed with NIH Image software in order to estimate the difference in porosity content within the top and bottom sections of a bar. Table 4.1 details the maximum, minimum and volume fraction of pores comprised in each section. Despite a larger volume fraction of pores within the bottom section, the top section possessed larger pores. This interesting finding can be attributed to the reduced amount of liquid pressure above the pores available to impede their growth during solidification.

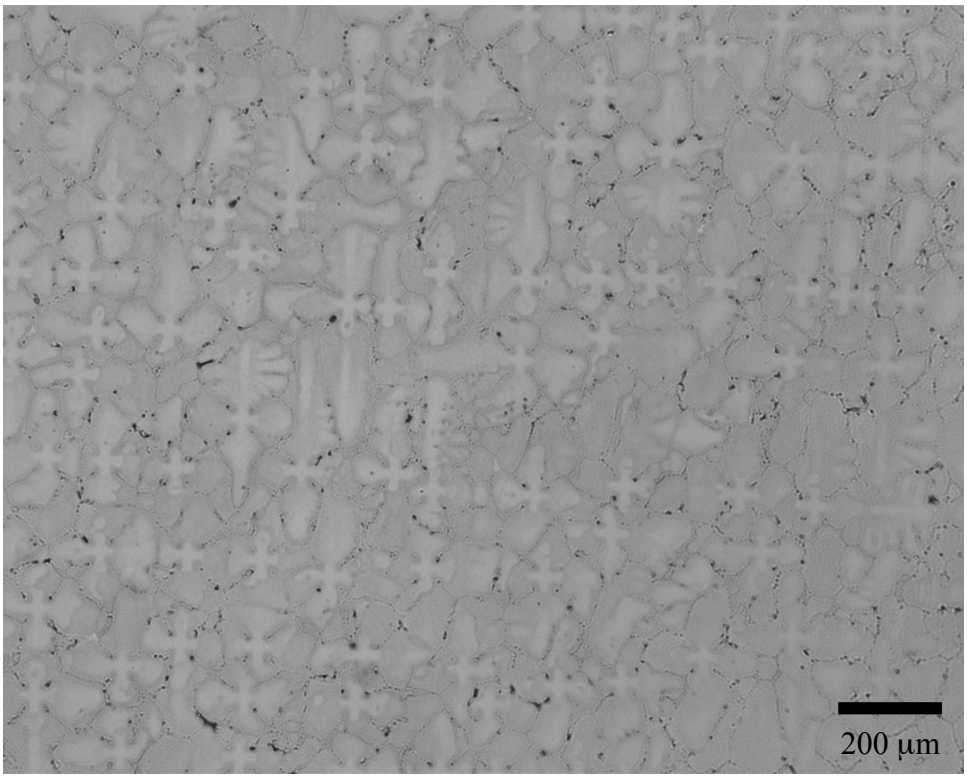

(a)

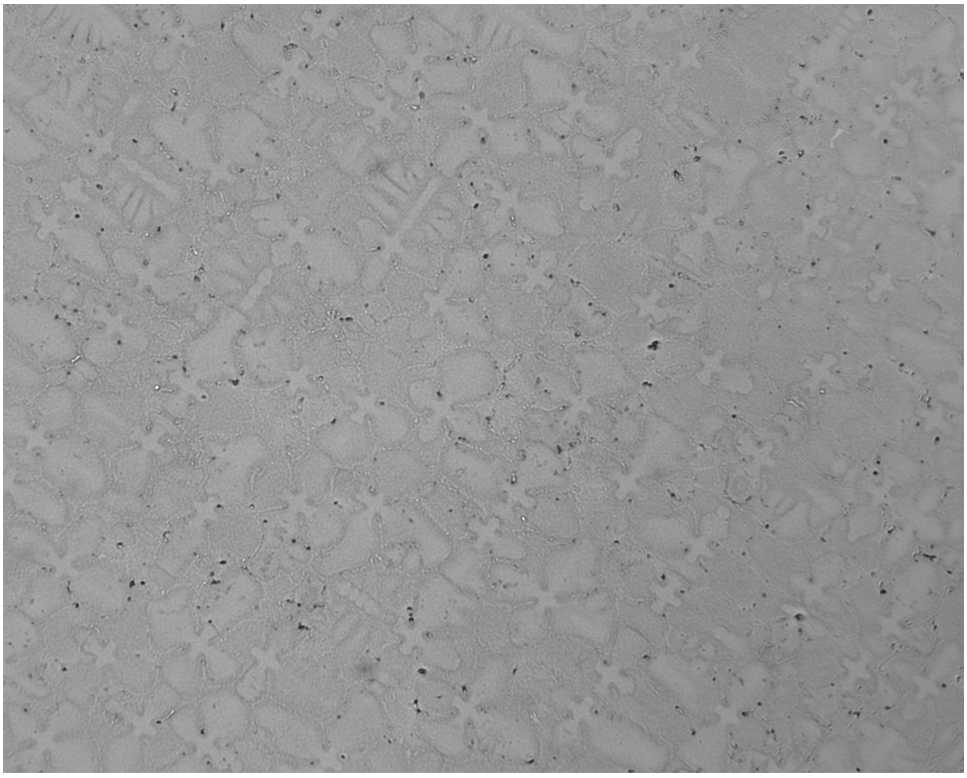

(b)

Figure 4.9 Micrographs of random sections of a LMC solidified bar (as-cast) used for pore size distribution analysis. The top random section (a) shows larger pores and higher porosity content than the bottom section (b).

Table 4.1 Porosity evaluation of a top and bottom section of a LMC solidified bar.

	Top Section	Bottom Section
Maximum Pore Area	404 μm^2	181 μm^2
Minimum Pore Area	0.81 μm^2	0.81 μm^2
Porosity	0.2%	0.5%

Images in Figure 4.8 and Figure 4.9 reveal the variety of possible 3-D shapes and sizes of pores within LMC and Bridgman solidified material, with the latter containing larger pores. Ultimately a 3-D perspective of the porosity contained with these alloys is necessary to identify the volumetric size, connectivity and distribution within the interdendritic region. This may aid in controlling the microstructure and achieve targeted properties, especially if pores are likely to form in specific regions.

To provide as complete and unbiased 3-D description of porosity as possible, studies have utilized serial sectioning and X-ray tomography. The former method acquires 3-D characterization data at the macroscale volumes (cm^3) with microscale resolution by sectioning a volume of material at specific fine-scale increments. The material is subsequently reconstructed in 3-D using imaging techniques. Unfortunately, the sample volume is entirely consumed during the data collection process, which precludes any re-examination of the material post-analysis.

X-rays provide a non-destructive means of collecting porosity information in an opaque volume of material by reconstructing a suite of transmission images taken at various projections.[22] X-ray imaging techniques are extremely sensitive to the differences in atomic numbers and density, therefore the porosity can be readily detected. However, serial sectioning and X-ray tomography are costly, time consuming and unfortunately were not readily available for this research. Therefore, quantitative stereology was used to obtain 3-D quantities of 2-D sections and compared to 3-D characterization results from the literature.

4.3 Novel Approaches for Single Crystal Porosity Evaluation

Stereological methods have been widely used to determine geometric properties of three-dimensional structures on the basis of information from two-dimensional sections.[21,23-25] Application of statistical methods which predict the 3-D distribution of defects sampled from two dimensional micrographs, will be discussed in this section for single crystal alloys. It should be noted that only a few studies have attempted to acquire 3-D information of pores within metallic materials.[26-28] The following sections will include: (1) a brief introduction and overview of stereology, (2) results of X-ray tomography of pores to evaluate 3-D shapes and sizes, (3) comparison of tomography data to pore measurements obtained from stereographic measurements, (4) evaluation of pore sizes for the four variants being evaluated in this research, and (5) a statistical approach to predict the maximum pore size.

4.4 Fundamental Formulae of Stereology

Figure 4.10 depicts a schematic of a random 2-D plane cutting an aggregate of three-dimensional pores. The relationship between the volume of pores and the total material volume can be derived using Equations 4.11-4.13. Additional basic equations that relate points, P, lines, L, surfaces, S, areas, A, and volumes, V are also shown in the equations.[21] For a random plane section of a three-dimensional specimen, the fundamental formula apply[21]

$$V_V = A_A = L_L = P_P \quad [4.11]$$

$$S_V = \frac{4}{\pi} L_L = 2P_L \quad [4.12]$$

$$L_V = 2P_A \quad [4.13]$$

As one can observe, metallographic sectioning of samples only acquires 2-D projections of 3-D shapes. So, it is questionable as to whether the maximum pore is actually being measured from sectioning. Therefore, comparison of stereological measurements to 3-D pore data is of particular interest.

Table 4.2 summarizes the definitions for the principal symbols used in stereology. The equalities are applicable in a statistical sense, which requires that the surface analyzed should be representative of the sample volume, and the phase must be randomly distributed within the volume. Hence, the measurement of A_A is an unbiased statistical estimate for V_V.

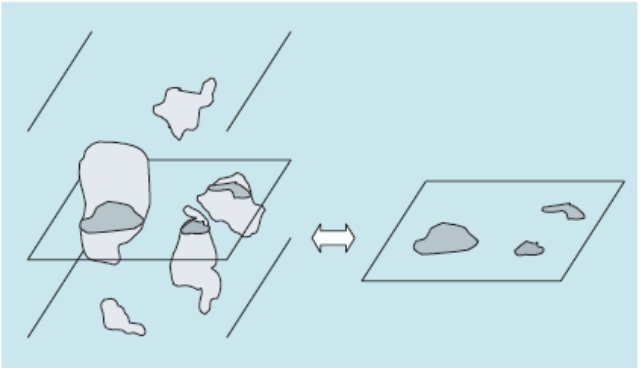

Figure 4.10 Schematic of a volume of particles and a 2-D section displaying the means for measuring the areal and volume fraction.[21]

Table 4.2 Basic stereology symbols and definitions[21]

Symbol	Definition	Symbol	Definition
P	Number of point elements	S_V	Surface area per unit volume
P_P	Point fraction	V	Volume
P_L	Number of point intersections per unit test line	V_V	Volume Fraction
P_A	Number of test points per unit test area	N	Number of features
P_V	Number of test points per unit test volume	N_L	Number of interceptions per unit line length
L	Length of lineal elements	N_A	Number Area
L_L	Lineal Fraction	N_V	Number Density
L_A	Length of lineal elements per unit test area	L_{AVG}	Average lineal intercept
L_V	Length of lineal elements per unit test volume	A_{AVG}	Average areal intercept
A	Planar area	S_{AVG}	Average surface area
S	Surface area	D_{AVG}	Diameter
A_A	Area Fraction	V_{AVG}	Average volume

From experimental observations on transverse and longitudinal metallographic sections, it is not clear whether the pores within single crystals are entirely oblate, prolate or spherical. Link *et al.*[28] has investigated porosity in single crystal nickel-base superalloys CMSX-6, SRR99, CMSX-4 and CMSX-10 using synchrotron X-ray tomography. This investigation supplied information pertaining to the 3-D distribution of pores and a statistical database of pore sizes and shapes. The pores that can be observed in the X-ray tomography images (Figure 4.11), are roughly equiaxed, so simple expressions will be utilized for analysis. X-ray tomography data by Link *et al.*[27] has also supplied valuable information about the three-dimensional distribution of pores and a statistical database of pore sizes and shapes. Using X-ray tomography with 1 μm resolution, three-dimensional views of the pores and their arrangement have been

observed. The images in Figure 4.11 show tomographs of heat-treated CMSX-10 (a) before and (b) after data processing was applied in order to remove artifacts.[28]

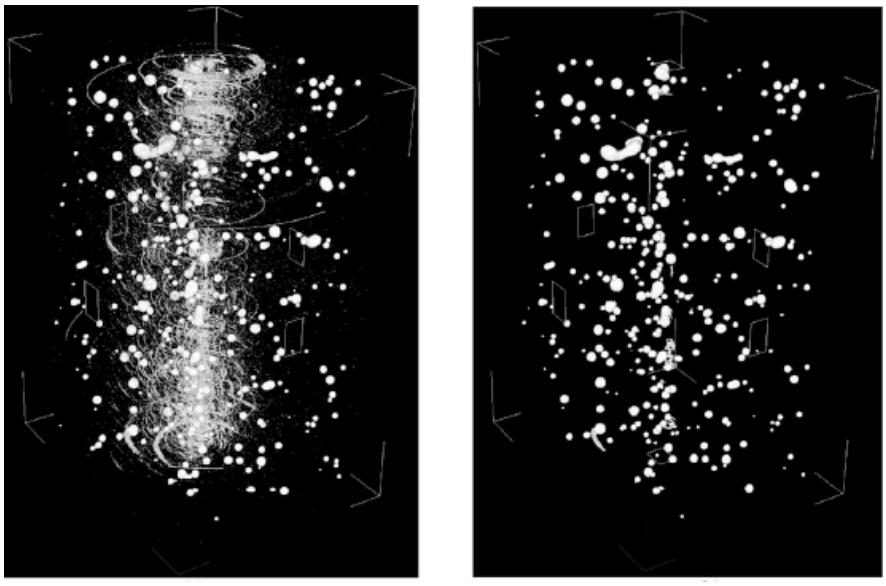

(a) (b)

Figure 4.11 Tomograph of heat-treated CMSX-10 displaying the porosity within the material. (a) The binarized volume consists of pores, point artifacts and ring artifacts before a ring filter was applied. (b) View of the pores within the sample after objects containing less than 27 voxels were deleted, as well as objects with a shape factor < 0.7 and less than 25 pixels in height. Total volume of the box = 500 µm × 500 µm × 800 µm. Images displayed in Link *et al.*[28]

After extensive processing of the three-dimensional images as described by Link *et al.*,[28] 3-D shape factor measurements were applied based on

$$S = 6\sqrt{\pi}\left(\frac{V}{A^3}\right) \qquad [4.23]$$

where S is calculated from the volume, V, and the surface area, A. S is equal to 1 for a perfect sphere and a shape factor limit of 0.7 was applied, which is considered a cube.

The porosity distribution by area of a René N5 Bridgman solidified sample is shown below (Figure 4.13) for comparison to the porosity distribution found in the tomography results displayed in Figure 4.11 for CMSX-10. It should be noted that both alloys contained a similar average PDAS of approximately 0.3 mm. However, the CMSX-10 sample analyzed with tomography had a lower volume fraction of porosity of 0.17%, in comparison to the René N5 sample analyzed in Figure 4.13 (0.2%). However,

in order to compare the 2-D vs 3-D data, the CMSX-10 pore size distributions in Figure 4.12a-c is shown for comparison to Bridgman solidified René N5 data in Figure 4.13.

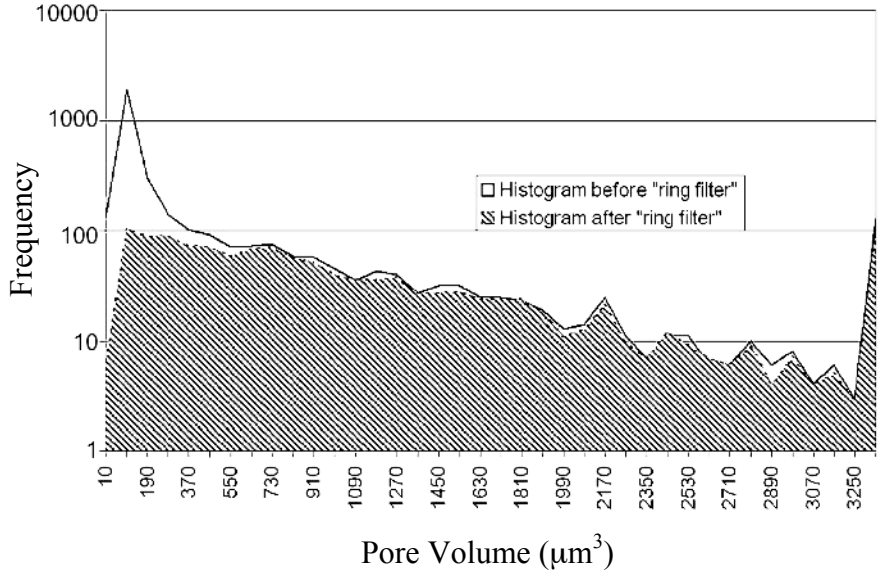

(a)

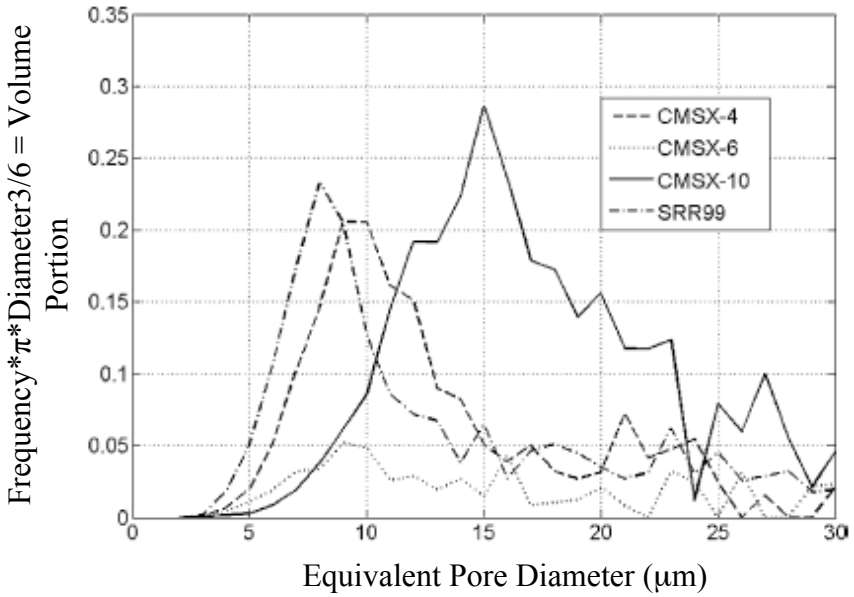

(b)

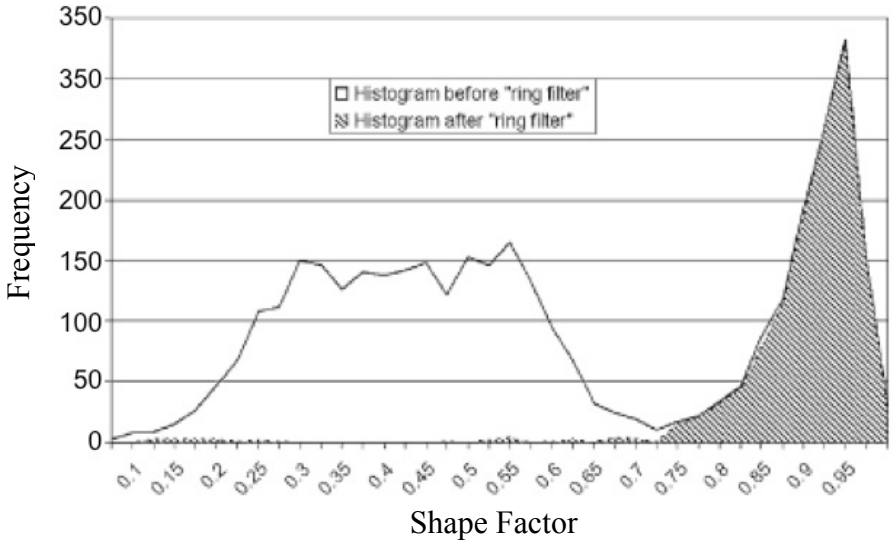

(c)

Figure 4.12 (a) Histogram of pores within a sample of CMSX-10 showing the distribution of the equivalent pore size before and after the application of a "ring-filter" (removal of artifacts). (b) Porosity in heat-treated underformed superalloys as a function of equivalent pore diameter, *d*. (c) Shape factors of pores in CMSX-10. Data shown in Link *et al*.[28]

For the data set recorded in Figure 4.11, the total volume recorded was 0.5 mm × 0.5 mm × 0.8 mm, which is on the order of a dendrite stalk with nearly 8 secondary arms. The X-rayed area is mainly the interdendritic region between two dendrite cores. The maximum pore size measured for René N5 was significantly larger than observed in Figure 4.12a for CMSX-10 at an estimated volume of 3.7×10^4 μm^3 using stereology. Based on the stereology formulae in Equation 4.11, a tomography experiment would require a volume greater than 0.5 mm^3, compared to the 0.2 mm^3 for the tomography dataset in Fig. 4.11. Therefore, it can be assumed that larger pores may be present in the CMSX-10 material, which may be observed with increased sampling.

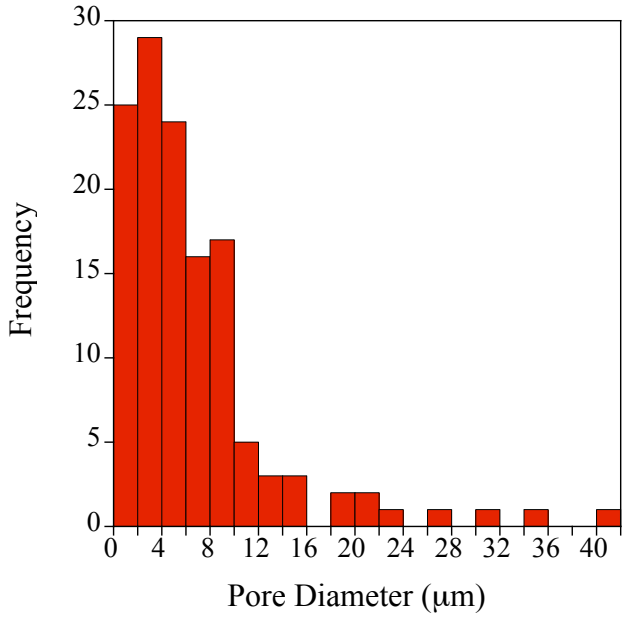

Figure 4.13 A histogram of pores from a random section from a Bridgman solidified René N5 sample for comparison to Figure 4.11b.

Figure 4.14 shows the distribution of the pore sizes measured for 2-D metallographic sections for the LMC and Bridgman solidified René N5 and Ta-modified alloys. At least 3,000 pores were measured from each variant to generate distribution curves of pore diameters. The maximum pore diameters for each variant are shown in Figure 4.15, with the volume of material estimated for each variant using stereology displayed in Table 4.3. Approximately a 65% reduction in maximum pore size was measured within the LMC castings in comparison to Bridgman. Larger pores were measured in the Hi-Ta alloys for the respective solidification processes. It is apparent that for a broader pore size distribution, increased numbers of pores must be measured to predict the pore size distribution compared to a narrow pore size range with the same precision.

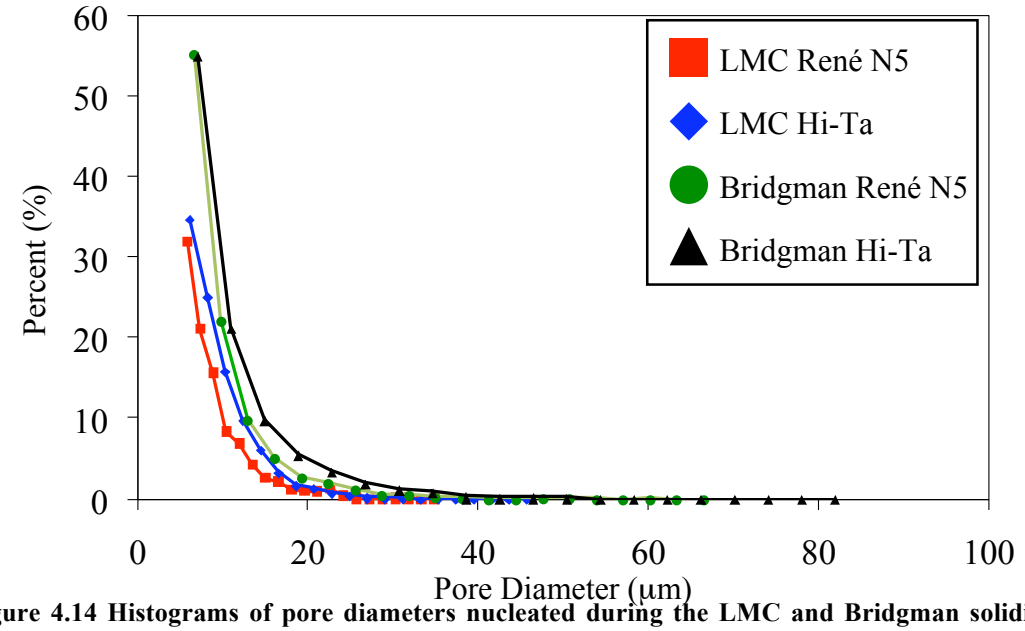

Figure 4.14 Histograms of pore diameters nucleated during the LMC and Bridgman solidification process for four variants of René N5.

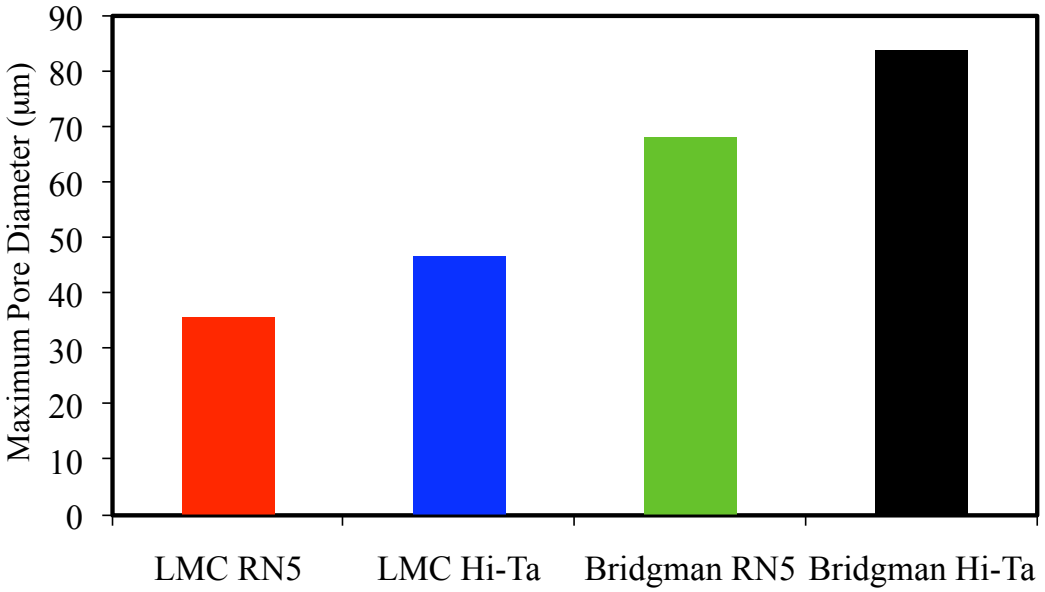

Figure 4.15 Maximum pore diameters measured for four variants of René N5.

Table 4.3 Volume of material evaluated for each variant detailed in Figure 4.15

	Total Pore Area (mm^2)	Section Area (mm^2)	Porosity	Total Pore Volume (mm^3)	Volume of Material (mm^3)
LMC N5	0.13	31.6	0.41%	1.21×10^{-3}	0.29
LMC Hi-Ta	0.24	49.7	0.48%	2.38×10^{-3}	0.50
Bridgman N5	0.17	59.2	0.29%	1.84×10^{-3}	0.64
Bridgman Hi-Ta	0.33	93.3	0.35%	6.94×10^{-3}	1.98

4.5 Implications of Maximum Pore Size on Fatigue Life

When defects become the fracture origin within a component, it is likely that the fatigue failure will occur at the largest defect or inhomogeneity that is present in the volume.[23] The fatigue strength is then controlled by the extreme values of the population of defects rather than the average size.[23,28-30] A suitable statistical method to evaluate life-limiting pores is needed; in this research analysis of the extremes was conducted employing an approach based on extreme value analysis.

When a fixed number of sampling points follow a lognormal distribution, Murakami and co-workers[30,31] have observed that the maxima and minima obtained from each set will also follow a distribution when plotted simultaneously. The construction of a statistics of extreme graph[32] is possible if the slope of the distribution of extremes decreases exponentially. If the pore distribution of extremes is doubly exponential, the statistics of extreme values (SEV) can be applied and the prediction of the maximum pore size within a given area or volume is possible.

Defects can easily be sampled and measured from metallographic sections[23,30,31,33] for SEV analysis, which was first implemented by Murakami and co-workers.[23,30,31] The SEV technique was applied to porous metallic materials for the purpose of gaining estimations of extreme defect sizes within a specific volume, which can subsequently represent a simple fatigue quality control approach for materials and components.[23,34,35]

The SEV has a probability density function described as[33]

$$f(x) = \frac{1}{\delta} \bullet \exp\left\{-\frac{x-\lambda}{\delta}\right\} \bullet \exp\left\{-\exp\left[\frac{x-\lambda}{\delta}\right]\right\} \quad [4.24]$$

and a cumulative probability function (CDF) given as

$$F(x) = \exp\left\{-\exp\left[-\frac{x-\lambda}{\delta}\right]\right\} \quad [4.25]$$

where λ and δ are the location and scale parameter, respectively. A fixed standard inspection area, S_o, is typically taken from a microscope image, which includes a maximum defect size. The square root of the projected area of this defect is then calculated and classified among a variety of defect sizes, from smallest to largest. For a desired area of prediction, S, the return period is described as $T=S/S_o$. If V_o is the inspection volume for detecting the defects and V is the volume of the component under examination, the maximum defect occurring in the component has a return period $T=V/V_o$. The cumulative probability based on volume is given as

$$P = 1 - \frac{1}{T} \quad [4.26]$$

The P-th percentile of the distribution is:

$$x(P) = \lambda - \delta \bullet \ln\left[-\ln\left(1-\frac{1}{T}\right)\right] \quad [4.27]$$

The maximum pore area for a specific casting geometry can be derived according to Murakami and Toriyama,[23] by plotting the reduced variates, y_j, versus $(\text{area})^{1/2}$. The reduced variates arise from $-\ln(\ln(F(x)))$. The sampled pores are indexed by j to n starting with the smallest defect area:

$$y_i = -\ln\left[-\ln\left(\frac{j}{n+1}\right)\right] \quad [4.28]$$

If the curve obtained is approximately linear, it can be assumed that the pores are within a single distribution and the largest pore size that can be expected in a volume can be calculated. An example of a graph of extremes for data sets acquired from René N5

LMC (12.7 mm/min) and Bridgman (3.4 mm/min) solidified material (Figure 4.16). Since a straight line can be drawn through the data points within the confidence bounds (10% < F < 85%),[36] then by implication, the distribution is doubly exponential in the form as required by the statistical analysis of extremes technique (Equation 4.25). It should be noted that due to the resolution limit of measurement, the entire distribution may not be lognormal.

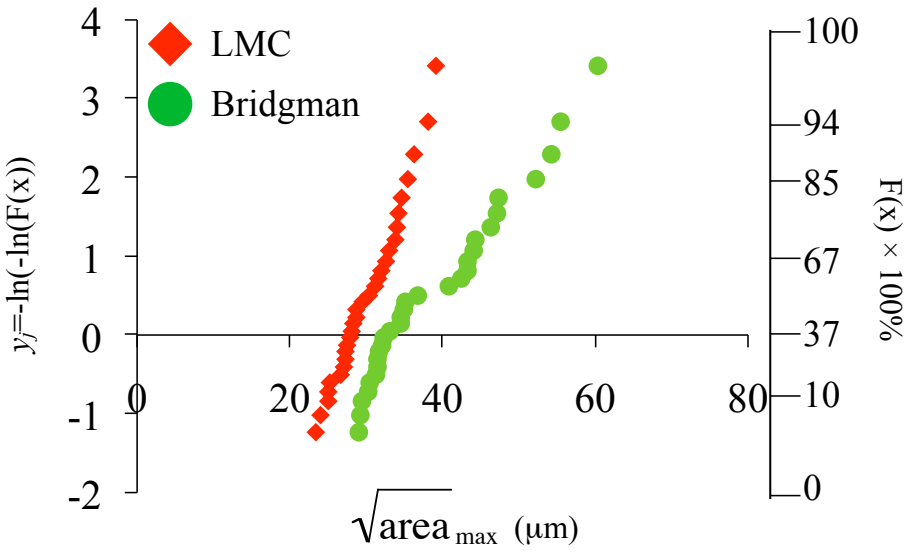

Figure 4.16 Graph of statistics of extremes for a LMC (12.7 mm/min) and Bridgman (3.4 mm/min) solidified René N5 bars.

The linear distribution of the maximum size of pores can be expressed as

$$\sqrt{area} = a \times y + b \qquad [4.29]$$

where a is the slope and b is the intercept. After calculating the return period for a specified predicted area or volume, the $-\ln(-\ln(x(P)))$ from Equation 4.27 can be used to predict a √area from Figure 4.16. This analysis is valuable for evaluation of the maximum pore size within a gage section volume of a fatigue specimen and comparing the predicted maximum pore size to the actual fatigue initiation sites. For the total area evaluated for the LMC René N5 material (Figure 4.14), the SEV analysis (S_0 = 2.79 mm^2) predicts a maximum pore diameter of 35.7 μm. This value is in agreement with the

experimental sectioning data presented in Figure 4.15, which is d_{max} = 36 μm for the LMC René N5 alloy. Statistical evaluation of maximum pore sizes within Bridgman and LMC as-cast solidified will be presented in Chapter 5, along with the actual fatigue site sizes for comparison.

4.6 Influence of Ta Additions on Solidification Structure

Figure 4.17 displays micrographs of a (a) René N5 and (b) Ta-modified René N5 alloy solidified with the Bridgman process. The white phase, which is script/blocky carbides, is clearly more prevalent within the interdendritic area of the Ta-modified alloy.

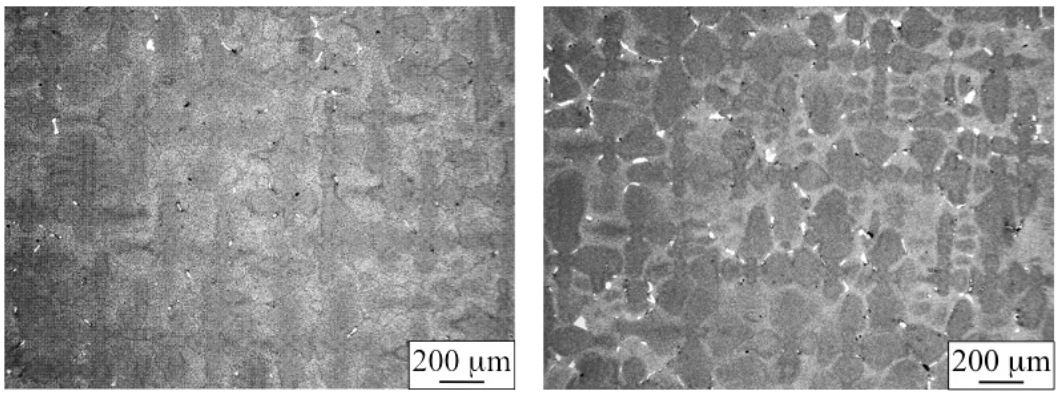

(a) (b)

Figure 4.17 Optical images depicting the variation in γ–γ' eutectic produced in (a) Bridgman René N5 and (b) Bridgman Hi-Ta solidified samples.

It is worthwhile to investigate the impact of Ta additions on the heterogeneity of LMC solidified microstructure, since previous investigations have indicated an existence of significant solute segregation during solidification.[37] Additionally, since Ta is a substitutional solid, the formation of a new solid phase or phases directly from the melt can occur, which depends on the solidification path. Ta influences the solidification path, depending on the weight pct composed in the alloy composition and can dictate whether the γ′ phase is formed by eutectic or eutectic and peritectic solidification. This occurs particularly in the late stages since it segregates to the interdendritic region and results in slightly altered fractions of eutectic γ–γ′. The segregation process may induce a buoyancy-driven convective fluid flow and can result in the formation of freckles, but was not observed in this study. Despite the possible change in solidification path due to

the Ta modification, similar primary core spacings were produced for both LMC and Bridgman processes. Yet, the increase in TaC formation may have attributed to the larger pore size exhibited in Figure 4.14. One possible reason for this occurrence is the presence of structurally intricate Ta-carbide networks in the interdendritic area that impede the fluid flow in the dendritic channels during solidification.[38]

4.7 Porosity, Dendritic Structure and Weakest Link Theory

It has been observed in the literature that fatigue mechanisms are based on the weakest link theory, where failure initiates at the weakest point of the material. Barsom and McNicol have presented a discussion on the weakest-link model[39] and Cashman[40] has recently used a similar procedure to understand competing mechanisms in fatigue failures within polycrystalline René 95. When a structure is subjected to a cyclic stress, the concept of a weak links arises because the strength of the entire component is limited by the strength of its weakest location. It is assumed that the pores near the high end of the size distribution for a given solidification condition will create the weak links where failure will initiate. Thus, it is of considerable interest to predict the locations of these weak links within the single crystal microstructure in order to obtain a correlation to the fatigue properties. The relationship between the primary dendrites and pore locations for LMC (12.7 mm/min) and Bridgman (3.4 mm/min) solidified crystals can be observed in the Voronoi maps presented in Figure 4.18. Circles that reside at Voronoi cell boundaries are generally representative of pores that formed near dendrite tips and in some cases between secondary arms.. Circles near the dots were identified as pores formed near the root of dendrite stalks. Significant pore clustering was observed within both casting processes, which is particularly important when determining the stress concentration within a surrounding area.

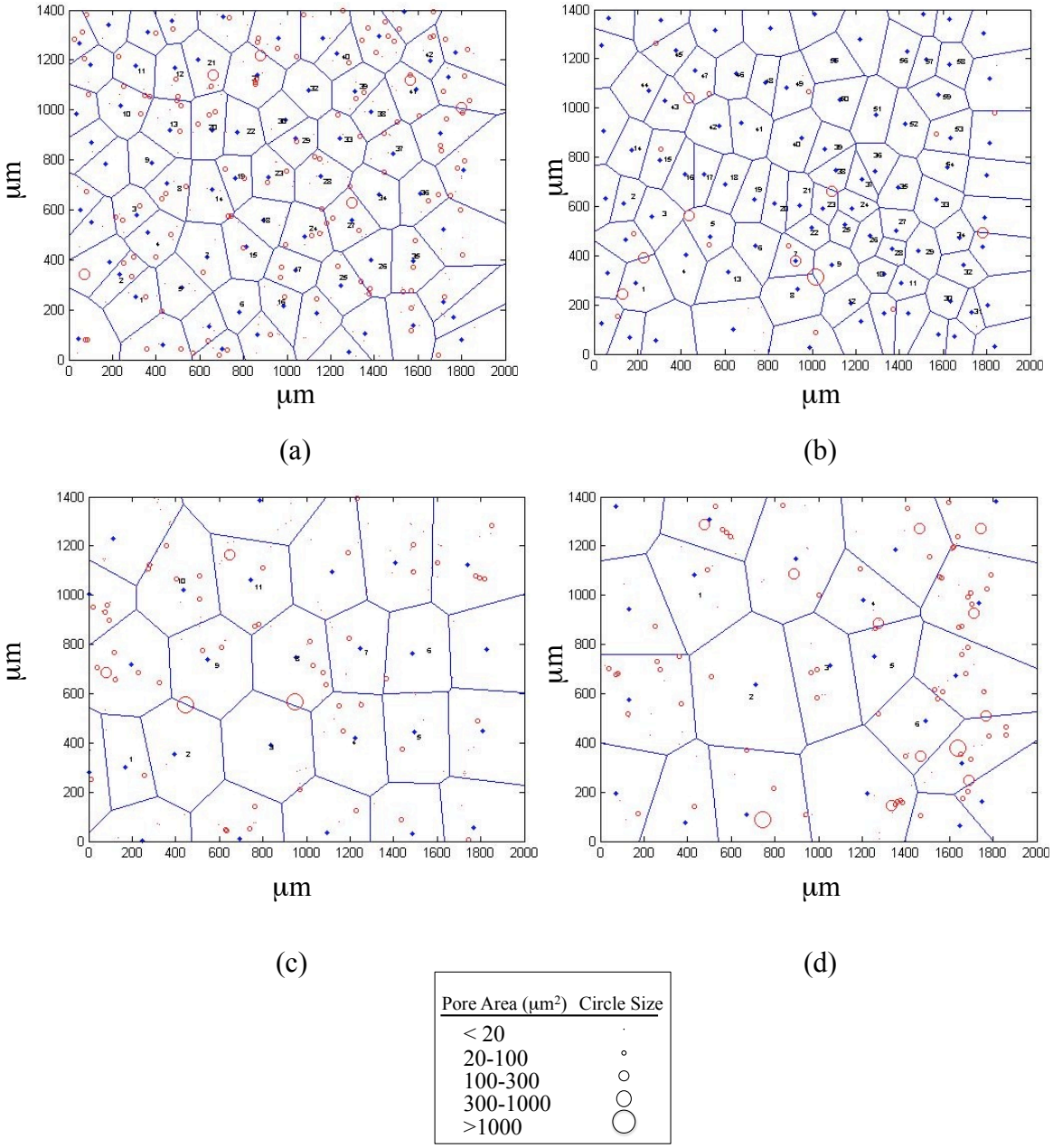

Figure 4.18 Voronoi (dendrite) maps of (a) René N5 and (b) Hi-Ta solidified alloys with the LMC process at 12.7 mm/min. Bridgman cast René N5 and Hi-Ta maps are shown in (c) and (d), respectively, for the 3.4 mm/min rate. Cast transverse sections with associated porosity locations and sizes are designated by circles within cells. Voronoi polygons are constructed only with respect to the primary dendrite cores.

The correlation between pore area and Voronoi cell area is shown in Figure 4.19. Surprisingly, the largest pores are concentrated towards the center of the distribution of cell sizes, rather than within the largest cells, representative of larger primary dendrite spacings. This was true for both Bridgman and LMC castings. Furthermore, a smaller range in pore size was observed in LMC cast material.

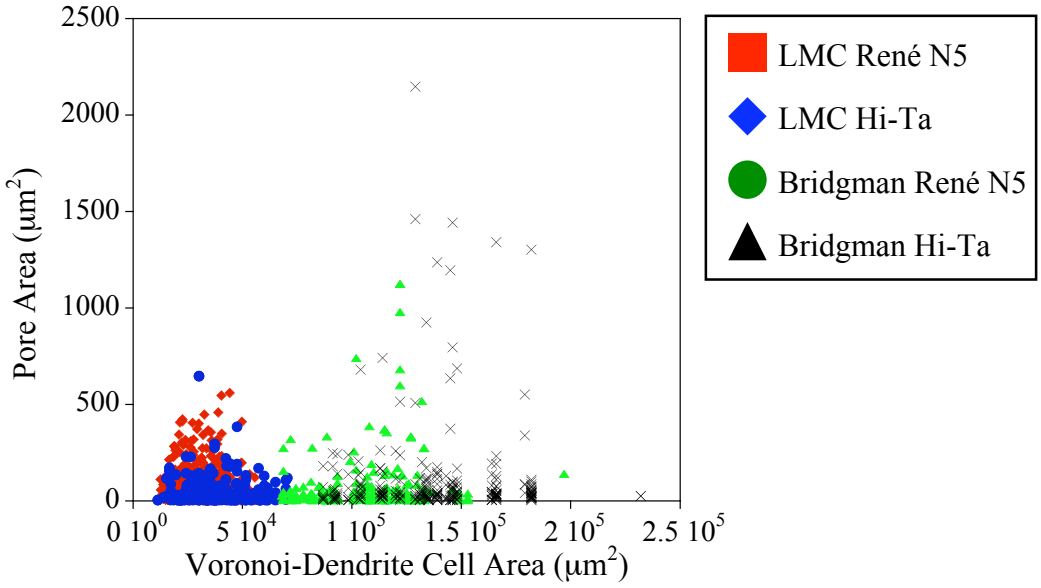

Figure 4.19 A minimum of 3,000 pore area measurements from Bridgman (3.4 mm/min) and LMC (12.7 mm/min) cast material are correlated to Voronoi (dendrite) cell areas.

At least 100 pore sizes were measured from top sections sliced parallel to the withdrawal axis from withdrawal rates of 8.5-21.2 mm/min (LMC) and 3.4 mm/min (Bridgman). Secondary dendrite arm spacings were measured at least 50 μm away from the pore location to obtain a correlation of maximum pore size and average λ_2. Each data point in Figure 4.20 represents either an average λ_2 from measuring over 200 arms per withdrawal rate, or the maximum pore size per section. It should be noted that 10.5 mm^2 of cross-sectional area was observed to obtain the maximum pore size for the data below.

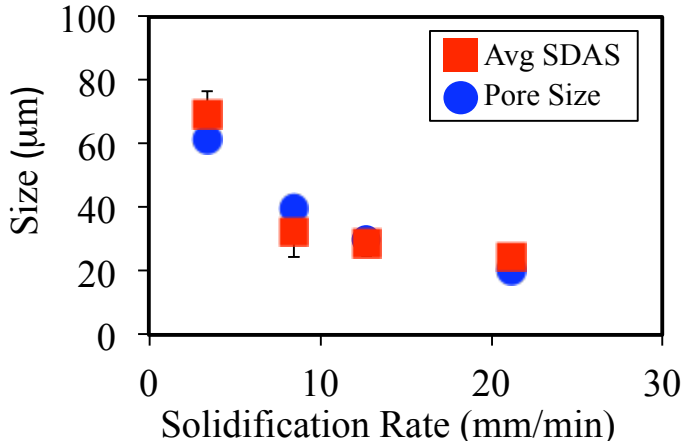

Figure 4.20 Dependence of maximum pore size and average SDAS on withdrawal rate for the LMC solidified bars at 8.5-21.2 mm/min and Bridgman cast bars at 3.4 mm/min. Each SDAS data point represents a total average measurement obtained from nearby pore locations.

4.7.1 Connecting Processing to Final Microstructure

Since it is desirable to link the microstructure to the mechanical properties, it is of particular importance to quantify the variability in dendritic spacing and its relationship to the largest defect (pore) size following solidification. Voronoi statistics are useful for the determination of the range in dendrite spacings (Figure 4.5) rather than only an average λ_1 value from a specific area. Moreover, this range can be quickly obtained to observe how the average varies with change in cooling rate. Nearest-neighbor spacings, illustrated in Figure 4.3, give insight to the degree of homogeneity in microstructure, which decreases with increasing withdrawal rate with the LMC process, up to the optimal rate. Changes in the solidification velocity using the LMC process influenced the dendrite packing structure by increasing the range in nearest neighbors. This is a reflection of the thermal gradient inducing different selection mechanisms including dendrite branching and competitive growth.[41]

The large range in λ_1 spacing observed within the 3.4 mm/min casting is associated with the large range of pore sizes (Figure 4.19), which may act as stress concentrators during fatigue and initiate cracks. As observed in Figure 4.20, pore size decreases with increases in withdrawal rate, not necessarily refinement in PDAS. This suggests that pore refinement is more strongly correlated to SDAS and cooling rate, rather than PDAS.

The relationship between dendrite arm spacing and maximum pore size remains to be developed, as discussed in the next section. Additionally, the large variability in λ_1 is also expected to result in a greater degree of property variability and lower maximum properties in the Bridgman cast material, in comparison to the LMC material.

4.7.2 Determination of Maximum Pore Size at Critical Dendritic Spacing

By linking Voronoi statistics and pore mapping, a rigorous relationship between primary dendrite spacings and pore size has been established for the 3.4 mm/min and 12.7 mm/min withdrawal rates. Since dendrites strongly influence the fluid distribution and fluid flow in the mushy zone, it is expected that they would influence pore size.

A significant observation within this study is that the largest pores are associated with the average primary dendrite arm spacings, rather than those at the high end of the spacing distribution. This suggests competing mechanisms. Primary dendrite spacings will be dependent on imposed solidification parameters, such that λ_1 is a function of $G^{0.5}V^{-0.25}$, where G is the thermal gradient and V is the solidification velocity.[42] Taking into account that the 3.4 and 12.7 mm/min solidification velocities produced constant dendrite arm spacings throughout the entire length of the casting and the fact that the pores develop from shrinkage of the final eutectic liquid at a fraction f_l rather than from dissolved gas, it is expected that the pore diameter, d_{pore}, will increase with λ_1: [43]

$$d_{pore} = \frac{f_l \lambda_1}{2} \qquad [4.30]$$

While there is a trend toward larger pores with larger dendrite arm spacings, Figure 4.20, the largest pores are not always located at the boundaries between the largest Voronoi cells. Thus it is useful to consider pore formation in terms of the driving forces for fluid flow in the mushy zone in the late stages of solidification. Pores nucleate heterogeneously when the local pressure to close the pores is exceeded by the local pressure to open the pores.[44] Specifically, when the local liquid metal pressure, p_L, becomes smaller than a critical pressure, the susceptibility of pore formation increases. The following equation assumes the critical pressure to be assumed a constant close to zero:

$$p_L = p_o + p_m - \Delta P \qquad [4.31]$$

where p_o and p_m are the external and metallostatic pressures, respectively, and ΔP is the pressure drop associated with the liquid metal flow through the mushy zone. Liquid-vapor interfacial energies are neglected due to the limited solubility of gas in the liquid and the absence of spherically-shaped gas porosity. The pressure drop, ΔP, is related to the permeability of the dendritic array according to Darcy's law:

$$v = \frac{K}{\mu L} \Delta P \qquad [4.32]$$

where v is the bulk velocity of the fluid, K is the permeability of the porous medium, μ is the viscosity of the liquid, and L is the length of the porous medium. Given the imposed velocities during directional solidification, increases in permeability should decrease the pressure drop, thus inhibiting the heterogeneous nucleation of pores within the interdendritic area. Thus pore size should thus be maximized when there is a balance between the interdendritic space available for a pore and the permeability associated with a favorable net pressure.

The permeability is influenced by the fraction liquid (fraction eutectic at final solidification), the primary dendrite arm spacing and S_v, the surface area per unit volume of dendritic structure. In fluid flow studies within three dimensional reconstructions of directionally solidified structures, Madison *et al.*[13] have shown that the permeability of these dendritic arrays at the liquid fractions in the range experimentally observed for the final liquid eutectic fraction of the alloy studied here (≈10%) is of the order of 10^{-12} m^2. Furthermore, at these low liquid fractions, it was shown[13] that these 3-D permeabilities are in good correspondence with the modified Blake-Kozeny relationship,[45] where:

$$K = 3.75x10^{-4} f_l^2 \lambda_1^2 \qquad [4.33]$$

Equations 4.30 and 4.33 can be combined to determine the pore size at the critical spacing, where the pressure driven feeding of interdendritic liquid is balanced by the increasing spacing of the dendrites. In this case a simple expression emerges:

$$d_{pore} = \frac{K^{1/2}}{2\sqrt{3.75x10^{-4}}} \qquad [4.34]$$

With the permeability above, this suggests a pore size of 26 μm, which somewhat underestimates the maximum pore size in comparison to Figure 4.15, but this may be due to small differences in the second-generation alloy studied here, compared to the René N4 alloy of the 3-D permeability studies.[13] Statistically, the size of the porosity also shows a strong correlation to λ_2 (Figure 4.20), which is again consistent with the expected scale of the final pockets of liquid eutectic to solidify. A good correlation with both primary and secondary spacing is not unexpected, given that solidification parameters

that influence primary spacings, will also influence secondary spacings. Importantly, is has been shown that maximum pore size may be predicted from either the primary or the secondary dendrite arm spacings if sufficient information on permeability exists.

4.8 Summary

A detailed statistical analysis of primary dendrite distribution has been carried out on transverse sections using Voronoi Tessellations. There is a dominance of six nearest neighbors in the distribution of number of nearest-neighbor primary dendrites for all solidification rates, similar to what has been observe in the literature for other Pb-Sn alloys. A range of primary dendrite spacings is present during directional solidification. The variation in dendrite arm spacing in a fixed cross section decreases significantly by using the LMC process. Using convective cooling with the LMC process to increase the thermal gradient also affects the spacing distribution and packing of dendrites.

Increasing the LMC solidification velocity faster than 12.7 mm/min provides further decreases in maximum pore size due to its strong correlation with λ_2. For optimal solidification velocities, the largest pores reside near the overall average λ_1. This relationship is associated with the competition between the final size of the γ/γ' eutectic pools and interdendritic liquid feeding.

A 65% reduction in maximum pore size is produced using the LMC process at 12.7 mm/min compared to Bridgman casting at 3.4 mm/min. Basic stereology measurements can be applied to 2-D cross-sections of porous single-crystal material in order to accurately measure the main morphological properties, porosity and pore size distribution. A reliable estimation of the maximum pore size contained within in a single crystal casting was successfully obtained using the extreme value analysis method.

An expression was developed to predict maximum pore sizes as a function of permeability, fraction of liquid during solidification and dendritic spacings. The influence of pore size on the fatigue properties will be addressed in Chapter 5.

[1] J.D. Hunt: in *Solidification and Casting of Metals*, J.D. Hunt, eds., The Metals Society, London, 1979, pg. 3-9.

[2] W. Kurz and D.J. Fisher: *Acta Metall*., 1981, 29, pp. 11-20.

[3] B. Skallerund, T. Iveland, G. Harkegard: *Eng. Fract. Mech*., 1993, 44, pp. 857-874.

[4] Q.G. Wang, D. Apelian, D.A. Lados: *J. of Light Met*., 2001, 1, pp. 73-84.

[5] J.Z. Yi, P.D. Lee, T.C. Lindley, and T. Fukui: *Mat. Sci. Eng. A*, 2006, 432A, pp. 59-68.

[6] J. Hui, R. Tiwari, X. Wu, S.N. Tewari and R. Trivedi: *Metall. Mater. Trans A*., 2002, 33, pp. 3499-3510.

[7] J.D. Miller: *PhD Thesis*, University of Michigan, Ann Arbor, MI, 2010.

[8] T.M. Pollock: Mater. Sci. Eng. B, 1995, B32, pp. 255-266.

[9] J.A. Warren and J.S. Langer: Phys. Rev. 1990, A42, pp. 3518.

[10] J.A. Warren and J.S. Langer: Phys. Rev. 1993, A47, pp. 2702.

[11] C.L. Brundidge, J.D. Miller, and T.M. Pollock: *Metall. Mater. Trans. A*., 2011, in press.

[12] D.G. McCartney and J.D. Hunt: *Acta Metall*., 1981, 29, pp. 1851-1863.

[13] J. Madison, J. Spowart, D. Rowenhorst, L.K. Aagesen, K. Thornton, and T.M. Pollock: A*cta Mater*., 2010, 58, pp. 2864-2875.

[14] S. Tin, T.M. Pollock, and W. Murphy: *Metall. Mater. Trans. A*., 2001, 32, pp. 1743-1753.

[15] R. Nasser-Rafi, R. Deshmukh, and D.R. Poirier: *Metall. Mater. Trans. A*. 1985, 16A, pp. 2263-71.

[16] N. Streat and F. Weinberg: *Metall. Trans.*, 1976, 7B, pp. 417-23.

[17] Y. Murakami and M. Endo: *Int. J. of Fatigue,* 1994,16, pp. 163-82.

[18] Y.X. Gao, J.Z. Yi, P.D. Lee, and T.C. Lindley: *Fatigue. Fract. Eng. Mater. Struct*., 2004, 27, pp. 559-570.

[19] K. Gall, M.F. Horstemeyer, B.W. Degner, D.L. McDowell, and J. Fan: *Int. J. Fract.*, 2001, 108. Pp. 207-233.

[20] M.A. Delesse: *C.R. Acad. Sci. Paris*, 1847, 25, pp. 544-545.